

Soft X-Ray Spectroscopy of Astrophysical Plasmas

S.M. Kahn

Columbia University, New York, USA

1 Introduction

These lectures are intended to provide a review of the basic physics necessary for the interpretation of high resolution soft X-ray spectra of astrophysical sources. While many of the topics I discuss can be found at the requisite level of sophistication in standard textbooks on atomic physics and spectroscopy (e.g. [1]), I have made an attempt to highlight those aspects which are especially important for X-ray transitions, and which are relevant at the characteristic temperatures and densities typically found in various types of X-ray emitting astrophysical plasmas.

My emphasis is on discrete atomic transitions, which dominate the spectra of most cosmic sources in the soft X-ray band ($100 \text{ eV} \leq E \leq 10 \text{ keV}$). I do not discuss basic continuum processes like bremsstrahlung, synchrotron emission, and inverse Compton emission, as these are covered well in the usual texts used to introduce students to radiative processes in astrophysics (e.g. [2]).

In general, I avoid long derivations, concentrating instead on the key physical ideas that underlie the various formulas, and especially on the definition of terms that appear frequently in the atomic physics literature. The level is intended for advanced undergraduates and beginning graduate students with little or no background in X-ray spectroscopy. While I do assume a rudimentary familiarity with the basics of classical and quantum physics (typical of the preparation one would receive as an undergraduate physics major in an American university), the lectures are self-contained, and were designed to provide a suitable introduction to this field without the need for extensive consultation of other source materials.

The organization is as follows: in the remainder of this initial chapter, I provide a brief introduction to the role of X-ray spectroscopy in astrophysics, and the physical conditions in various types of cosmic X-ray sources. Chapters 1 through 3 cover the essentials of atomic physics: classical and quantum radiation theory, atomic structure, and electron-ion collisional processes, respectively. In Chap. 4, I discuss the various types of equilibria that apply in astrophysical plasmas, and in Chap. 5, I provide a relatively brief review of the most important discrete-line spectral diagnostics that fall in the soft X-ray band. Chapter 6 includes a set of concluding remarks and some thoughts on where this field might be headed in the future.

1.1 The Role of X-Ray Spectroscopy in Astrophysics

X-ray astronomy is not a “new” field of research. Most practitioners date its inception to the serendipitous detection of the very bright binary X-ray source, Scorpius X-1, in June of 1962 [3]. That momentous discovery proved that cosmic systems could be copious X-ray emitters, and that observations in the X-ray band could provide new insights into astrophysical phenomena that could not be gleaned from observations at longer wavelengths. In the ensuing forty years, this field has grown to become one of the major disciplines of observational astrophysics. Hundreds of thousands of discrete sources of X-ray emission have been detected, covering nearly all classes of astrophysical systems.

Until very recently, however, real X-ray *spectra* of astrophysical sources, with sufficient resolution and sensitivity to enable the investigation of individual atomic features, had been largely unavailable. This was principally due to instrumental limitations. Since cosmic X-ray sources are exceedingly faint (typical fluxes for sources of interest are $\sim 10^{-3}$ phot cm $^{-2}$ s $^{-1}$ keV $^{-1}$), early experiments required large area detectors with very high efficiency for photon detection. Gas proportional counters were the instruments of choice. In the soft X-ray band, the spectral resolution achievable with such devices is extremely limited: $E/\Delta E \sim \text{few}$. While the data obtained with those experiments did provide some measure of the overall shapes of cosmic X-ray spectra, they could not be used to derive any real constraints on physical conditions in source emission regions.

The situation improved significantly in the mid 1990’s with the launch of the *ASCA* Observatory. This was the first mission to incorporate charge-coupled device (CCD) detectors at the focus of an X-ray telescope. The energy resolution of CCDs is roughly an order of magnitude better than that achievable with proportional counters. That enabled the detection of broad “humps” in the spectra, which could loosely be identified with complexes of emission lines from particular ions. Yet detailed spectral constraints could still only be derived from model fits to the spectra – even CCD resolution was insufficient to allow for direct interpretation of the intensities of individual features. Hence, the true power of spectroscopy had still not been realized.

Shortly before these lectures were delivered, however, the National Aeronautics and Space Administration launched the *Chandra* X-ray Observatory (June 1999), and the European Space Agency launched the *XMM-Newton* Observatory (December 1999). These two magnificent space missions both incorporate diffraction grating spectrometers, with resolving powers $E/\Delta E \geq 200$ across most of the soft X-ray band. They have collectively provided the first high resolution X-ray spectra of a wealth of astrophysical sources. This has created a revolution in this field, whose significance, even as of this writing two years later, is still continuing to be appreciated. In some cases, the data have provided striking confirmation of existing astrophysical

models. In others, they have presented significant challenges to our basic understanding of the sources involved.

Why is soft X-ray spectroscopy an important tool for astronomy?

There are several unique features of the soft X-ray band that play a role. First, X-ray emitting gas is often the “key” component of the astrophysical system. For many objects (e.g. elliptical galaxies, clusters of galaxies), the virial temperature, $kT \sim GMm_p/R$, lies in the range 10^6 – 10^8 K, where most of the emission comes out at soft X-ray energies. In others (e.g. supernova remnants, binary sources), shocks heat gas into the same temperature regimes. Second, the conventional soft X-ray band (0.1–10 keV) is unusually rich in discrete spectral features. The K-shell transitions of carbon through iron, and the L-shell transitions of silicon through iron fall in this range. In contrast to other wave bands, all charge states are visible in a single X-ray spectrum. This makes the interpretation of the spectrum relatively unambiguous. For example, one can derive relative elemental abundances without invoking any assumptions about the thermal state of the gas. Finally, because of the high radiative decay rates of X-ray transitions, astrophysical emitting plasmas are generally not in local thermodynamic equilibrium. This means that the details of the observed spectra depend on the explicit mechanisms by which the levels are populated. While that can occasionally lead to complications in the interpretation of the data, it also implies that they are quite sensitive to physical conditions in the source. Hence, X-ray spectra have high diagnostic utility.

Astrophysical X-ray spectroscopy can also be of interest as a probe of fundamental physics issues in unusual environments. In particular, cosmic plasmas can achieve extremely low densities, $n_e < 10^{-3} \text{ cm}^{-3}$, orders of magnitude below the densities found in the best vacuum obtainable in a laboratory. At such low densities, radiative decays from very long-lived metastable levels are important. In addition, the time scales for equilibration can be very long in comparison to the lengths of our observations. This means that for some sources, the emitting plasmas appear “frozen” in non-equilibrium states. Finally, given the vast physical scales characteristic of astronomical systems, we can find interesting examples of non-negligible optical depth for exotic absorption and scattering processes.

1.2 Characteristics of Cosmic X-ray Sources

An extensive review of the general science of X-ray astronomy is well beyond the scope of these lectures. However, I believe it is useful, in this introductory chapter, to provide a very brief accounting of physical conditions in the various types of cosmic X-ray sources we are studying with our spectroscopic experiments. More complete discussions of all of these topics can be found in a series of conference proceedings that have appeared within the past year [4].

General introductions to X-ray astronomy, suitable for non-specialists, have been written recently by Schlegel [5] and Tucker & Tucker [6].

Late-Type Stars

X-ray emission from late-type stars (stars of spectral type F, G, K and M) is believed to be produced in coronae, tenuous collections of hot gas confined by magnetic field lines above the stellar photospheres. The best known example, of course, is the solar corona, which was first detected in X-rays by a rocket experiment in 1951. The X-ray luminosity of the quiescent solar corona is $\sim 2 \cdot 10^{27} \text{ erg s}^{-1}$, which is only of order a part in a million of the total solar luminosity. The characteristic temperature is $\sim 2 \cdot 10^6 \text{ K}$, and the characteristic electron density is $\sim 10^9 \text{ cm}^{-3}$. However, the Sun turns out to be a rather weak X-ray source. More active late-type stars exhibit X-ray luminosities as high as $10^{32} \text{ erg s}^{-1}$, with temperatures \sim several 10^7 K , and densities that can reach 10^{14} cm^{-3} . Coronal plasmas are optically thin to photoelectric absorption, although line optical depths for the highest oscillator strength lines can be greater than unity. Most active stars exhibit flares, which can increase the luminosities by three to four orders of magnitude on time scales of minutes to hours. There are many issues associated with the formation and energization of stellar coronae that are still poorly understood, making this an active area of research.

Early-Type Stars

Massive early-type stars (spectral types O and B) do not possess the outer convective zones believed to provide the dynamo necessary to generate stellar coronae. On the other hand, these stars possess massive, radiatively driven stellar winds, with mass loss rates $\sim 10^{-6} M_{\odot}$ per yr. X-ray emission from these systems is believed to arise in shocks in the wind, driven by inhomogeneities resulting from both thermal and dynamical instabilities. Typical X-ray luminosities are $\sim 10^{31} \text{ erg s}^{-1}$, with characteristic temperatures \sim several 10^6 K . Since the wind is dense ($n_e \geq 10^{11} \text{ cm}^{-3}$), and far from fully ionized, the overlying photoelectric opacity is significant. However, the shocks are believed to be distributed throughout the wind, so the absorption structure can be quite complex. Emission lines arising from this gas should exhibit velocity broadening with characteristic velocity widths of several 10^3 km s^{-1} .

Supernova Remnants

Supernovae are cataclysmic stellar explosions which drive high temperature blast waves in the surrounding interstellar medium. There are essentially two varieties. Type 2's which result when massive stars exhaust their nuclear fuel and implode, and Type 1a's which result when white dwarf stars accrete material from their binary companions, causing their masses to exceed the critical

“Chandrasekhar limit” ($\sim 1.4 M_{\odot}$) – the maximum allowable for hydrostatic stability. In both cases, $\sim 10^{50}$ – 10^{51} erg of kinetic energy is transferred to the outer layers of the star, which expand into the neighboring environment. Shock waves form in both the stellar ejecta and the surrounding interstellar gas, with initial temperatures \sim few 10^8 K. These shocks radiate brightly at X-ray energies for $\geq 10^4$ yr. As the remnant expands, the temperature drops, roughly as the third power of the radius. The X-ray emitting gas can have a range of densities, from 10^{-2} to 10^1 cm^{-3} . At such low densities, the time scale for ionization balance to be achieved can exceed the age of the remnant, implying that the plasma may be well out of equilibrium. Despite the very large length-scales involved, the density is low enough that the gas is optically thin to both line and continuum radiation.

X-ray Binaries

Nearly half of all stars in the sky are in binaries, i.e. gravitationally bound two-star systems. Stars of higher mass evolve faster, eventually collapsing to form a “compact object” (white dwarf, neutron star, or black hole). Hence, binary systems can form where one member is compact, and the other is relatively normal. If the binary separation is sufficiently short, these systems exhibit mass transfer, wherein the normal star loses mass that is subsequently accreted by the compact companion. Infall into the deep gravitational potential well characteristic of a compact star, shocks the accreting material up to high temperatures, causing these systems to be copious X-ray emitters. For a white dwarf, $\sim 10^{-4}$ of the rest mass energy of the accreting matter may be released in the form of X-radiation. For a neutron star or black hole, the fraction can be much higher, approaching 20%, leading to X-ray luminosities as high as 10^{38} ergs s^{-1} .

There are two possible modes of mass transfer. If the companion is an early type star, it may have a significant stellar wind, some of which will be gravitationally captured by the compact object. Such systems are called “high mass X-ray binaries” (HMXBs). On the other hand, if the companion has low mass, but expands to fill the critical equipotential surface that connects to the other star (the so-called *Roche lobe*), material can flow freely through an inner Lagrange point and fall inward to the compact star. This process is called Roche lobe overflow, and the resulting X-ray sources are called “low mass X-ray binaries” (LMXBs). If the compact star is a white dwarf, instead of a neutron star or black hole, the source is called a “cataclysmic variable star” (CV).

The fate of the accreting material is not well understood, and probably varies from source to source. Since it is far easier to dissipate energy than angular momentum, it is thought that the flow should settle into a thin *accretion disk*, with the matter moving in near Keplerian orbits. Some form of viscous interaction between neighboring “rings” allows angular momentum to be transferred out, thereby enabling accretion to proceed, either continuously,

or episodically. Most of the X-radiation is released down near the surface of the compact star (or in the case of a black hole, near the event horizon). Because the material is nearly fully ionized, and the Compton depths are non-negligible, the emergent flux is radiated primarily as a continuum, with characteristic photon energies of order a few keV. However, the transfer of this intense continuum outward through the circumsource medium can generate a wealth of discrete features. The irradiated environment is likely to be severely photoionized, with the energy density in the radiation field nearly four orders of magnitude higher than the thermal kinetic energy of the gas.

Active Galactic Nuclei

The term “active galactic nucleus” (AGN) refers to an intense source of radiation emanating from a compact nuclear region at the center of a galaxy. The first “quasi-stellar objects”, or quasars, were discovered in the early 1960’s. Spectra of these sources indicated significant redshifts, implying large distances, and thus very high luminosities, comparable to that of an entire galaxy. In addition, observed short-term variations in the emission suggested that the emitting regions must be compact, with characteristic dimensions comparable to the size of our solar system.

There is a rich variety of empirical phenomena associated with AGNs, leading to the definition of numerous “classes”, however it is generally believed that most of these can be understood in terms of a grand unified model, wherein a supermassive accreting black hole is surrounded by an obscuring torus of optically thick material, oriented in the equatorial plane. Accretion onto the black hole generates X-radiation, as well as relativistic jets along the spin axis. If our line of sight is oriented above the plane of the torus, we get a direct view of the black hole and the source is bright in X-rays. Such systems are called Seyfert 1 galaxies if they are radio-quiet, or Type 1 quasars if they are radio-loud. If our line of sight is oriented along the plane, the central source is obscured, and the soft X-ray emission we see is mainly reprocessed radiation emanating from the circumsource environment. These are called Seyfert 2 galaxies (radio-quiet), or Type 2 quasars (radio-loud). Finally, if our line of sight is oriented along the jet, the observed emission is greatly enhanced by relativistic beaming. These systems are called BL Lac objects, or more generally, “blazars”.

Our understanding of the accretion process in AGNs is even less well-developed than for X-ray binaries. However, it is believed that similar physical processes must be involved. There is some evidence for the existence of relativistically broadened X-ray emission lines in these systems, which could be produced in the inner most regions of the accretion disk around the black hole. If this interpretation is correct, X-ray spectroscopy of AGNs may provide us with one of our best observational handles on the physics of ultra-strong gravitational fields. For the Seyfert 2 systems, the obscuration

of the central source affords a relatively “clean” view of the surrounding photoionized gas. Soft X-ray spectra of these systems are rich in discrete spectral features.

Clusters of Galaxies

Clusters are massive collections of galaxies that have formed relatively recently via gravitational collapse as the universe has expanded. They are gravitationally bound systems, with most of the mass in the form of dark matter that only interacts weakly (if at all) with ordinary baryonic matter. The richest, most evolved clusters contain hundreds of members, centered on a central dominant galaxy. The intracluster medium is filled with hot gas, in rough hydrostatic equilibrium with the dark matter gravitational potential. Characteristic temperatures are in the range 10^7 – 10^8 K, so that the gas radiates mostly at X-ray energies. Electron densities are $\sim 10^{-3}$ cm $^{-3}$, and typical X-ray luminosities lie in the range 10^{43} – 10^{45} erg s $^{-1}$. Even at such low densities, the cooling timescales appropriate to this gas are often significantly less than the age of the system, especially at the cluster core. This leads to the expectation that gas should continually be cooling out of this medium, perhaps eventually forming stars in the central galaxy. Curiously, however, recent X-ray spectra suggest a deficit of low temperature gas predicted by this scenario. The intracluster media should be mostly optically thin to continuum absorption, but can exhibit non-negligible optical depth for scattering of bright emission lines.

2 Classical and Quantum Radiation Theory

2.1 Introduction

In this chapter, I review the essential components of classical and quantum radiation theory. I assume that most of the material will be very familiar to the reader from undergraduate (and perhaps graduate) coursework in electrodynamics and elementary quantum mechanics. Nevertheless, I believe it is useful to offer this quick review so that we have the relevant formulae ready at hand for reference in later discussions. You might expect that classical radiation theory should find very limited application in a discussion of discrete radiation from atoms, but as I will show, it does provide a quick means of deriving order of magnitude estimates for a number of important processes. In addition, I find it pedagogically useful to discuss the classical and quantum formulae in a unified context. This is rarely done in textbooks, which makes it difficult to follow where and when quantum ideas are important.

In this, and all subsequent chapters, I utilize the CGS system of units. Although this is going out of fashion in most fields of physics (where SI units have indeed become standard), it is still common practice in astrophysics.

In addition, the fundamental equations of radiation theory take on a simple and more elegant form in CGS units. In this system, the unit of charge is the esu, defined such that Coulomb's Law for the attraction between two point charges, q_1 and q_2 is:

$$\mathbf{F}(\mathbf{r}) = \frac{q_1 q_2}{r^2} \hat{\mathbf{r}}, \quad (1)$$

where \mathbf{r} is the vector separation between them and $\hat{\mathbf{r}}$ the unit vector pointing in the \mathbf{r} direction. Thus, $1 \text{ (esu)}^2 = 1 \text{ erg cm}$. In this system, the electric and magnetic fields, \mathbf{E} and \mathbf{B} , have the same units, usually expressed as gauss.

2.2 Overview of the Classical Equations

We start with the governing equations of electromagnetism, specifically *Maxwell's equations*:

$$\nabla \cdot \mathbf{E} = 4\pi \rho, \quad \nabla \cdot \mathbf{B} = 0, \quad (2)$$

$$\nabla \times \mathbf{E} = -\frac{1}{c} \frac{\partial \mathbf{B}}{\partial t}, \quad \nabla \times \mathbf{B} = \frac{4\pi}{c} \mathbf{j} + \frac{1}{c} \frac{\partial \mathbf{E}}{\partial t}. \quad (3)$$

which relate the spacetime derivatives of the electric and magnetic fields to each other and to the charge and current densities of the medium, ρ and \mathbf{j} , respectively. In addition, the *Lorentz force law*:

$$\mathbf{f} = \rho \mathbf{E} + \frac{1}{c} \mathbf{j} \times \mathbf{B} \quad (4)$$

relates the force density on a charged volume, \mathbf{f} , to the fields and the charge and current densities. Due to the conservation of electric charge, ρ and \mathbf{j} obey a *continuity equation*:

$$\frac{\partial \rho}{\partial t} + \nabla \cdot \mathbf{j} = 0. \quad (5)$$

It is useful to define also the scalar and vector potential functions, φ and \mathbf{A} , respectively, which are related to the fields by:

$$\mathbf{B} = \nabla \times \mathbf{A}, \quad (6)$$

$$\mathbf{E} = -\nabla \varphi - \frac{1}{c} \frac{\partial \mathbf{A}}{\partial t}. \quad (7)$$

Equations (6) and (7) do not define φ and \mathbf{A} uniquely. To make the definitions unique, we need to further specify a gauge. For radiation theory, it is most convenient to adopt the *Lorentz gauge*:

$$\nabla \cdot \mathbf{A} + \frac{1}{c} \frac{\partial \varphi}{\partial t} = 0 \quad (8)$$

Substitution into Maxwell's equations yield:

$$\left(\nabla^2 - \frac{1}{c^2} \frac{\partial^2}{\partial t^2}\right) \varphi = -4\pi \varrho, \quad (9)$$

$$\left(\nabla^2 - \frac{1}{c^2} \frac{\partial^2}{\partial t^2}\right) \mathbf{A} = -\frac{4\pi}{c} \mathbf{j}. \quad (10)$$

which relate the potentials to the charge and current densities. These equations have solutions of the form:

$$\varphi(\mathbf{r}, t) = \int d^3\mathbf{r}' dt' \frac{\varrho(\mathbf{r}', t')}{|\mathbf{r} - \mathbf{r}'|} \delta[t' - t_r(\mathbf{r}, t, \mathbf{r}')] , \quad (11)$$

$$\mathbf{A}(\mathbf{r}, t) = \int d^3\mathbf{r}' dt' \frac{\mathbf{j}(\mathbf{r}', t')}{|\mathbf{r} - \mathbf{r}'|} \delta[t' - t_r(\mathbf{r}, t, \mathbf{r}')] \quad (12)$$

where t_r is the retarded time, defined by:

$$t_r \equiv t - \frac{|\mathbf{r} - \mathbf{r}'|}{c}. \quad (13)$$

Differentiation of the right-hand sides of (11), (12) according to (6), (7) yields the electric and magnetic fields associated with arbitrary time-varying charge and current distributions. We return to this shortly.

2.3 Electromagnetic Waves

In charge-free space, Maxwell's equations (2), (3) give rise to wave equations for both the electric and magnetic fields:

$$\left(\nabla^2 - \frac{1}{c^2} \frac{\partial^2}{\partial t^2}\right) \mathbf{E} = 0, \quad (14)$$

$$\left(\nabla^2 - \frac{1}{c^2} \frac{\partial^2}{\partial t^2}\right) \mathbf{B} = 0 \quad (15)$$

which have plane-wave solutions written in the form:

$$\mathbf{E} = \mathbf{E}_0 e^{i(\mathbf{k} \cdot \mathbf{r} - \omega t)}, \quad (16)$$

$$\mathbf{B} = \mathbf{B}_0 e^{i(\mathbf{k} \cdot \mathbf{r} - \omega t)} \quad (17)$$

where

$$\omega = kc, \quad (18)$$

$$\mathbf{k} \cdot \mathbf{E}_0 = \mathbf{k} \cdot \mathbf{B}_0 = 0, \quad (19)$$

$$\mathbf{k} \times \mathbf{E}_0 = \frac{\omega}{c} \mathbf{B}_0, \quad (20)$$

$$\mathbf{k} \times \mathbf{B}_0 = -\frac{\omega}{c} \mathbf{E}_0, \quad (21)$$

$$\hat{k} = \hat{E} \times \hat{B}, \quad (22)$$

the waves are transverse, and the fields have equal magnitudes. The first (18) requires that electromagnetic waves travel at the speed of light in the vacuum. The energy flux associated with electromagnetic waves is given by the *Poynting vector*:

$$\mathbf{S} = \frac{c}{4\pi} \mathbf{E} \times \mathbf{B} \quad (23)$$

which has units of $\text{erg cm}^{-2} \text{s}^{-1}$ in the CGS system. For the plane-wave solutions (16), (17), (18)–(22) imply that the real part of the Poynting vector is given by:

$$\mathbf{S}(t) = \hat{k} \frac{c}{4\pi} |E(t)|^2 . \quad (24)$$

The plane waves described above are monochromatic. Since the wave equations are linear, however, arbitrary linear combinations of plane-waves also provide solutions. In general, we are interested in the frequency dependence of the radiation, which can be assessed by taking the Fourier transform of the electric field:

$$\tilde{\mathbf{E}}(\omega) \equiv \frac{1}{2\pi} \int_{-\infty}^{\infty} \mathbf{E}(t) e^{i\omega t} dt . \quad (25)$$

Parseval's Theorem for Fourier transforms requires:

$$\int_{-\infty}^{\infty} |\mathbf{E}(t)|^2 dt = 2\pi \int_{-\infty}^{\infty} |\tilde{\mathbf{E}}(\omega)|^2 d\omega = 4\pi \int_0^{\infty} |\tilde{\mathbf{E}}(\omega)|^2 d\omega \quad (26)$$

(Since $\mathbf{E}(t)$ is real, $\tilde{\mathbf{E}}(-\omega) = \tilde{\mathbf{E}}(\omega)$). The energy in the radiation per unit area is given by:

$$\frac{dW}{dA} = \int_{-\infty}^{\infty} \mathbf{S}(t) dt = c \int_0^{\infty} |\tilde{\mathbf{E}}(\omega)|^2 d\omega \quad (27)$$

so the energy per unit area per unit frequency is:

$$\frac{dW}{dA d\omega} = c |\tilde{\mathbf{E}}(\omega)|^2 . \quad (28)$$

2.4 The Classical Multipole Expansion

As for the electric field, we can take the Fourier transform of the charge, current density and vector potential:

$$\tilde{\varrho}(\mathbf{r}, \omega) \equiv \frac{1}{2\pi} \int_{-\infty}^{\infty} \varrho(\mathbf{r}, t) e^{i\omega t} dt , \quad (29)$$

$$\tilde{\mathbf{j}}(\mathbf{r}, \omega) \equiv \frac{1}{2\pi} \int_{-\infty}^{\infty} \mathbf{j}(\mathbf{r}, t) e^{i\omega t} dt , \quad (30)$$

$$\tilde{\mathbf{A}}(\mathbf{r}, \omega) \equiv \frac{1}{2\pi} \int_{-\infty}^{\infty} \mathbf{A}(\mathbf{r}, t) e^{i\omega t} dt . \quad (31)$$

Using (12) and (13) we get:

$$\tilde{\mathbf{A}}(\mathbf{r}, \omega) = \frac{1}{c} \int d^3\mathbf{r}' \frac{\tilde{\mathbf{j}}(\mathbf{r}', \omega) e^{ik|\mathbf{r}-\mathbf{r}'|}}{|\mathbf{r}-\mathbf{r}'|} \quad (32)$$

where $k = \omega/c$. If we are interested in the character of the radiation far from the charge distribution, then $|\mathbf{r}| \gg |\mathbf{r}'|$, so that $|\mathbf{r}-\mathbf{r}'| \approx r - \hat{n} \cdot \mathbf{r}'$, where \hat{n} is the unit vector pointing in the direction \mathbf{r} . We thus obtain:

$$\tilde{\mathbf{A}}(\mathbf{r}, \omega) \approx \frac{e^{ikr}}{rc} \int d^3\mathbf{r}' \tilde{\mathbf{j}}(\mathbf{r}', \omega) e^{-ik(\hat{n} \cdot \mathbf{r}')} . \quad (33)$$

The classical multipole expansion involves a Taylor expansion of the complex exponential inside the integral in (33), assuming that $k(\hat{n} \cdot \mathbf{r}') \ll 1$. To see why this might be valid, note that:

$$k(\hat{n} \cdot \mathbf{r}) \sim R\omega/c \sim v/c \quad (34)$$

where R is the characteristic dimension of the charge distribution, and v is a characteristic velocity of the oscillating charge. Thus the multipole expansion is justified in the limit that the charge motions are non-relativistic. The lowest order term is obtained by setting the complex exponential equal to unity. We are then left with a simple integral of the Fourier transform of the current density which can be rewritten in terms of the dipole moment of the charge distribution, $\tilde{\mathbf{d}}(\omega)$

$$\begin{aligned} \int d^3\mathbf{r}' \tilde{\mathbf{j}}(\mathbf{r}', \omega) &= - \int d^3\mathbf{r}' (\nabla' \cdot \tilde{\mathbf{j}}) \mathbf{r}' = -ikc \int d^3\mathbf{r}' \tilde{\rho}(\mathbf{r}', \omega) \mathbf{r}' \\ &\equiv -ikc \tilde{\mathbf{d}}(\omega) . \end{aligned} \quad (35)$$

We thus refer to this term as the *electric dipole* or (E1) term. Expressions for $\tilde{\mathbf{E}}$ and $\tilde{\mathbf{B}}$ in the electric dipole limit can be found by taking the appropriate derivatives of $\tilde{\mathbf{A}}$. Then, converting back to the time domain, we obtain:

$$\mathbf{E}(\mathbf{r}, t) = \frac{1}{c^2 r} [\hat{n} \times (\hat{n} \times \ddot{\mathbf{d}}(t_r))] \quad (36)$$

where $\ddot{\mathbf{d}}(t_r)$ is the second time-derivative of the electric dipole moment evaluated at the retarded time. The Poynting vector is:

$$\mathbf{S} = \frac{c}{4\pi} |\mathbf{E}|^2 \hat{n} = \frac{|\ddot{\mathbf{d}}|^2 \sin^2\theta}{4\pi r^2 c^3} \hat{n} \quad (37)$$

Integrating over the surface of a sphere of radius r yields the total energy radiated per unit time:

$$\frac{dW}{dt} = \int \mathbf{S} r^2 d\Omega = \frac{2}{3} \frac{|\ddot{\mathbf{d}}|^2}{c^3} . \quad (38)$$

For a single, accelerating point charge, this reduces to the well-known *Larmor formula*:

$$\frac{dW}{dt} = \frac{2}{3} \frac{q^2 a^2}{c^3} \quad (39)$$

where a is the acceleration of the charge.

For non-relativistic motions, the electric dipole term will dominate whenever it is non-zero. If it is zero, however, the next highest term will be important. In that case, the relevant integral in (33) is:

$$\int d^3 \mathbf{r}' \tilde{\mathbf{j}}(\tilde{\mathbf{r}}', \omega) (\hat{\mathbf{n}} \cdot \tilde{\mathbf{r}}') \quad (40)$$

which can be “broken” into two parts:

$$\tilde{\mathbf{j}}(\mathbf{r}', \omega) (\hat{\mathbf{n}} \cdot \mathbf{r}') = \frac{1}{2} \left[\tilde{\mathbf{j}}(\hat{\mathbf{n}} \cdot \mathbf{r}') - \mathbf{r}' (\tilde{\mathbf{j}} \cdot \hat{\mathbf{n}}) \right] + \frac{1}{2} \left[\tilde{\mathbf{j}}(\hat{\mathbf{n}} \cdot \mathbf{r}') + \mathbf{r}' (\tilde{\mathbf{j}} \cdot \hat{\mathbf{n}}) \right] \quad (41)$$

The integral of the first term on the right-hand side of (41) can be shown to be related to the magnetic dipole moment of the current distribution:

$$\tilde{\boldsymbol{\mu}}(\omega) \equiv \frac{1}{2c} \int d^3 \mathbf{r}' \mathbf{r}' \times \tilde{\mathbf{j}}(\mathbf{r}', \omega) \quad (42)$$

while the integral of the second term is related to the electric quadrupole tensor of the charge distribution:

$$\tilde{Q}(\omega) \equiv \int d^3 \mathbf{r}' \left[3\mathbf{r}' \mathbf{r}' - r'^2 I \right] \tilde{q}(\mathbf{r}', \omega) \quad (43)$$

where I is the identity tensor. The radiated power for the magnetic dipole term is:

$$\frac{dW}{dt} = \frac{2}{3} \frac{|\dot{\boldsymbol{\mu}}|^2}{c^3} . \quad (44)$$

For the electric quadrupole term, the integral over solid angle depends on the explicit form of the quadrupole tensor, but the radiated power is proportional to $|\ddot{Q}|^3 / c^5$. Note that for an oscillating charge distribution:

$$|\ddot{\mathbf{d}}| \sim qR\omega^2, \quad |\ddot{\boldsymbol{\mu}}| \sim R \left(\frac{qv}{c} \right) \omega^2 \quad (45)$$

and

$$|\ddot{Q}| \sim qR^2\omega^3 . \quad (46)$$

Taking $R\omega \sim v$, we find:

$$\frac{dW}{dt} \sim \frac{q^2 \omega}{R} \left(\frac{v}{c} \right)^3 \quad (E1), \quad (47)$$

$$\frac{dW}{dt} \sim \frac{q^2 \omega}{R} \left(\frac{v}{c} \right)^5 \quad (M1), \quad (48)$$

$$\frac{dW}{dt} \sim \frac{q^2 \omega}{R} \left(\frac{v}{c} \right)^5 \quad (E2). \quad (49)$$

So the (M1) and (E2) terms are of the same order and are both down from the (E1) term by a factor $\sim(v/c)^2$, where v is a characteristic velocity of the charges.

2.5 The Classical Oscillator

An important application of classical radiation theory, and one that proves useful in understanding radiation from atoms, is the *classical harmonic oscillator*, in which the acceleration of the charge is given by:

$$\ddot{\mathbf{x}} = -\omega_0^2 \mathbf{x} \quad (50)$$

where \mathbf{x} is the position of the oscillating charge, and ω_0 is the oscillation frequency. However, since an oscillating charge radiates energy, there must be a damping force associated with the radiation, which gradually reduces the amplitude of the oscillation to zero. This is called the “radiation reaction”. We can approximate it by noting that the power dissipated by the drag force must agree with the Larmor formula for the radiated energy. That yields:

$$\mathbf{F}_{drag} \approx \frac{2}{3} \frac{q^2}{c^3} \ddot{\mathbf{x}} \approx \frac{2}{3} \frac{q^2}{c^3} \omega_0^2 \dot{\mathbf{x}} \quad (51)$$

so the equation of motion becomes:

$$\ddot{\mathbf{x}} + \Gamma \dot{\mathbf{x}} + \omega_0^2 \mathbf{x} = 0 \quad (52)$$

where

$$\Gamma = \frac{2}{3} \frac{q^2 \omega_0^2}{mc^3}, \quad (53)$$

and m is the mass of the charge. The solution has the form:

$$\mathbf{x}(t) = \mathbf{x}_0 e^{-\Gamma t/2} \cos(\omega_0 t + \varphi), \quad (54)$$

and thus the Fourier transform of the electric dipole moment ($\mathbf{d}(t) = q\mathbf{x}(t)$), becomes:

$$|\tilde{\mathbf{d}}(\omega)|^2 = q^2 \left(\frac{x_0}{4\pi}\right)^2 \frac{1}{(\omega - \omega_0)^2 + (\Gamma/2)^2}. \quad (55)$$

The radiated spectrum in the (E1) limit is given by:

$$\frac{dW}{d\omega} = \frac{8\pi}{3} \frac{\omega^4}{c^3} |\tilde{\mathbf{d}}(\omega)|^2 \approx \left(\frac{1}{2} k |\mathbf{x}_0|^2\right) \left[\frac{\Gamma/2\pi}{(\omega - \omega_0)^2 + (\Gamma/2)^2} \right]. \quad (56)$$

Here $1/2 k |\mathbf{x}_0|^2$ ($k \equiv m\omega_0^2$ is the “spring constant” of the oscillator) is the initial energy of the oscillation, and the term in brackets describes a Lorentzian line profile, centered at ω_0 , with width equal to Γ . Note that:

$$\Delta\nu = \frac{1}{2\pi} \Delta\omega = \frac{4\pi}{3} \frac{q^2 \nu_0^2}{mc^3} \quad (57)$$

and

$$\Delta\lambda = \frac{c}{\nu_0^2} \Delta\nu = \frac{4\pi}{3} \frac{q^2}{mc^2} \quad (58)$$

is a constant, independent of frequency or wavelength. This is the classical *natural line width* for electric dipole transitions. For an electron, $\Delta\lambda \approx 1.2 \cdot 10^{-4} \text{ \AA}$. For the soft X-ray transitions we are concerned with in this lecture, $\lambda \approx 1 - 100 \text{ \AA}$, so the natural width is nearly always a very small component of the line broadening. The time-averaged radiated power of the classical oscillator is:

$$\frac{dW}{dt} = \frac{1}{3} \frac{q^2 \omega_0^4 |\mathbf{x}_0|^2}{c^3}. \quad (59)$$

Since the initial energy, $W_0 = 1/2 k |\mathbf{x}_0|^2 = 1/2 m \omega_0^2 |\mathbf{x}_0|^2$, the *classical radiative decay rate* is given by:

$$A_{cl} \equiv \frac{(dW/dt)}{W_0} = \frac{2}{3} \frac{q^2 \omega_0^2}{mc^3} \quad (60)$$

which turns out to be equal to the damping constant, Γ . In terms of the linear frequency:

$$A_{cl} = \frac{8\pi^2}{3} \frac{q^2}{mc^3} \nu^2 \approx 2.5 \cdot 10^{-22} \nu^2 \text{ s}^{-1} \quad (61)$$

for an electron, where ν is in Hz. Note that in the X-ray band, where $\nu \approx 10^{16} - 10^{18}$ Hz, radiative decay rates are extremely fast, $\sim 10^{10} - 10^{14} \text{ s}^{-1}$. This has an important effect on level populations for X-ray emitting plasmas, as we will see later.

The discussion above pertains to spontaneous emission. To model induced processes, like photoexcitation, we must consider driven oscillations, where there is an applied force due to an incoming wave, given by: $\mathbf{F}_{appl} = q\mathbf{E}_0 e^{i\omega t}$. The equation of motion is now that of a damped, driven harmonic oscillator. The time-averaged radiated power for this case becomes:

$$\frac{dW}{dt} = \frac{q^4 |\mathbf{E}_0|^2}{3m^2 c^3} \frac{\omega^4}{(\omega^2 - \omega_0^2)^2 + (\Gamma\omega_0)^2}. \quad (62)$$

Since the time-averaged incident energy flux in the wave is $\langle S \rangle = c/8\pi |\mathbf{E}_0|^2$, the cross-section for scattering is:

$$\sigma(\omega) = \frac{dW/dt}{\langle S \rangle} = \frac{8\pi}{3} \frac{q^4}{m^2 c^4} \frac{\omega^4}{(\omega - \omega_0)^2 + (\Gamma/2)^2}. \quad (63)$$

In the vicinity of line center: $\omega^2 - \omega_0^2 \approx 2\omega_0(\omega - \omega_0)$, so this becomes:

$$\sigma(\omega) = \frac{2\pi^2 q^2}{mc} \frac{\Gamma/2\pi}{(\omega^2 - \omega_0^2)^2 + (\Gamma\omega_0)^2} \quad (64)$$

where we have used our earlier expression for Γ . The scattering cross-section again has the Lorentzian line profile with width in angular frequency equal to Γ . Integrating over frequency yields:

$$\int_0^\infty \sigma(\omega) d\omega = 2\pi \int_0^\infty \sigma(\nu) d\nu = \frac{2\pi^2 q^2}{mc} \quad (65)$$

so

$$\sigma(\nu) = \frac{\pi q^2}{mc} \varphi(\nu). \quad (66)$$

where $\varphi(\nu)$ is the normalized line shape (it may have other components associated with Doppler broadening, etc.). Note that the coefficient is independent of frequency. For an electron, it has the value: $\pi e^2/mc = 2.7 \cdot 10^{-2} \text{ cm}^2 \text{ Hz}$.

2.6 Quantum Radiation Theory – Overview

We now turn to the quantum theory. There are two fundamental differences between the classical and quantum treatments of the interaction between radiation and matter:

- In quantum mechanics, charge configurations are expressed in terms of quantum “states”. Radiative interactions involve an exchange of energy and momentum, so they are associated with a change of state. The only stationary quantum states are the eigenstates of the Hamiltonian, which is the operator associated with the energy of the system. The rates for various processes therefore involve quantum “matrix elements” of the form $\langle f | H_{rad} | i \rangle$, where f represents the final state, i the initial state, and H_{rad} is the perturbing Hamiltonian associated with the radiation field. In the classical picture, charges radiate when they are accelerated. Acceleration requires an external applied force, which can be identified with the perturbing Hamiltonian.
- In the quantum treatment, the radiation field is described in terms of discrete particles or “photons”. The energy of an individual photon is $E = \hbar\omega = h\nu$, where h is Planck’s constant, and has the value $6.626 \cdot 10^{-27} \text{ erg s}$. The momentum of a photon is given by $\mathbf{p} = \hbar\mathbf{k} = (\hbar\omega/c)\hat{\mathbf{k}}$, directed along the direction of propagation. Photons are spin 1 particles, and therefore the emission or absorption of a photon changes the angular momentum of the system by one unit of \hbar .

The key rates and cross-sections for various radiative processes follow from time-dependent perturbation theory. We begin with the time-dependent *Schrodinger equation*:

$$H | \psi \rangle = i\hbar \frac{\partial | \psi \rangle}{\partial t}. \quad (67)$$

The energy eigenstates satisfy:

$$H | \psi_E \rangle = E | \psi_E \rangle \quad (68)$$

and therefore have a time dependence given by:

$$|\psi_E(t)\rangle = |\psi_E\rangle e^{-iEt/\hbar}. \quad (69)$$

Let the total Hamiltonian contain a dominant “unperturbed part” and a small additional “perturbing part”:

$$H = H^0 + H' \quad (70)$$

and let $|n\rangle$ represent a complete set of energy eigenstates of H^0 . An arbitrary state $|\psi(t)\rangle$ can be expanded in terms of these energy eigenstates:

$$|\psi(t)\rangle = \sum_n a_n(t) |n\rangle e^{-iE_n t/\hbar}. \quad (71)$$

Substituting into (67) and taking the scalar product with a specific energy eigenstate $\langle k |$ to both sides, then yields the differential equation:

$$i\hbar \frac{\partial a_k}{\partial t} = \sum_n a_n \langle k | H' | n \rangle e^{i\omega_{kn}t} \quad (72)$$

where $\omega_{kn} \equiv (E_k - E_n)/\hbar$. Here, we have used the fact that the energy eigenstates are orthonormal: $\langle k | n \rangle = \delta_{k,n}$. Suppose the system is initially in state “m”, so that $a_k(0) = \delta_{k,m}$. Then, to lowest order in the perturbing Hamiltonian, the coefficients a_k at some later time are given by:

$$a_k(t) = (i\hbar)^{-1} \int_0^t \langle k | H'(t) | m \rangle e^{i\omega_{km}t} dt. \quad (73)$$

For application to radiation theory, we are interested in perturbations which are oscillatory in time:

$$H'(t) = H' e^{\pm i\omega t} \quad (74)$$

where ω is some angular frequency. Thus:

$$a_k(t) = (i\hbar)^{-1} \langle k | H' | m \rangle \int_0^t e^{i(\omega_{km} \pm \omega)t} dt. \quad (75)$$

The probability at time t that the system has made the transition from “m” to state “k” is given by $|a_k(t)|^2$. The transition rate, R , is thus given by:

$$R = \lim_{t \rightarrow \infty} \frac{|a_k(t)|^2}{t} = \frac{2\pi}{\hbar^2} |\langle k | H' | m \rangle|^2 \delta(\omega_{km} \pm \omega) \quad (76)$$

$$= \frac{2\pi}{\hbar} |\langle k | H' | m \rangle|^2 \delta(E_k - E_m \pm \hbar\omega). \quad (77)$$

This last expression indicates that the transition is possible only if the change of state is accompanied by the emission or absorption of a single photon with energy equal to the energy difference between the states. Note that this is a first order perturbation result. Multi photon processes occur via higher order terms in the perturbation expansion.

2.7 The Radiation Hamiltonian

The appropriate Hamiltonian to use for the interaction between charged particles and electromagnetic fields is derived from the formalism of classical mechanics. Defining a Lagrangian of the form:

$$L = \frac{1}{2}mv^2 - q\varphi + \frac{q}{c}\mathbf{A} \cdot \mathbf{v} \quad (78)$$

where φ and \mathbf{A} are the classical scalar and vector potentials, respectively, and applying Lagrange's Equation:

$$\frac{d}{dt} \left(\frac{\partial L}{\partial \dot{\mathbf{r}}} \right) = \frac{\partial L}{\partial \mathbf{r}}, \quad (79)$$

we arrive at the desired Lorentz force law for the electromagnetic force on a single charge:

$$\mathbf{F} \equiv m\dot{\mathbf{v}} = q\mathbf{E} + \frac{q\mathbf{v}}{c} \times \mathbf{B}. \quad (80)$$

The canonical momentum of the particle is defined by:

$$\mathbf{p} \equiv \frac{\partial L}{\partial \dot{\mathbf{r}}} = m\mathbf{v} + \frac{q\mathbf{A}}{c}. \quad (81)$$

The Hamiltonian is then:

$$H \equiv \mathbf{p} \cdot \mathbf{v} - L = \frac{1}{2}mv^2 + q\varphi = \frac{1}{2m} \left(\mathbf{p} - \frac{q}{c}\mathbf{A} \right)^2 + q\varphi. \quad (82)$$

It is the canonical momentum \mathbf{p} that we associate with the quantum mechanical operator $(\hbar/i)\nabla$. Substituting into (82) yields:

$$H = -\frac{\hbar^2}{2m}\nabla^2 + \frac{iq\hbar}{mc}(\nabla \cdot \mathbf{A}) + \frac{iq\hbar}{mc}(\mathbf{A} \cdot \nabla) + \frac{q^2}{2mc^2}A^2 + q\varphi. \quad (83)$$

For an electromagnetic wave, $\varphi = 0$, and therefore, in the Lorentz gauge, $\nabla \cdot \mathbf{A} = 0$. The term involving A^2 is small compared to the first order terms in \mathbf{A} , so we ignore it. In addition, there may be a non-radiation potential $V(\mathbf{r})$, e.g. the binding potential of the atom. In that case:

$$H = -\frac{\hbar^2}{2m}\nabla^2 + V(\mathbf{r}) + \frac{iq\hbar}{mc}(\mathbf{A} \cdot \nabla) \quad (84)$$

The first two terms on the right hand side are usually taken to be the unperturbed Hamiltonian. The perturbing Hamiltonian associated with the interaction with radiation is given by the third term. For a strictly monochromatic wave, we can write the vector potential in the form:

$$\mathbf{A}(\mathbf{r}, t) = \text{Re} \left[\mathbf{A}_0 e^{i(\mathbf{k} \cdot \mathbf{r} - \omega t)} \right] = \frac{1}{2} |\mathbf{A}_0| \left[\hat{\mathbf{e}} e^{i(\mathbf{k} \cdot \mathbf{r} - \omega t)} + \hat{\mathbf{e}}^* e^{-i(\mathbf{k} \cdot \mathbf{r} - \omega t)} \right] \quad (85)$$

where $\mathbf{A} = |\mathbf{A}_0| \hat{\varepsilon}$, and $\hat{\varepsilon}$ is the polarization vector of the wave. From (7) and (24), we find that the time-averaged Poynting vector is given by:

$$\langle \mathbf{S} \rangle = \frac{\omega^2}{8\pi c} |\mathbf{A}_0|^2 \hat{k} \quad (86)$$

Recall that $\langle \mathbf{S} \rangle$ represents the energy flux of the radiation. If we think in terms of discrete photons, the photon flux, $dN/dAdt$, is given by:

$$\frac{dN}{dt dA} = \frac{|\langle \mathbf{S} \rangle|}{\hbar\omega} = \frac{\omega}{8\pi\hbar c} |\mathbf{A}_0|^2 . \quad (87)$$

Note from (85) that the perturbing Hamiltonian in (84) has two pieces, one proportional to $e^{-i\omega t}$, and one proportional to $e^{+i\omega t}$. The former leads to the absorption of a photon ($E_k = E_m + \hbar\omega$), while the latter leads to the emission of a photon ($E_k = E_m - \hbar\omega$). For a given set of initial and final states, only one of the two terms can satisfy energy conservation, so we can treat them separately. The expression for the transition rate between initial state i and final state f is thus:

$$R = \frac{2\pi}{\hbar} \frac{q^2 \hbar^2}{4m^2 c^2} |\mathbf{A}_0|^2 \left| \left\langle f \left| e^{\pm i\mathbf{k}\cdot\mathbf{r}} \hat{\varepsilon}^{(*)} \cdot \nabla \right| i \right\rangle \right|^2 \delta(E_f - E_i \mp \hbar\omega) \quad (88)$$

where the top sign corresponds to absorption (with $\hat{\varepsilon}$ in the matrix element) and the bottom sign corresponds to emission (with $\hat{\varepsilon}^*$ in the matrix element).

2.8 Bound-Free Absorption (Photoionization)

Consider first the application to bound-free absorption, where the initial state of an electron is a bound state in an atom, and the final state is that of a free particle. To get the total transition rate, we must integrate over all possible final states. For a free particle, the states are characterized by the momentum vector \mathbf{p} . However, the *uncertainty principle* requires that a particle cannot be localized in a 6-dimensional phase space cell smaller than $d^3\mathbf{r}d^3\mathbf{p} = (2\pi\hbar)^3$. Therefore, the density of states for a free particle is given by:

$$\varrho(E)dE = \frac{Vd^3\mathbf{p}}{(2\pi\hbar)^3} = \frac{Vm(2mE)^{1/2}dEd\Omega}{(2\pi\hbar)^3} \quad (89)$$

where V is the allowable volume for the free particle (it will drop out of the later expression), $d\Omega$ is a differential element of solid angle, and we have assumed non-relativistic dynamics. The free particle final state of the charge can be represented by:

$$\psi_f(\mathbf{r}) = V^{-1/2} e^{i\mathbf{p}_f\cdot\mathbf{r}/\hbar} \quad (90)$$

where the coefficient has been introduced for normalization, i.e. $\langle \psi_f | \psi_f \rangle = 1$ when the integration is performed over the allowable volume.

Taking $(2mE_f)^{1/2} = mv_f$, and integrating over energy in (88), we obtain:

$$dR = \frac{1}{4} \frac{q^2}{(2\pi\hbar c)^2} v_f |\mathbf{A}_0|^2 \left| \left\langle e^{-i\mathbf{p}_f \cdot \mathbf{r}/\hbar} \mid e^{i\mathbf{k} \cdot \mathbf{r}} \hat{\boldsymbol{\varepsilon}} \cdot \boldsymbol{\nabla} \mid \psi_i \right\rangle \right|^2 d\Omega. \quad (91)$$

The differential cross-section for this process is given by:

$$\frac{d\sigma}{d\Omega} = \frac{dR/d\Omega}{dN/dt dA} = \frac{dR/d\Omega}{\omega |\mathbf{A}_0|^2 / 8\pi\hbar c} \quad (92)$$

$$= \frac{q^2}{2\pi\hbar c} \frac{\nu_f}{\omega} \left| \left\langle e^{-i\mathbf{p}_f \cdot \mathbf{r}/\hbar} \mid e^{i\mathbf{k} \cdot \mathbf{r}} \hat{\boldsymbol{\varepsilon}} \cdot \boldsymbol{\nabla} \mid \psi_i \right\rangle \right|^2. \quad (93)$$

Actually, this expression is an approximation to the real photoionization cross-section because the liberated electron is not really “free” – it still feels the Coulomb attraction to the nucleus. A more accurate treatment would use a true continuum wave-function for the electron subject to the atomic potential. We will come back to this later.

2.9 Bound-Bound Transitions

In the case of bound-bound transitions, which give rise to emission or absorption lines, both the initial and final states are discrete. Equation (88) indicates that if the incoming wave is perfectly monochromatic, then the transition rate will be infinite if $\hbar\omega = |E_f - E_i|$, and zero otherwise. To derive a meaningful cross-section, we must integrate over a finite spectrum of the incident radiation field. This is characterized by a continuum photon flux, $dN/dtdAd\omega$. Setting:

$$|\mathbf{A}_0|^2 = \frac{8\pi\hbar c}{\omega} \frac{dN}{dtdAd\omega} d\omega \quad (94)$$

in (88) and integrating over frequency, yields:

$$R_{i \rightarrow f} = \frac{4\pi^2 q^2 \hbar}{m^2 c \omega_{if}} \frac{dN}{dtdAd\omega}(\omega_{if}) \left| \langle f \mid e^{\pm i\mathbf{k} \cdot \mathbf{r}} \hat{\boldsymbol{\varepsilon}}^* \cdot \boldsymbol{\nabla} \mid i \rangle \right|^2 \quad (95)$$

where $\omega_{if} \equiv |E_f - E_i|/\hbar$. Here again the (+) sign corresponds to absorption and the (−) sign to emission. The emission case is actually *induced* emission, since the transition rate is proportional to the incident flux. Because the radiation Hamiltonian operator is Hermitian, the rates for emission and absorption are identical (with the appropriate reversal of initial and final states).

Dividing the transition rate in (95) by the continuum flux yields a quantity with units of $\text{cm}^2 \text{ Hz}$, which is the cross-section integrated over frequency:

$$\frac{R_{i \rightarrow f}}{dN/dtdAd\omega} = \int \sigma(\omega) d\omega = 2\pi \int \sigma(\nu) d\nu. \quad (96)$$

This yields:

$$\int \sigma(\nu) d\nu = \left(\frac{\pi q^2}{mc} \right) \frac{2\hbar}{m\omega_{if}} |\langle f | e^{i\mathbf{k}\cdot\mathbf{r}} \hat{\boldsymbol{\varepsilon}} \cdot \boldsymbol{\nabla} | i \rangle|^2 . \quad (97)$$

Notice that the term within parentheses is the classical expression we had earlier (65). The remainder of the right hand side is the “quantum correction” to the classical result, and is called the *oscillator strength*, usually denoted by the symbol f :

$$f_{i \rightarrow f} \equiv \frac{2\hbar}{m\omega_{if}} |\langle f | e^{i\mathbf{k}\cdot\mathbf{r}} \hat{\boldsymbol{\varepsilon}} \cdot \boldsymbol{\nabla} | i \rangle|^2 . \quad (98)$$

2.10 The Quantum Multipole Expansion

The matrix element which appears in (98) involves the complex exponential factor: $e^{i\mathbf{k}\cdot\mathbf{r}}$. This is reminiscent of the classical expression (33) where we found it useful to expand this expression as a Taylor expansion in $\mathbf{k} \cdot \mathbf{r}$. The logic in the quantum calculation is the same: $\mathbf{k} \cdot \mathbf{r} \approx v/c$, where v is the characteristic velocity of oscillating charges in the system. For non-relativistic motions, this is a small parameter. In the lowest order limit, the electric dipole (E1) limit, we set the complex exponential to unity. The matrix element becomes:

$$\langle f | \hat{\boldsymbol{\varepsilon}} \cdot \boldsymbol{\nabla} | i \rangle = \frac{i}{\hbar} \hat{\boldsymbol{\varepsilon}} \cdot \langle f | \mathbf{p} | i \rangle \quad (99)$$

where \mathbf{p} is the momentum operator. Using the commutation relation:

$$[p^2, \mathbf{r}] = -2i\hbar\mathbf{p} = 2m [H^0, \mathbf{r}], \text{ we can rewrite this in the form:}$$

$$\begin{aligned} \langle f | \mathbf{p} | i \rangle &= \frac{mi}{\hbar} \langle f | [H^0, \mathbf{r}] | i \rangle \\ &= \frac{mi}{\hbar} (E_f - E_i) \langle f | \mathbf{r} | i \rangle = im\omega_{if} \langle f | \mathbf{r} | i \rangle . \end{aligned} \quad (100)$$

The (E1) expression for the oscillator strength is therefore:

$$f_{i \rightarrow f} = \frac{2m\omega_{if}}{\hbar} |\hat{\boldsymbol{\varepsilon}} \cdot \langle f | \mathbf{r} | i \rangle|^2 \quad (101)$$

Averaged over polarization directions, this becomes:

$$f_{i \rightarrow f} = \frac{2}{3} \frac{m\omega_{if}}{\hbar} |\langle f | \mathbf{r} | i \rangle|^2 . \quad (102)$$

A simple set of operator manipulations shows that the (E1) oscillator strengths satisfy a sum rule (the *Thomas-Reiche-Kuhn sum rule*):

$$\sum_f f_{i \rightarrow f} = Z \quad (103)$$

where Z is the number of bound electrons in the atom. This provides a useful limit on the oscillator strengths for highly excited transitions, which are numerous and therefore unwieldy to calculate. The next term in the multipole expansion has the form $\langle f | (\mathbf{k} \cdot \mathbf{r})(\hat{\boldsymbol{\epsilon}} \cdot \mathbf{p}) | i \rangle$, which, as in the classical case, can be broken into two pieces:

$$\begin{aligned} & 1/2 \langle f | (\mathbf{k} \cdot \mathbf{r})(\hat{\boldsymbol{\epsilon}} \cdot \mathbf{p}) - (\mathbf{k} \cdot \mathbf{p})(\hat{\boldsymbol{\epsilon}} \cdot \mathbf{r}) | i \rangle \\ & + 1/2 \langle f | (\mathbf{k} \cdot \mathbf{r})(\hat{\boldsymbol{\epsilon}} \cdot \mathbf{p}) + (\mathbf{k} \cdot \mathbf{p})(\hat{\boldsymbol{\epsilon}} \cdot \mathbf{r}) | i \rangle . \end{aligned} \quad (104)$$

The first term can be rewritten as:

$$(\mathbf{k} \times \hat{\boldsymbol{\epsilon}}) \cdot (\mathbf{r} \times \mathbf{p}) \sim \boldsymbol{\mu} \cdot \mathbf{B} \quad (105)$$

where $\boldsymbol{\mu}$ is the magnetic dipole moment of the orbiting electron. This is the magnetic dipole term (M1). For atomic transitions, we need to include both orbital and intrinsic spin contributions to the magnetic dipole moment. The second term above gives rise to electric quadrupole (E2) transitions. Here again, (M1) and (E2) transitions are of the same order in v/c . The (E1) term always dominates unless the matrix element of the position vector vanishes between the initial and final states. Transitions for which this is the case are called “electric dipole forbidden”, or simply “forbidden”. This condition gives rise to certain “selection rules” for (E1) transitions, which we discuss later in the context of atomic structure. Transitions for which the expression in (98) vanishes to all orders in $(\mathbf{k} \cdot \mathbf{r})$ are called “strictly forbidden”. These can only go by two-photon decay.

2.11 Spontaneous Emission

The quantum theory summarized so far only works for induced transitions, where an external electromagnetic field is introduced as a perturbation. This is because the treatment is semi-classical, i.e. the radiation field is still modeled classically even though the radiating system is treated quantum mechanically. Spontaneous emission, in which a system in an excited state decays on its own by emitting a photon, does not occur in this picture because the initial state involves no radiation field, so there is no perturbing Hamiltonian. The correct treatment of this process requires the quantization of the radiation field. That is straightforward, but too time-consuming to review here. However, another form of semi-classical argument can be invoked to derive what turns out to be the correct result. In the (E1) limit, our classical expression for the radiated power is given by (38). For an oscillator at a particular frequency:

$$|\ddot{\mathbf{d}}|^2 = \omega^4 (|\tilde{\mathbf{d}}(\omega)|^2 + |\tilde{\mathbf{d}}(-\omega)|^2) = 2\omega^4 |\tilde{\mathbf{d}}(\omega)|^2 . \quad (106)$$

Using (35), we can write this in terms of the integrated current density:

$$|\tilde{\mathbf{d}}(\omega)|^2 = \frac{1}{\omega^2} |\mathbf{j}_0|^2 \quad (107)$$

where $\mathbf{j}_0 \equiv \int d^3\mathbf{r}' \tilde{\mathbf{j}}(\mathbf{r}', \omega)$ Thus:

$$\frac{dW}{dt} = \frac{4}{3} \frac{\omega^2}{c^3} |\mathbf{j}_0|^2 . \quad (108)$$

In quantum mechanics, the charge density for a point charge is $\varrho = q |\psi(\mathbf{r})|^2$. From the continuity equation (5) and the time-dependent Schroedinger equation (67), it can be shown that the current density must be given by:

$$\mathbf{j} = -\frac{iq\hbar}{2m} [\psi^* \nabla \psi - \psi \nabla \psi^*] . \quad (109)$$

An appropriate “quantization” of the classical expression (108) can thus be obtained by setting:

$$|\mathbf{j}_0|^2 = \left| \int d^3\mathbf{r}' \left(\frac{-iq\hbar}{2m} \right) [\psi_f^* \nabla \psi_i - (\nabla \psi_f)^* \psi_i] \right|^2 \quad (110)$$

$$= \frac{q^2}{m^2} |\langle f | \mathbf{p} | i \rangle|^2 \quad (111)$$

$$= \frac{q^2 \omega_{if} \hbar}{2m} f_{i \rightarrow f} \quad (112)$$

where $f_{i \rightarrow f}$ is the electric dipole oscillator strength of (102). The resulting expression for the decay rate is then:

$$A_{i \rightarrow f} = \frac{1}{\hbar \omega_{if}} \frac{dW}{dt} = \frac{2}{3} \frac{q^2 \omega_{if}^2}{m c^3} f_{i \rightarrow f} \quad (113)$$

Comparison with (60) shows that this is simply the expression for the radiative decay rate of the classical oscillator multiplied by the absorption oscillator strength.

3 The Structure of Multi-Electron Atoms

3.1 Introduction

This chapter is devoted to the structure of multi-electron atoms. This is a vast and complex subject and time limitations will unfortunately prevent me from going into any real depth on most of the topics I will cover. My main focus will be on defining the relevant terms and outlining the basic principles and approximations which are used in modern atomic physics calculations. I will not discuss computational techniques or the specifics of particular codes.

Once again, I assume that much of this material is familiar to the reader from undergraduate and graduate courses in quantum mechanics.

The physics of atomic structure basically involves the solution of the time-independent Schroedinger equation:

$$H\psi = E\psi \quad (114)$$

where H is the Hamiltonian operator, E the energy and ψ is the wave-function for the electrons in the atom, usually expressed as a function of spatial and spin coordinates. For all but the simplest atoms, this equation is not analytically solvable and various approximation techniques are required. The most common, and most general is time-independent perturbation theory, in which one writes the Hamiltonian in terms of two parts:

$$H = H^0 + H^1 \quad (115)$$

a zeroth-order Hamiltonian H^0 , which is amenable to direct solution and an additional perturbation H^1 which has much smaller amplitude. In first order perturbation theory, the corrections to the energy levels due to the presence of the perturbation are given by:

$$\Delta E_n^{(1)} = \left\langle \psi_n^{(0)} \mid H^1 \mid \psi_n^{(0)} \right\rangle \quad (116)$$

where $\psi_n^{(0)}$ is the zeroth-order wave-function associated with the n -th energy level, E_n , and the corrections to the wave-functions are given by

$$\Delta\psi_n^{(1)} = \sum_{k \neq n} \frac{\left\langle \psi_k^{(0)} \mid H^1 \mid \psi_n^{(0)} \right\rangle}{E_k^{(0)} - E_n^{(0)}} \psi_k^{(0)}. \quad (117)$$

The zeroth-order wave-functions are orthonormal by construction and the perturbed wave-functions remain orthonormal to lowest order in H^1 .

Another approach which is frequently used for more complex atoms is the *Ritz variational method*. Its utility follows from the fact that the expectation value of the Hamiltonian with respect to an arbitrary normalized wave-function ψ , $\langle \psi \mid H \mid \psi \rangle$, is a minimum when ψ is the ground state eigenfunction of H . Even more generally, if the functional $\langle \psi \mid H \mid \psi \rangle$ is *stationary* with respect to perturbations in ψ , then ψ must be an eigenfunction of H . Typically, one uses this method by choosing a form for a trial wave-function characterized by a set of adjustable parameters and then minimizing the expectation value of the Hamiltonian with respect to those parameters.

3.2 Hydrogen-like Ions

We will begin the discussion with a quick review of the structure of hydrogen-like ions or one-electron atoms. Hydrogen-like ions are important for a number of reasons. First, in the non-relativistic limit, the time-independent

Schrodinger equation is exactly solvable so we can get analytic expressions for all important quantities. Second, the “hydrogenic approximation” is often useful for orders of magnitude estimates of rates for important processes and for simple scaling laws with the nuclear charge Z . Finally, hydrogen-like ions are quite important contributors to the soft X-ray emission from astrophysical plasmas. Indeed, the brightest lines are usually Lyman series transitions from hydrogen-like oxygen, neon, silicon and other low- Z elements.

The non-relativistic Hamiltonian for a single electron in an attractive central potential is given by:

$$H = \frac{p^2}{2m_e} - V(r) . \quad (118)$$

Making the usual substitution: $\mathbf{p} = -i\hbar\nabla$ we get the relevant form of (114):

$$\left(-\frac{\hbar^2}{2m_e} \nabla^2 - V(r) \right) \psi(\mathbf{r}) = E\psi(\mathbf{r}) . \quad (119)$$

It is convenient to use *atomic units* where the natural unit of length is the *Bohr radius*: $a_0 \equiv \hbar^2/me^2 = 0.529 \cdot 10^{-8}$ cm, and the natural unit of energy is twice the Rydberg constant: $e^2/a_0 \equiv 2Ry = 27.2$ eV = $4.36 \cdot 10^{-11}$ erg. In these units, $e = \hbar = m = 1$.

Equation (119) then takes the form:

$$\left(\frac{1}{2} \nabla^2 + E + V(r) \right) \psi(\mathbf{r}) = 0 . \quad (120)$$

Equation (120) is spherically symmetric, so it is useful to write it in spherical coordinates. A spherically symmetric Hamiltonian commutes with the total angular momentum operator $\mathbf{l} = \mathbf{r} \times \mathbf{p}$, which implies that eigenstates of H are also eigenstates of l^2 and l_z . In spherical coordinates (120) becomes:

$$\left(\frac{1}{2} \left[\frac{1}{r^2} \left(r \frac{\partial}{\partial r} \right) \left(r \frac{\partial}{\partial r} \right) + \frac{1}{r} \frac{\partial}{\partial r} - \frac{l^2}{r^2} \right] + E + V(r) \right) \psi = 0 . \quad (121)$$

The only dependence on the angular coordinates (ϑ, φ) in this expression is the l^2 term. That implies that the equation is separable and ψ can be written as a product of radial and angular parts:

$$\psi(r, \vartheta, \varphi) \equiv \frac{R(r)}{r} Y(\vartheta, \varphi) . \quad (122)$$

The eigenfunctions of l^2 and l_z are called *spherical harmonics* and have the form:

$$Y_{lm}(\vartheta, \varphi) \equiv \left[\frac{(l-|m|)!}{(l+|m|)!} \frac{2l+1}{4\pi} \right]^{1/2} (-1)^{(m+|m|)/2} P_l^{|m|}(\cos\vartheta) e^{im\varphi} \quad (123)$$

where P_l^m is the associated Legendre Polynomial. The spherical harmonics obey the eigenvalue equations:

$$l^2 Y_{lm}(\vartheta, \varphi) = l(l+1) Y_{lm}(\vartheta, \varphi) \quad (124)$$

$$l_z Y_{lm}(\vartheta, \varphi) = m Y_{lm}(\vartheta, \varphi) \quad (125)$$

where l and m are integers, with $-l \leq m \leq l$.

After substitution of (122) into (121), we are left with the *radial equation*:

$$\left(\frac{1}{2} \frac{d^2}{dr^2} + \frac{1}{r} \frac{d}{dr} - \frac{l(l+1)}{2r^2} + E + V(r) \right) \frac{R(r)}{r} = 0. \quad (126)$$

For bound-states, $E < 0$, the solutions are discrete and are characterized by an integer index n called the *principal quantum number*. Bound-state wave-functions are only obtained for $n \geq l + 1$, so for a given principal quantum number, the only allowed angular momentum states are $l = 0, 1, 2, \dots, n - 1$. The radial eigenfunctions are thus characterized by the two indices n and l .

For the particular case of the Coulomb potential $V(r) = Z/r$, (126) is exactly solvable, and leads to the radial wave-functions:

$$R_{nl}(r) = - \left(\frac{Z(n-l-1)!}{n^2[(n+l)!]^3} \right)^{1/2} e^{-\rho/2} \rho^{l+1} L_{n+l}^{2l+1}(\rho) \quad (127)$$

where $\rho \equiv 2Zr/n$ and $L_{n+l}^{2l+1}(\rho)$ are associated Laguerre polynomials. The energy eigenvalues, in atomic units, have the form:

$$E_n = \frac{-Z^2}{2n^2} \quad (128)$$

and are independent of l . This is a unique property of the Coulomb potential.

The probability density of finding the electron in the radial range $r \rightarrow r + dr$ is given by $R_{nl}^2(r)$. Plots of this function for a few low order orbitals are given in Fig. 1. Several key features of these radial wave-functions are immediately apparent from the plots. First, most of the charge is concentrated in a spherical shell of moderate thickness, whose radius increases with n . This is expected classically, i.e. smaller binding energy is associated with larger orbits. Note that for a given n , the radius of this shell decreases with increasing l . Again, this is in line with classical expectations. For a fixed energy, smaller angular momentum implies an elliptical orbit with higher eccentricity, in which the electron spends most of its time further away from the nucleus. Finally, note that as r goes to zero, the probability density goes to zero for all but the $l = 0$ states. Hence only these states are appreciably affected by nuclear interactions.

Since the energy only depends on n for hydrogen-like ions, there are n degenerate l states for each value of n , and $2l + 1$ degenerate m states for each value of l . In addition, the electron is a spin 1/2 particle, so there are

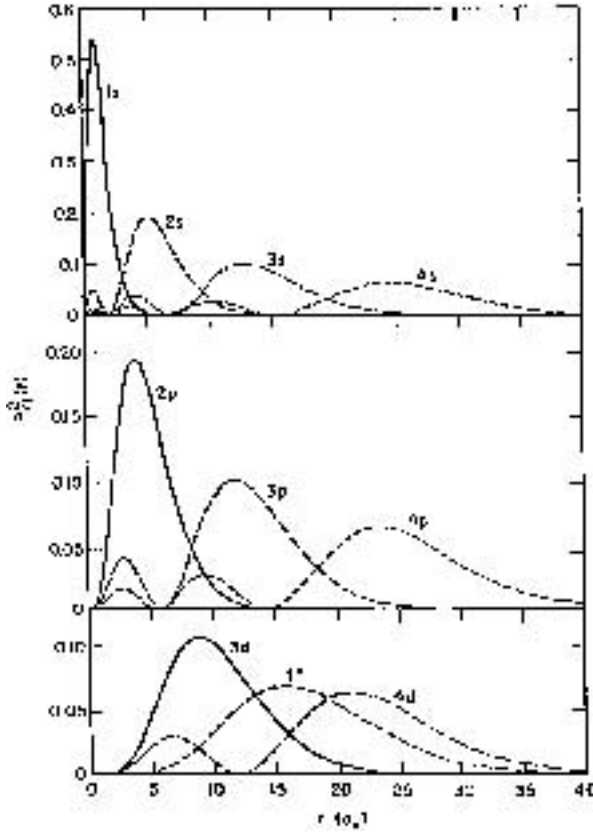


Fig. 1. Probability density to find the electron as a function of r (from Rybicki and Lightman, Fig. 9.1)

two degenerate spin states for each spatial state. The total degeneracy of level n is therefore given by:

$$g_n = 2 \sum_{l=0}^{n-1} (2l+1) = 2n^2 \quad (129)$$

3.3 Scaling with Nuclear Charge

It is useful, at this stage, to look at the scaling of various quantities with the nuclear charge Z . First note that the energy levels scale like Z^2 , which implies that the frequencies of key transitions also scale like Z^2 . The Lyman- α or $n = 2 \rightarrow 1$ transition, specifically, has photon energy given by:

$$\hbar\omega_{K\alpha} = (10.2 \text{ eV})Z^2. \quad (130)$$

Note that this line falls in the soft X-ray band (0.1–10 keV) for $Z = 3$ –31, which includes the abundant elements: C ($Z = 6$), N ($Z = 7$), O ($Z = 8$), Ne ($Z = 10$), Si ($Z = 14$), S ($Z = 16$), Ar ($Z = 18$), Ca ($Z = 20$) and Fe ($Z = 26$). The energy of this line is only slightly affected by the presence of additional electrons. So (130) gives a rough idea of the energies of all K-shell feature transitions down to $n = 1$, for these and other elements.

Transitions down to $n = 2$ are called L-shell transitions. For hydrogen-like ions, the brightest is the Balmer- α transition corresponding to $n = 3 \rightarrow 2$, whose energy is given by:

$$\hbar\omega_{L\alpha} = (1.89 \text{ eV})Z^2 \quad (131)$$

Note that the L-shell transitions for Fe fall close to 1 keV, in the center of the soft X-ray band. These are especially important for diagnostic purposes, as we will review in a subsequent chapter.

Equation (127) implies that the scaling of the radial wave-function is like Z^{-1} . Specifically, the characteristic size of hydrogen-like ions is given roughly by a_0/Z , where a_0 is the Bohr radius we defined earlier. Recall from (102) that the oscillator strength for an E1 transition is proportional to $\omega_{ij} |\langle f | \mathbf{r} | i \rangle|^2$. This scales like $Z^2 Z^{-2}$, and thus is independent of Z . The radiative decay rates for E1 transitions are proportional to $\omega^2 f$, so they scale like Z^4 .

The Coulomb potential for a hydrogen-like atom is proportional to $1/r$ so classically, the electron orbit obeys the Virial theorem, i.e. the kinetic energy is $-1/2$ times the potential energy:

$$\frac{1}{2}mv^2 = \frac{Ze^2}{2r}.$$

For the ground-state:

$$r \simeq \frac{a_0}{Z},$$

and thus:

$$v \simeq \left(\frac{Z^2 e^2}{ma_0} \right)^{1/2} = (Z\alpha)c \quad (132)$$

where $\alpha \equiv e^2/\hbar c \simeq 1/137$ is the fine structure constant. We saw earlier that the expansion parameter for both the classical and quantum multipole expansion ($\mathbf{k} \cdot \mathbf{r}$) $\sim v/c$, where v is a characteristic velocity of the system. For atomic transitions, we see that this parameter is $\sim Z\alpha$. The magnetic dipole and electric quadrupole terms are thus $\sim (Z\alpha)^2$ times smaller than electric dipole terms, so they scale like Z^6 . For low- Z abundant elements (C, N, O), $(Z\alpha)$ is indeed a small parameter. However for Fe, it is ~ 0.2 , so higher order multipole terms are non-negligible and can often be important in the spectrum.

3.4 Relativistic Corrections

The time independent Schroedinger equation as expressed in (119) assumes non-relativistic dynamics. For relativistic charges, one must use the Dirac equation instead. However, since $v/c \sim Z\alpha$, atomic electrons are only mildly relativistic, even for iron which is the highest Z abundant element. Thus, it is sufficient to use (119) and to treat relativistic corrections as a simple perturbation to the atomic structure.

To lowest order, there are three contributions to the relativistic corrections:

$$H_1^1 = -\frac{1}{8} \frac{p^4}{m_e^3 c^2} \quad (133)$$

which is the lowest order correction to the kinetic energy,

$$H_2^1 = \frac{1}{2m_e^2 c^2} \left(\frac{1}{r} \frac{dV}{dr} \right) \mathbf{l} \cdot \mathbf{s} , \quad (134)$$

the spin-orbit term, which represents the magnetic interaction between the magnetic dipole moment of the electron associated with its intrinsic spin and the magnetic field that it sees as it orbits in the electric field of the nuclear charge, and

$$H_3^1 = \frac{\hbar^2}{4m_e^2 c^2} \left(\frac{dV}{dr} \right) \frac{\partial}{\partial r} , \quad (135)$$

the so-called Darwin term, which is a relativistic correction to the potential energy produced by the non-localizability of the electron associated with its rest mass energy.

For the Coulomb potential in hydrogen-like atoms, a simple first order perturbation theory calculation using zeroth-order wave-functions yields the energy shift:

$$\Delta E_n = +E_n \frac{(Z\alpha)^2}{n^2} \left[\frac{n}{(j+1/2)} - \frac{3}{4} \right] \quad (136)$$

where j is the eigenvalue associated with the *total angular momentum* – specifically $j(j+1)\hbar^2$ is the eigenvalue of j^2 , where $\mathbf{j} = \mathbf{l} + \mathbf{s}$. The fact that the perturbed energies depend on j is a consequence of the spin-orbit term, which is proportional to the operator:

$$\mathbf{l} \cdot \mathbf{s} = \frac{1}{2} (j^2 - l^2 - s^2) . \quad (137)$$

Ignoring the relativistic corrections, eigenfunctions of the Hamiltonian for a one-electron central potential are simultaneous eigenfunctions of H_0 , l^2 , l_z , s^2 and s_z , so the states are characterized by the quantum numbers n , l , m_l , s , m_s . When the spin-orbit term is included however, l_z and s_z no longer commute with the Hamiltonian. The states are then characterized by n , l , s , j , m_j . We will see shortly that this has important consequences for the specification of the states in multi-electron atoms.

3.5 The Central Field Approximation and Quantum Indistinguishability

When there is more than one electron in the atom, the Schroedinger equation acquires an additional term due to the electron-electron repulsion:

$$\left(\frac{1}{2} \sum_j \nabla_j^2 + E + Z \sum_j \frac{1}{r_j} - \sum_{i>j} \frac{1}{|\mathbf{r}_i - \mathbf{r}_j|} \right) \psi(\{\mathbf{r}_j\}) = 0 \quad (138)$$

where \mathbf{r}_j is the position coordinate of the j th electron, $\nabla_j \equiv \partial/\partial\mathbf{r}_j$ and the sum is taken over all electrons. As indicated, the wave-function now depends on the set of all electron positions $\{\mathbf{r}_j\}$. Even for the case of just two electrons, (138) is impossible to solve analytically. The main problem is due to the coupling of all of the individual \mathbf{r}_j 's.

To make the problem tractable, some simplifying assumptions must be made. The most common is called the *central field approximation*. We partially account for the effects of the electron-electron repulsion by modifying the central potential, and then treat the residual electron-electron repulsion as a perturbation. That is, we define a zeroth order Hamiltonian by:

$$H_0 = -\frac{1}{2} \sum_j \nabla_j^2 + \sum_j V(r_j) \quad (139)$$

and a perturbing Hamiltonian by:

$$H' = \sum_{i>j} \frac{1}{|\mathbf{r}_i - \mathbf{r}_j|} - \sum_j \left(\frac{Z}{r_j} + V(r_j) \right). \quad (140)$$

Here $V(r)$ takes the form of a screened Coulomb potential. Close to the nucleus,

$$V(r) \rightarrow \frac{-Z}{r} + C$$

where C is a constant. Far from the nucleus

$$V(r) \rightarrow \frac{-(Z - N + 1)}{r}$$

where N is the number of electrons in the atom. The constant C enters in because the outer electrons approximate a uniformly charged sphere where the electron is close to the nucleus, and the potential inside a uniformly charged sphere is constant.

In the central field approximation, the zeroth order Hamiltonian given by (139) is the sum of single particle Hamiltonians, and thus the zeroth order wave-functions can be written as the product of single particle wave-functions:

$$\psi(\{\mathbf{r}_j\}) = \psi_1(\mathbf{r}_1)\psi_2(\mathbf{r}_2)\dots\psi_N(\mathbf{r}_N) \quad (141)$$

where the individual $\psi_j(\mathbf{r}_j)$ are solutions to the single electron Schroedinger equation:

$$\left(\frac{1}{2}\nabla_j^2 + E - V(\mathbf{r}_j)\right)\psi_j(\mathbf{r}_j) = 0 \quad (142)$$

and are individually characterized by the quantum numbers n , l , m_l , s , m_s . This would be sufficient if it were not for quantum indistinguishability. Because the atomic electrons form a system of *identical particles* and because they are fermions, the total wave-function must be anti-symmetric with respect to particle interchange. We can construct such an anti-symmetric wave-function by forming the following linear combination of product wave-functions:

$$\psi(\{\mathbf{r}_j\}) = \frac{1}{\sqrt{N!}} \sum_P (-1)^P \psi_1(\mathbf{r}_{j_1}) \psi_2(\mathbf{r}_{j_2}) \dots \psi_N(\mathbf{r}_{j_N}). \quad (143)$$

Here, in each term in the sum, the set of single-electron wave-functions is arranged in the same order, but the electron coordinates, $\mathbf{r}_{j_1}, \mathbf{r}_{j_2}, \dots, \mathbf{r}_{j_N}$ have been arranged in a new order which is a permutation of the original set.

The sum is taken over all possible permutations. For each permutation, P represents the number of interchanges. Thus $(-1)^P = +1$ for even permutations and -1 for odd permutations. The wave-function given by (143) is often written in terms of what is called a *Slater determinant*:

$$\psi(\{\mathbf{r}_j\}) = \frac{1}{\sqrt{N!}} \begin{vmatrix} \psi_1(\mathbf{r}_1) & \psi_2(\mathbf{r}_1) & \dots & \psi_N(\mathbf{r}_1) \\ \psi_1(\mathbf{r}_2) & \psi_2(\mathbf{r}_2) & \dots & \psi_N(\mathbf{r}_2) \\ \vdots & \vdots & \ddots & \vdots \\ \psi_1(\mathbf{r}_N) & \psi_2(\mathbf{r}_N) & \dots & \psi_N(\mathbf{r}_N) \end{vmatrix} \quad (144)$$

and is occasionally referred to as a *determinantal wave-function*. An important consequence of the anti-symmetrization is the *Pauli Exclusion Principle*: “No two electrons can occupy the same individual quantum state”. This can be seen to follow trivially from the Slater determinant. If two of the single particle wave-functions, ψ_i and ψ_j are identical then two columns in the matrix are identical and the determinant vanishes. The Pauli exclusion principle implies that for multi-electron atoms, even the ground state must involve electrons in the individual particle excited states. Recall that for principal quantum number n , there are $2n^2$ distinct spin and angular momentum states. If there are more than two electrons in the atom, at least some must be in an $n = 2$ or higher level. If there are more than ten electrons, some must be in an $n = 3$ or higher state.

The specification of the N individual particle quantum states for the set of N electrons is usually referred to as the *configuration*. The representation of the general wave-function $\psi(\{\mathbf{r}_j\})$ in terms of the Slater determinant is sometimes called the *single configuration approximation*.

3.6 Electron Exchange – Helium-like Atoms

A second important consequence of the anti-symmetrization of the wavefunction is the existence of what are called *electron exchange terms*. These are additional interaction terms which introduce spin dependence in the energy levels even when there is no explicit spin dependence in the Hamiltonian.

The key concepts are most simply illustrated by looking at the detailed level structure of helium-like atoms where there are two orbital electrons. The Hamiltonian for this system is:

$$H = -\frac{1}{2}\nabla_1^2 - \frac{1}{2}\nabla_2^2 - \frac{2}{r_1} - \frac{2}{r_2} + \frac{1}{r_{12}} \quad (145)$$

where $r_{12} \equiv |\mathbf{r}_1 - \mathbf{r}_2|$. The Hamiltonian is spin-independent, so the eigenfunctions are functions only of the \mathbf{r}_1 and \mathbf{r}_2 . However, because of the anti-symmetrization, there is a coupling to spin. Specifically, the total wavefunction can be written in only one of the two forms:

$$\psi = \varphi_S(\mathbf{r}_1, \mathbf{r}_2)\chi_A(m_{s1}, m_{s2}) \quad (146)$$

or

$$\psi = \varphi_A(\mathbf{r}_1, \mathbf{r}_2)\chi_S(m_{s1}, m_{s2}) . \quad (147)$$

Here φ denotes the *spatial* component of the wave-function, while χ denotes the *spin* component. The subscripts ‘‘S’’ and ‘‘A’’ indicate the symmetric and anti-symmetric combinations, respectively. Since the total wave-function must be anti-symmetric, one of the two must appear in a symmetric combination while the other must be anti-symmetric.

The symmetric spin-state is the so-called *triplet state*, where the total spin: $\mathbf{s} = \mathbf{s}_1 + \mathbf{s}_2$ has eigenvalue $s = 1$. This state has three-fold degeneracy; the degenerate eigenstate can be written in the form:

$$\begin{aligned} & |1/2, 1/2\rangle , \quad m_s = +1 \\ & \frac{1}{\sqrt{2}}(|1/2, -1/2\rangle + |-1/2, 1/2\rangle) , \quad m_s = 0 \\ & |-1/2, -1/2\rangle . \quad m_s = -1 \end{aligned}$$

Here the first index in each case is m_{s1} and the second index is m_{s2} . The anti-symmetric spin state is the *singlet state*, corresponding to $s = 0$. There is no degeneracy in this state. It can be written in the form:

$$\frac{1}{\sqrt{2}}(|1/2, -1/2\rangle - |-1/2, 1/2\rangle) . \quad m_s = 0$$

Invoking the central field approximation, we will treat the electron-electron repulsion term as the perturbation. For simplicity, we will take the central potential to be the simple Coulomb potential of the nuclear charge: $V(r) = -2/r$. In that case the spatial part of the wave-function is the product

wave-function of hydrogen-like eigenfunctions. The symmetric combination is:

$$\frac{1}{\sqrt{2}}(\varphi_1(\mathbf{r}_1)\varphi_2(\mathbf{r}_2) + \varphi_2(\mathbf{r}_1)\varphi_1(\mathbf{r}_2))$$

where φ_1 and φ_2 are each characterized by a particular choice of n , l , m_l . The anti-symmetric combination is:

$$\frac{1}{\sqrt{2}}(\varphi_1(\mathbf{r}_1)\varphi_2(\mathbf{r}_2) - \varphi_2(\mathbf{r}_1)\varphi_1(\mathbf{r}_2)) .$$

Now consider the ground state of the helium atom. Both of the electrons must be in the lowest energy orbital, corresponding to $n = 1$, $l = 0$. Since the two electrons are in the same spatial state, the spatial wave-function must be symmetric. In that case, the spin wave-function is anti-symmetric, so this is a singlet state. In first order perturbation theory, the correction to the energy level is given by:

$$\begin{aligned} \Delta E &= \left\langle \psi \left| \frac{1}{r_{12}} \right| \psi \right\rangle \\ &= \int d^3\mathbf{r}_1 d^3\mathbf{r}_2 |\varphi_{10}(\mathbf{r}_1)|^2 |\varphi_{10}(\mathbf{r}_2)|^2 \frac{1}{r_{12}} . \end{aligned} \quad (148)$$

This expression has a simple classical interpretation: since $|\varphi_{10}(\mathbf{r}_1)|^2$ and $|\varphi_{10}(\mathbf{r}_2)|^2$ represent the probability density of finding the electrons at positions \mathbf{r}_1 and \mathbf{r}_2 , respectively, this is just the weighted average of the electrostatic repulsion energy between them.

Next consider the first excited states. In this case, one of the electrons is in the $n = 1$, $l = 0$ orbital, while the other is in an $n = 2$, $l = 0, 1$ orbital. In this case, there are two possible spatial wave-functions:

$$\frac{1}{\sqrt{2}}(\varphi_{10}(\mathbf{r}_1)\varphi_{20}(\mathbf{r}_2) + \varphi_{20}(\mathbf{r}_1)\varphi_{10}(\mathbf{r}_2))$$

which corresponds to the spin singlet, and

$$\frac{1}{\sqrt{2}}(\varphi_{10}(\mathbf{r}_1)\varphi_{20}(\mathbf{r}_2) - \varphi_{20}(\mathbf{r}_1)\varphi_{10}(\mathbf{r}_2))$$

which corresponds to the spin triplet. The first order perturbation theory correction to the energy level now has two terms:

$$\begin{aligned} \Delta E &= \int d^3\mathbf{r}_1 d^3\mathbf{r}_2 |\varphi_{10}(\mathbf{r}_1)|^2 |\varphi_{20}(\mathbf{r}_2)|^2 \frac{1}{r_{12}} \\ &\quad \pm \int d^3\mathbf{r}_1 d^3\mathbf{r}_2 \varphi_{10}^*(\mathbf{r}_1)\varphi_{20}^*(\mathbf{r}_2)\varphi_{20}(\mathbf{r}_1)\varphi_{10}(\mathbf{r}_2) \frac{1}{r_{12}} \end{aligned} \quad (149)$$

where the (+) sign applies to the spin singlet combination and the (−) sign applies to the spin triplet. The first term has the same interpretation that we saw

earlier; it is the weighted average of the electrostatic repulsion energy. However, the second term is new. It appears because of the anti-symmetrization of the wave-function and is generally referred to as the *electron exchange term*. It can be shown that the integral for this term is always positive, so the triplet state has always lower energy. Thus the lowest excited state of helium-like atoms are spin triplet states.

A simple interpretation of the exchange energy is as follows: for a spin triplet combination, the spatial wave-function is anti-symmetric, so the Pauli exclusion principle requires that the electrons stay further apart. In that case, the electrostatic repulsion energy is reduced. For a spin singlet, the electrons are closer together on average and the electrostatic repulsion energy is enhanced.

3.7 Approximation Techniques for Multi-Electron Atoms

For more complicated multi-electron atoms, the electron-electron interaction is a significant perturbation and some form of approximation scheme is required to calculate wave-functions and energy levels. Within the context of the central field approximation, the simplest approach is to assume a central $V(r)$ which suitably accounts for the effects of electron shielding, and then to use this potential to calculate the single electron wave-functions which are the basic ingredients for the Slater determinant wave-function appropriate to the whole atom. Final wave-functions and energy levels are computed using first order perturbation theory, with the perturbation given by (140).

An early candidate functional form for the central potential was the *Thomas-Fermi potential* derived from a statistical treatment of the electron cloud as a gas of free-particle degenerate fermions at zero temperature. The potential is calculated classically from an assumed continuous charge density $\rho(\mathbf{r})$ and the form of $\rho(\mathbf{r})$ is adjusted so as to achieve a minimum in the total (kinetic plus potential) energies. This model yields moderately accurate energy levels for the valence shells of multi-electron near-neutral atoms, where the semi-classical assumptions involved are most reliable.

A more modern, and more accurate approach is to assume a convenient analytic form for the potential such as:

$$V(r) = -\frac{2}{r}((N-1)e^{-\alpha_1 r} + \alpha_2 r e^{-\alpha_2 r} + \dots + \alpha_{N-1} r^k e^{-\alpha_N r} + Z - N + 1) \quad (150)$$

characterized by the adjustable set of parameters: $\alpha_1, \alpha_2, \dots, \alpha_N$. For a given configuration, the values of the α_i 's are determined by minimizing the total energy of the atom. This yields a unique form for the potential for each electron configuration. That is sufficient for calculating energy levels. However, for the calculations of matrix elements (such as oscillator strengths), a common potential must be chosen, or otherwise the wave-functions describing initial and final states are not necessarily orthonormal. The *parametric*

potential method is computationally fast, and has been shown to yield reasonably accurate results, especially for highly charged ions, which are the dominant contributors to astrophysical X-ray spectra.

The most accurate conventional approach however is the *Hartree-Fock* or *self-consistent field* method. Here one takes a direct account of the dependence of the individual electron wave-functions on one another, which is brought about by the electron-electron repulsion term. The governing equations can be derived from the Ritz variational principle, i.e. using total wave-functions, ψ , constructed as Slater determinants of individual electron wave-functions, φ_i , we minimize the quantity $\langle \psi | H | \psi \rangle$ (where H is the total Hamiltonian) subject to the constraint that the individual wave-functions remain orthonormal. This can be accomplished by introducing N Lagrange multipliers ε_i , such that:

$$\delta(\langle \psi | H | \psi \rangle - \sum_i \varepsilon_i \langle \varphi_i | \varphi_i \rangle) = 0. \quad (151)$$

The result is a set of N equations (the Hartree-Fock equations) which look like Schrodinger equations, but with potentials that depends on the wave-function solutions:

$$\left[-\frac{1}{2}\nabla_i^2 - \frac{Z}{r_i} + \sum_{j \neq i} \int d^3\mathbf{r}_j \frac{|\varphi_j(\mathbf{r}_j)|^2}{|\mathbf{r}_i - \mathbf{r}_j|} \right] \varphi_i(\mathbf{r}_i) - \sum_{j \neq i} \delta(m_{s_i}, m_{s_j}) \\ \times \left[\int d^3\mathbf{r}_j \frac{1}{|\mathbf{r}_i - \mathbf{r}_j|} \varphi_j^*(\mathbf{r}_j) \varphi_i(\mathbf{r}_j) \right] \varphi_j(\mathbf{r}_i) = \varepsilon_i \varphi_i \mathbf{r}_i. \quad (152)$$

Here m_{s_i} and m_{s_j} are the eigenvalues of s_z for the i th and j th orbitals in the electron configuration, respectively. The first two terms on the left-hand side of (152) are associated with the single particle Hamiltonian ignoring the electron-electron interaction. The third term comes from the electron-electron repulsion energy. The fourth term is due to the exchange energy. It is zero unless the two orbitals have the same spin ($\delta(m_{s_i}, m_{s_j}) = 1$), so that the spatial part of the wave-function is anti-symmetric.

For a given set of *trial* wave-functions $\varphi_i^{(0)}(\mathbf{r})$, the set of (152) can be solved to yield a new set of wave-functions $\varphi_i^{(1)}(\mathbf{r})$. This is repeated until it converges, i.e. until the resulting set of eigenfunction solutions is “close” to the trial set. The process yields a self-consistent potential for the electron-electron interaction which can then be used to calculate energy levels and matrix elements.

Hartree-Fock calculations are generally time-consuming and unwieldy in comparison to the simpler parametric potential methods discussed earlier. In addition, the self-consistent potential is not always smooth and well-behaved which can complicate the calculation of relativistic corrections (134 and 135) that are important for highly charged ions.

3.8 LS, jj and Intermediate Coupling

The Hamiltonian for the multi-electron atom as incorporated in (138) is rotationally invariant. In addition, it has no explicit spin dependence. This means that H must commute with the operators \mathbf{J} , \mathbf{L} and \mathbf{S} :

$$[H, \mathbf{J}] = [H, \mathbf{L}] = [H, \mathbf{S}] = 0 \quad (153)$$

where \mathbf{L} is the total orbital angular momentum of all the electrons in the atom: $\mathbf{L} = \sum_i \mathbf{l}_i$, \mathbf{S} is the total spin angular momentum: $\mathbf{S} = \sum_i \mathbf{s}_i$ and \mathbf{J} is the total angular momentum: $\mathbf{J} = \mathbf{L} + \mathbf{S}$. Hence, the eigenstates of H must also be eigenstates of J^2 , J_z , L^2 , L_z , S^2 and S_z and will thus be characterized by definite values of the corresponding eigenvalues: J , M_J , L , M_L , S , M_S , in addition to the energy E .

However, in the central field approximation, we have constructed the eigenfunctions out of single-electron wave-functions, which are themselves eigenfunctions of l^2 , l_z , s^2 , s_z , and are thus characterized by the eigenvalues l , m_l , s , m_s . The simple product wave-functions which comprise the Slater determinant will be characterized by a set of definite eigenvalues $l^{(i)}$, $m_l^{(i)}$, $s^{(i)}$, $m_s^{(i)}$ for each of the electrons in the atom. But L^2 does not commute with the individual $l_z^{(i)}$ operators and S^2 does not commute with the individual $s_z^{(i)}$. Hence these simple products cannot be eigenfunctions of the total Hamiltonian including the electron-electron repulsion.

Product states of definite L , M_L , S , M_S can however be generated by ‘‘coupling’’ individual product wave-functions into suitable superpositions. Here one uses the usual rules of angular momentum addition in quantum mechanics, and the coefficients of the various terms are given by Clebsch-Gordan coefficients. One first couples the spatial wave-functions individually into states of definite L^2 and L_z and the spin wave-functions individually into states of definite S^2 and S_z . One couples their product together to yield states of definite J^2 and J_z . This is called an *LS coupling scheme* or sometimes *Russell-Saunders coupling*.

The anti-symmetrization of the wave-function involves a superposition over permutations of the electron coordinates. Coupling involves a superposition over different values of $m_l^{(i)}$ and $m_s^{(i)}$. In principle, one can anti-symmetrize first and couple afterwards or couple first and anti-symmetrize afterwards. In practice, the latter is usually easier. The calculation of the matrix elements using these anti-symmetrized, coupled wave-functions can be quite complex if carried out by brute force. Fortunately, there is an elegant mathematical formalism known as *Racah algebra* – developed by Racah and Wigner in the 1940’s – which greatly simplifies the angular part of these matrix elements.

The discussion above ignores the relativistic corrections covered in Sect. 3.4. In particular, the spin-orbit term (134) in the single electron Hamiltonian is proportional to the operator $\mathbf{l} \cdot \mathbf{s}$, which does not commute with l_z and s_z , but

does commute with j^2 and j_z . When this term is important, it is convenient to first couple the individual particle wave-functions into states of definite $j^{(i)}$, $m_j^{(i)}$ and then couple these states into states of definite J , M_J . This is known as jj-coupling.

jj-coupling is formally incompatible with LS-coupling because states of definite L^2 , L_z , S^2 , S_z are not characterized by definite values of $j^{(i)}$, $m_j^{(i)}$. In practice, LS-coupling is preferred whenever the electron-electron repulsion term dominates over the spin-orbit terms. This is especially true for low- Z atoms which are not highly ionized. jj-coupling would be preferred for high- Z atoms with only a few electrons. In cases where both electron-electron and spin-orbit terms are important, neither scheme is entirely appropriate. In that case, one chooses one or the other as the basis, and then diagonalizes the “other” perturbing operator in this basis to achieve the appropriate superpositions. This is known as *intermediate coupling*. The final eigenstates are then only characterized by definite values of J and M_J .

3.9 Spectroscopic Notation and Ground-State Configurations

In LS-coupling, a given electron configuration is specified by the quantum numbers $n^{(i)}$, $l^{(i)}$, $s^{(i)}$ for each of the individual electrons and the total quantum numbers L , S , J , M_J for the atom as a whole. In the absence of an external field, the energy levels are degenerate in M_J so this is usually not included. In addition, all electrons have $s = 1/2$, so this too need not be indicated. Over the years, a notational scheme has become standard for designating these configurations. Specifically, for a given nl “shell” the number of electrons in that shell is indicated as an exponent. Recall that there are $2(2l + 1)$ distinct states in such a shell, so the exponent cannot exceed that number. For historical reasons, l is not indicated as an integer, but instead as a letter, with the assignments:

$$\begin{array}{cccccccc} l = & 0 & 1 & 2 & 3 & 4 & 5 & \dots \\ \text{symbol} & s & p & d & f & g & h & \dots \end{array}$$

Thus the notation $3d^24f$ indicates two electrons with principal quantum number $n = 3$ and angular momentum $l = 2$ and one electron with $n = 4$ and $l = 3$.

For the total quantum numbers, the standard notation has the form

$${}^{2S+1}L_J.$$

Here again a letter is used in place of a number for L and the convention is the same as that used for the individual l 's only with upper case letters instead of lower case. Thus the designation ${}^2D_{3/2}$ indicates a state with $S = 1/2$, $L = 2$ and $J = 3/2$.

For X-ray emitting astrophysical plasmas, we are mainly concerned with few electron atoms, specifically K- and L-shell ions, isoelectronic with the

neutral elements hydrogen through neon. Only a few key ideas are required to understand the ground configuration of such ions.

1. For a Coulomb potential, we have seen that the energy levels only depend on n not l . This is not true of the screened Coulomb potential appropriate to multi-electron atoms. The lower the angular momentum, the higher the probability that the electron is close to the nucleus where it “sees” less screening of the nuclear charge and hence the lower the energy. The energy therefore increases strongly with n and/or l .
2. Because of the strong dependence on n and l , as electrons are added to an ion, they continue to fill n, l “shells” until they are closed. A shell is closed when all of its magnetic spatial and spin orbitals are filled. A closed shell therefore has J, L and S all equal to zero.
3. For a partially open shell, the state of highest S will have the lowest energy. This is a consequence of the exchange energy, as we saw earlier. If S is maximal, the spin wave-function must be symmetric, which means that the spatial wave-function is anti-symmetric, and the electrons are on average further apart, thereby lowering their repulsion energy.
4. If the partially open shell is less than half-full, the lowest energy state will have the lowest possible value of J . This is a consequence of the spin-orbit interaction, which contributes positive energy that increases with J .
5. If the open shell is more than half-full, it is easier to think in terms of the electron “holes” rather than the electrons. These behave like positive electrons. Their spin-orbit contribution then has opposite sign. As a result, the lowest energy state has the highest possible J .

Using these rules, one can understand now the ground-states of hydrogen-like through neon-like ions have the following configurations:

H:	$1s$	$^2S_{1/2}$
He:	$1s^2$	1S_0
Li:	$1s^2 2s$	$^2S_{1/2}$
Be:	$1s^2 2s^2$	1S_0
B:	$1s^2 2s^2 2p$	$^2P_{1/2}$
C:	$1s^2 2s^2 2p^2$	3P_0
N:	$1s^2 2s^2 2p^3$	$^4S_{3/2}$
O:	$1s^2 2s^2 2p^4$	3P_2
F:	$1s^2 2s^2 2p^5$	$^2P_{3/2}$
Ne:	$1s^2 2s^2 2p^6$	1S_0

In cases of intermediate coupling, which is important for highly charged ions, it is sometimes useful to also indicate the j -values of the individual electrons. This is done by adding a subscript to the individual shell terms indicating the value of j . Since the spin-orbit interaction for an individual electron has the lowest energy for the lowest values of j , the lower j states are filled first. Thus, in this notation, the ground configuration of oxygen-like ions is represented by $1s^2 2s^2 2p_{1/2}^2 2p_{3/2}^2$. Of course, for intermediate coupling, the L and S values

are not precisely defined. Typically, one lists the notation for the leading term in the LS expansion.

3.10 Configuration Interaction

In Sect. 3.5 we introduced the central field approximation and the associated single configuration approximation, where the total wave-function is written as an anti-symmetrized product of single-electron wave-functions. It should be emphasized that this is an approximation – it is by no means clear that the exact multi-electron eigenfunction of the total Hamiltonian is close to a single configuration wave-function, i.e. to a single Slater determinant. When this is not true, we need to allow for configuration mixing, by forming multi-configuration superpositions derived from matrix elements of the Hamiltonian. Codes which include these effects are called *multi-configuration* calculations.

It is impractical of course to include a large number of configurations in constructing the basis set. However, some guidance comes from the structure of the Hamiltonian. In LS-coupling, only configurations of common L , S , J and parity need be included. In addition, since the Hamiltonian only contains terms involving one or two electrons, interactions can only occur between configurations that differ in at most two orbitals.

Configuration interaction tends to be strong between configurations which are close in energy. For the highly charged ions important in X-ray emitting plasmas, the energy levels are more weakly dependent on l . Thus significant mixing can occur between configurations like $3s^23p^k$ and $3p^{k+2}$. In such cases, the identification of a particular transition with a set of upper and lower configurations is not very meaningful.

3.11 Selection Rules for Radiative Transitions

The matrix elements which appear in the various terms in the multipole expansion for radiative transitions can vanish for particular choices of initial and final states. This gives rise to what are called *selection rules* for the various multipole transitions. Transitions which violate the selection rules are called *forbidden*, while those consistent with the selection rules are *allowed*.

First, consider *electric dipole* transitions. Here the matrix element is $\langle f|\mathbf{r}i\rangle$, where $\mathbf{r} = \sum_i \mathbf{r}_i$. Since \mathbf{r} is a sum of single electron operators, this matrix element will vanish if the initial and final configurations differ by more than one electron orbital. Hence, only single electron transitions are allowed. Second, note that \mathbf{r} has odd parity. Thus initial and final states must have opposite parity. Finally, since in spherical coordinates \mathbf{r}_i can be written as a superposition of the spherical harmonics with $l = 1$, it is easy to show that this matrix element also vanishes unless $\Delta l = \pm 1$ for the change in the single electron orbital. The essential selection rules are $\Delta l = \pm 1$, $\Delta s = 0$, $\Delta L = 0, \pm 1$, $\Delta S = 0$, $\Delta J = 0, \pm 1$, with $J = 0 \rightarrow 0$ strictly forbidden.

Second, for *magnetic dipole* transitions, the matrix element is $\langle f | \boldsymbol{\mu} | i \rangle$, where $\boldsymbol{\mu}$ is the magnetic dipole moment. Including spin contributions, $\boldsymbol{\mu} \sim \mathbf{L} + 2\mathbf{S} = \mathbf{J} + \mathbf{S}$. Since \mathbf{J} commutes with H , $\langle f | \mathbf{J} | i \rangle = 0$, so we are only left with $\langle f | \mathbf{S} | i \rangle$. This is a pure spin operator, so the net spatial configuration cannot change. Ignoring relativistic terms, \mathbf{S} also commutes with H . However, the spin-orbit interaction introduces some mixing. The selection rules are $\Delta S = 0, \pm 1$ (spin flip), $\Delta J = 0, \pm 1$, no $J = 0 - 0$, no parity change, no change in configuration (i.e. $\Delta n = 0$, $\Delta l = 0$ for all electrons).

And third, for *electric quadrupole* transitions, the selection rules are: $\Delta l = 0, \pm 2$, $\Delta L = 0, \pm 1, \pm 2$, $\Delta J = 0, \pm 1, \pm 2$, no $J = 0 - 0$, no change in parity.

When configuration interaction is important, these selection rules can appear to be violated because of mixing. That is, even if the dominant configurations in the initial and final states violate the selection rules, there may be small admixtures in each case that do contribute to a non-zero matrix element.

4 Electron-Ion Collisional Processes

4.1 Overview

In the previous two chapters, I have laid out the essential ingredients for the calculation of radiative transitions rates between various energy levels and for the atomic structure effects which give rise to the particular characteristics of those levels. To predict the emergent X-ray spectra of astrophysical plasmas, however, we also need to understand the details of how excited atomic levels are populated. For the most part, that involves the study of electron-ion collisional processes in plasmas. This is also a rich and diverse field and it will not be possible to do justice to the full complexity of this topic. My emphasis, as in the previous chapter, will be on the explication of key concepts, definition of terms commonly used in the atomic physics literature and presentation of some quick back-of-the-envelope type calculations that enable us to derive rough estimates of the rate coefficients for these processes.

Each electron-ion collisional process is accompanied by a quantum mechanical *inverse*, which can be viewed as the same process *time-reversed*. Not surprisingly, the rates for direct and inverse processes involve common matrix elements, and are therefore related. The easiest way to derive these relations is to resort to *detailed balance* arguments, i.e. to set the rates for direct and inverse processes equal in strict thermodynamic equilibrium. I will defer an extensive discussion of thermodynamic equilibrium to the next chapter, but we will anticipate some important results from that discussion and utilize them here.

There are essentially four key electron-ion collisional processes that are important for X-ray emitting plasmas. These are schematically illustrated

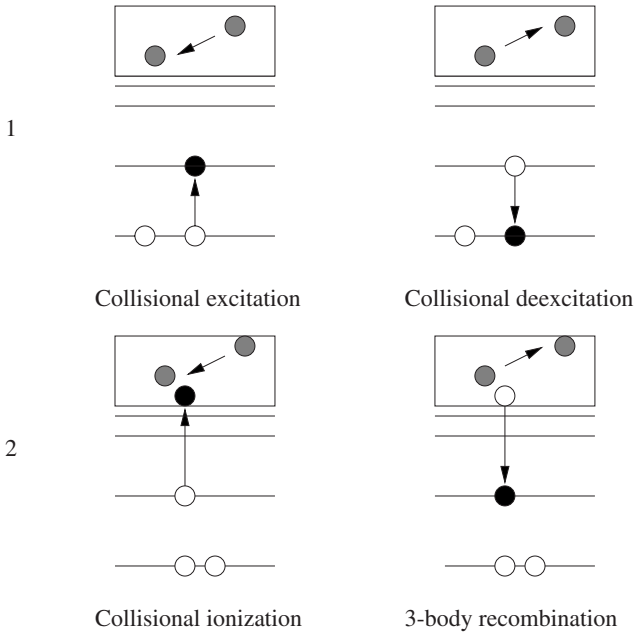


Fig. 2. The first two of the four key electron-ion collisional processes. The “inverse” process is on the right

in Figs. 2 and 3 where the “direct” process is depicted on the left and the “inverse” process on the right.

Collisional Excitation/Deexcitation

In collisional excitation, the interaction between a passing electron in a *continuum state* and a bound electron in a discrete state results in the excitation of the bound electron to a higher energy discrete level. To conserve energy, the colliding electron gives up a fraction of its energy and thus “falls” into a lower continuum state. The inverse process is collisional deexcitation, where a passing electron interacting with an excited atom actually gains energy as a result of the collision.

Collisional Ionization/3-Body Recombination

Collisional ionization is similar to collisional excitation, except that in this case, the final state of the initially bound electron is also a continuum state. The inverse process is 3-body recombination. Here, two, initially free electrons interact with the ion in the same collision. One of the two gets captured into a bound discrete level, while the other carries off the excess energy in a higher continuum state.

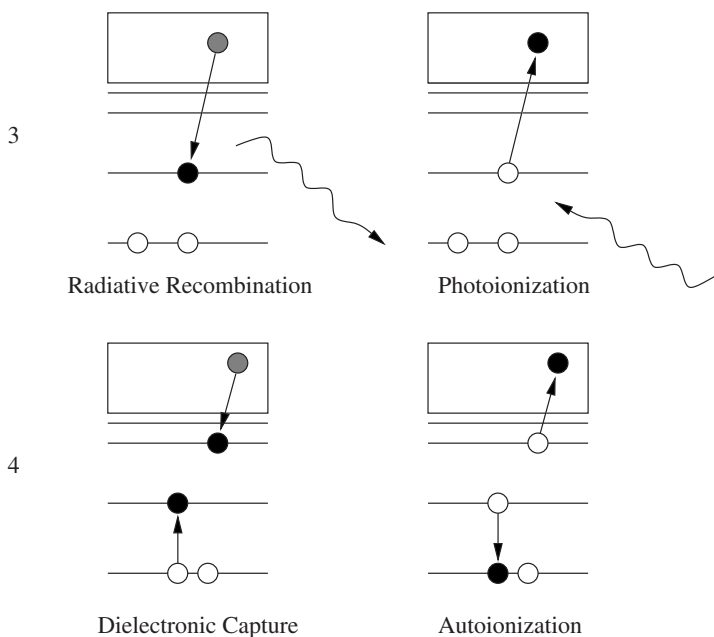


Fig. 3. The last two of the four key electron-ion collisional processes

Radiative Recombination/Photoionization

In radiative recombination a free electron in a continuum state decays into a bound discrete state through the emission of a photon. This is actually a form of spontaneous emission, similar to what we discussed for the radiative decay between two bound levels in Sect. 2.9. The inverse process is photoionization, or bound-free absorption, as discussed in Sect. 2.8.

Dielectronic Capture/Autoionization

Dielectronic capture is a resonant radiationless process in which the decay of an electron from a continuum state to a bound state is accompanied by the elevation of a core electron into an excited state. The resulting atom is doubly excited, and it has a total energy above the ionization potential of the initial ion. The inverse process is autoionization, where a doubly excited atom decays via the emission of a weakly bound outer electron. If the core excitation is associated with a “hole”, in one of the orbitals of an inner shell, this process is usually called *Auger decay*.

In the remainder of this chapter, I will review each of these processes in somewhat more detail.

4.2 Collisional Excitation – Scattering Theory

Collisional excitation is essentially an example of inelastic scattering of an electron off a complex atomic potential, and thus much of the formalism of quantum scattering theory can be applied to this process. Typically, one expresses the continuum wave-function at large distances from the atom as the sum of an incident plane wave and an outgoing spherical wave:

$$\varphi_c(\mathbf{r})_{r \rightarrow \infty} \simeq A \left[e^{i\mathbf{k}_i \cdot \mathbf{r}} + f(\vartheta, \varphi) \frac{e^{i\mathbf{k}_f \cdot \mathbf{r}}}{r} \right] \quad (154)$$

where $\hbar\mathbf{k}_i$ is the initial momentum of the electron, $\hbar^2 k_i^2/2m$ is its initial energy and $\hbar^2 k_f^2/2m$ is its final energy. The flux in the wave is given by:

$$\mathbf{j}(\mathbf{r}) = \frac{\hbar}{2mi} [\varphi^*(\nabla\varphi) - (\nabla\varphi^*)\varphi] \quad (155)$$

(see (109)). For the incident wave, this gives:

$$j_{in} = \frac{\hbar k_i}{m} |A|^2 . \quad (156)$$

For the outgoing wave:

$$\begin{aligned} \mathbf{j}_{out} \cdot \mathbf{r} &= \frac{\hbar}{2mi} \left[\varphi^* \frac{\partial \varphi}{\partial r} - \frac{\partial \varphi^*}{\partial r} \varphi \right] \\ &= \frac{\hbar k_f}{m} \frac{|A|^2 |f|^2}{r^2} . \end{aligned} \quad (157)$$

The number of scattered electrons in solid angle element $d\Omega$ is: $(\mathbf{j}_{out} \cdot \mathbf{r})r^2 d\Omega$. Therefore, the differential cross-section for scattering is:

$$\frac{d\vartheta}{d\Omega} = \frac{(\mathbf{j}_{out} \cdot \mathbf{r})r^2}{j_{in}} = \frac{k_f}{k_i} |f(\vartheta, \varphi)|^2 , \quad (158)$$

f is called the *scattering amplitude*.

If we limit our consideration to single electron transitions, then the total wave-function can be expressed in terms of product wave-functions for the colliding electron and the bound transitioning electron. These are still identical particles, so the total wave-function must be anti-symmetrized. Due to the exchange terms (see below), we get different answers for the singlet state and the triplet state. Averaging over the four possible spin states, the differential cross-section will then look like:

$$\frac{d\vartheta}{d\Omega} = \frac{k_f}{k_i} \left[\frac{1}{4} |f^+|^2 + \frac{3}{4} |f^-|^2 \right] \quad (159)$$

where the (+) indicates a symmetric spatial wave-function and the (–) indicates an anti-symmetric spatial wave-function.

The calculation of the scattering amplitude proceeds as follows: we write the total wave-function as the sum of anti-symmetrized product wave-functions for the initial and final states:

$$\begin{aligned} \psi = & \left[\varphi_{c_i}^{\pm}(\mathbf{r}_1) \varphi_{b_i}(\mathbf{r}_2) \pm \varphi_{c_i}^{\pm}(\mathbf{r}_2) \varphi_{b_i}(\mathbf{r}_1) \right] \\ & + \left[\varphi_{c_f}^{\pm}(\mathbf{r}_1) \varphi_{b_f}(\mathbf{r}_2) \pm \varphi_{c_f}^{\pm}(\mathbf{r}_2) \varphi_{b_f}(\mathbf{r}_1) \right] \end{aligned} \quad (160)$$

where $\varphi_{c_{i,f}}^{\pm}$ are the initial and final wave-functions for the colliding electron and $\varphi_{b_{i,f}}$ are the initial and final wave-functions for the bound electron. ψ must satisfy the Schrodinger equation:

$$\left[-\frac{1}{2} \nabla_1^2 - \frac{1}{2} \nabla_2^2 + V(r_1) + V(r_2) + \frac{1}{r_{12}} \right] \psi = E_{tot} \psi . \quad (161)$$

Therefore, if we take a scalar product with $\varphi_{b_i}^*(\mathbf{r}_2)$ we must get:

$$\int d^3 \mathbf{r}_2 \varphi_{b_i}^*(\mathbf{r}_2) \left[-\frac{1}{2} \nabla_1^2 - \frac{1}{2} \nabla_2^2 + V(r_1) + V(r_2) + \frac{1}{r_{12}} - E \right] \psi = 0 . \quad (162)$$

But

$$\left[-\frac{1}{2} \nabla_2^2 + V(r_2) \right] \varphi_{b_i}(\mathbf{r}_2) = E_{b_i} \varphi_{b_i}(\mathbf{r}_2) , \quad (163)$$

and

$$E_{tot} = E_{b_i} + \frac{\hbar^2 k_i^2}{2m} . \quad (164)$$

Substitution of (160) into (162) yields

$$\begin{aligned} (\nabla_1^2 + k_i^2) \varphi_{c_i}^{\pm}(\mathbf{r}_1) = & 2 \left[V_{ii}(\mathbf{r}_1) \varphi_{c_i}^{\pm}(\mathbf{r}_1) + V_{if}(\mathbf{r}_1) \varphi_{c_f}^{\pm}(\mathbf{r}_1) \right] \\ \pm 2 \left[\int d^3 \mathbf{r}_2 K_{ii}(\mathbf{r}_1, \mathbf{r}_2) \varphi_{c_i}^{\pm}(\mathbf{r}_2) + \int d^3 \mathbf{r}_2 K_{if}(\mathbf{r}_1, \mathbf{r}_2) \varphi_{c_f}^{\pm}(\mathbf{r}_2) \right] \end{aligned} \quad (165)$$

where

$$V_{ii} \equiv V(\mathbf{r}_1) + \left\langle \varphi_{b_i} \left| \frac{1}{r_{12}} \right| \varphi_{b_i} \right\rangle \quad (166)$$

$$V_{if} \equiv \left\langle \varphi_{b_i} \left| \frac{1}{r_{12}} \right| \varphi_{b_f} \right\rangle \quad (167)$$

$$K_{ii}(\mathbf{r}_1, \mathbf{r}_2) \equiv \varphi_{b_i}^*(\mathbf{r}_1) \varphi_{b_i}(\mathbf{r}_2) \left[\frac{1}{r_{12}} - E_{tot} - E_{b_i} \right] \quad (168)$$

$$K_{if}(\mathbf{r}_1, \mathbf{r}_2) \equiv \varphi_{b_i}^*(\mathbf{r}_1) \varphi_{b_f}(\mathbf{r}_2) \left[\frac{1}{r_{12}} - E_{tot} - E_{b_i} - E_{b_f} \right] \quad (169)$$

The terms involving the V 's are the direct potential terms, the K 's are the exchange terms. A second similar equation can be obtained (with the i 's and

f's reversed) by taking the scalar product with $\varphi_{b_f}^*$ in place of $\varphi_{b_i}^*$ in (162). The result is a set of two coupled equations which can be solved simultaneously for $\varphi_{c_i}^\pm$ and $\varphi_{c_f}^\pm$ given expressions for φ_{b_i} and φ_{b_f} . They are analogous to the Hartree-Fock equations for a two electron atom. Once the continuum wave-functions are found, the scattering amplitudes can be computed and we obtain the cross-section.

The exchange terms can be important at low collision energies, especially for electric dipole forbidden transitions. At high energies, the continuum wave-functions, φ_{c_i} and φ_{c_f} oscillate strongly in comparison to the slowly varying K-functions and so the integrals on the right-hand side of (165) tend to vanish.

This procedure is still an approximation since we have not allowed the colliding electron to influence the bound-state wave-functions. One approach to correcting this is to include in the trial wave-function (160) other terms allowing for other proper collision channels, involving other sets of bound excited states. That is called a *close coupling calculation* since it couples in other states of the atom. It results in a much larger set of simultaneous equations, depending on how many channels are included.

At energies well above threshold, a much simpler calculation can be performed using the *Born approximation*. Here one assumes plane-wave wave-functions for both the initial and final continuum states. The transition rate can be calculated from time-dependent perturbation theory (see (70)) taking the electron-electron interaction as the perturbing potential:

$$\begin{aligned} R &= \frac{2\pi}{\hbar} \left| \left\langle f \left| \frac{e^2}{|\mathbf{r}_1 - \mathbf{r}_2|} \right| i \right\rangle \right|^2 \delta(E_f - E_i) \\ &= \left| \frac{2\pi}{\hbar} \frac{1}{V^2} \int_V d^3\mathbf{r}_1 d^3\mathbf{r}_2 e^{-i\mathbf{k}_f \cdot \mathbf{r}_2} \varphi_{b_f}^*(\mathbf{r}_1) \frac{e^2}{|\mathbf{r}_1 - \mathbf{r}_2|} \varphi_{b_i}^*(\mathbf{r}_1) e^{i\mathbf{k}_i \cdot \mathbf{r}_2} \right|^2 \\ &\quad \times \delta(E_f - E_i) \end{aligned} \quad (170)$$

where we have normalized the plane waves over a finite volume V .

Because exchange effects were found to be small at higher energies, one usually does not need to bother anti-symmetrizing the wave-function. The total rate is found by summing over the trial states of the outgoing electrons so that the δ -function gets replaced by a density of states factor:

$$\rho_f = \frac{V}{2\pi^2} \left(\frac{2m}{\hbar^2} \right) k_f. \quad (171)$$

The total rate thus scales like $1/V$. However, the incident flux is given by v_i/V in this picture, so the total cross-section is independent of the assumed volume, as expected.

A similar, but somewhat improved calculation can be obtained using continuum wave-functions of the Coulomb potential of the ion in place of the plane-waves. This is called the *Coulomb-Born method*. Even better yet is to

use the continuum wave-functions derived from the effective central potential $V(r)$ of the atom. That is the *distorted wave approach*. Usually distorted wave radial wave-functions are calculated in a *partial wave expansion*, summing over states of definite orbital angular momentum l . Close to threshold, the energy of the outgoing electron is low and only a small number of terms in the partial wave expansion need be kept. The maximum l required can be roughly estimated from classical considerations:

$$L \approx p_f a \Rightarrow l \approx k_f a \quad (172)$$

where a is the characteristic dimension of the atom. At high impact energies, many partial waves are required and the plane-wave Born approach provides a much simpler alternative.

The integral which appears in the plane-wave Born approximation (170), can be simplified using *the Bethe integral*:

$$\int d^3\mathbf{r} \frac{e^{i\mathbf{\Delta}\cdot\mathbf{r}}}{r} = \frac{4\pi}{\Delta^2} \quad (173)$$

which implies that the excitation cross-section is proportional to the square of a matrix element given by:

$$\frac{1}{\Delta^2} \int d^3\mathbf{r} \varphi_{b_f}^*(\mathbf{r}) e^{i\mathbf{\Delta}\cdot\mathbf{r}} \varphi_{b_i}(\mathbf{r}) \quad (174)$$

where $\mathbf{\Delta} \equiv \mathbf{k}_i - \mathbf{k}_f$. Note that the expression in (174) can be approximated by a multipole expansion:

$$e^{i\mathbf{\Delta}\cdot\mathbf{r}} \approx 1 + i(\mathbf{\Delta}\cdot\mathbf{r}) + \dots \quad (175)$$

entirely analogous to the multipole expansion invoked for radiative transitions in Sect. 2.10. Here again, $\mathbf{\Delta}\cdot\mathbf{r} \approx \mathbf{k}\cdot\mathbf{r} \approx v/c$, so for non-relativistic electrons, only the lowest order non-vanishing term usually needs to be considered. We thus obtain selection rules for collisional excitation between bound levels which are identical to the selection rules for radiative transitions between those levels. Therefore, transitions that are electric dipole forbidden also have low cross-section for collisional excitation. The above argument, however, relies on the plane-wave Born calculations, ignoring exchange effects. Generally, exchange terms dominate the cross-section for higher order multipole transitions.

4.3 Collisional Excitation – Classical Estimate

The discussion in Sect. 4.2 provides a sketch of how accurate collisional excitation cross-sections are calculated using sophisticated atomic codes, but is not especially helpful for getting quick quantitative estimates of the magnitude of collisional excitation rates. For this, it is more useful to resort to

simple classical arguments. Imagine a passing electron interacting via the Coulomb force with one of the orbital electrons in the atom. The momentum transfer to the bound electron is approximately:

$$\Delta p \approx \int_0^\infty dt F(t) \approx \frac{e^2}{b^2} \left(\frac{2b}{v} \right) = \frac{2e^2}{bv} \quad (176)$$

where b is the impact parameter of the colliding electron, and $\tau = 2b/v$ is the characteristic duration of the interaction. Thus, the energy transfer to the bound electron is:

$$\Delta E \approx \frac{(\Delta p)^2}{2m} \approx \frac{2e^4}{mb^2 v^2}. \quad (177)$$

The energy transfer must equal the energy of the excitation $\Delta E \approx E_{mn}$, where we are considering a transition from initial state m to final state n . The cross-section at impact parameter b is $\sigma \approx \pi b^2$ so:

$$\sigma_{mn} \approx \frac{2\pi e^4}{mv^2 E_{mn}} = \frac{\pi e^4}{E_e E_{mn}} \quad (178)$$

where E_e is the energy of the colliding electron. In atomic units:

$$\sigma_{mn}(E_e) \approx \frac{4\pi a_0^2}{E_e E_{mn}} \quad (179)$$

where a_0 is the Bohr radius.

It is traditional to express the cross-section in terms of a *collision strength* Ω_{mn} which is specific to the transition, but relatively independent of the electron energy:

$$\sigma_{mn}(E) \equiv \frac{\pi a_0^2}{g_m E_e} \Omega_{mn} \quad (180)$$

where g_m is the degeneracy of the initial state. One thus sees that classically $\Omega_{mn} \approx 4g_m/E_{nm}$. The quantum mechanical treatment (for electric dipole transitions) gives:

$$\frac{\Omega_{mn}}{g_m} = \frac{8\pi}{\sqrt{3}} \frac{f_{mn}\bar{g}}{E_{mn}} \quad (181)$$

where f_{mn} is the dipole absorption oscillator strength for the transition, and \bar{g} is a *Gaunt factor* which is ≈ 1 for $\Delta n = 0$ transitions, and ≈ 0.2 for $\Delta n \neq 0$ transitions.

In thermal plasmas, collisional excitation can be characterized by a rate coefficient $C_{mn}(T)$, which is a function of electron temperature and is specific to the transition. The rate of collisional excitations for transition m to n per unit volume is given by $n_e n_i^m C_{mn}(T)$ where n_e is the free electron density and n_i^m is the density of the relevant ion in state m . In terms of the cross-section:

$$C_{mn}(T) = \int_{v_0}^\infty dv v f(v, T) \sigma_{mn}(v) \quad (182)$$

where $v_0 = (2E_{mn}/m)^{1/2}$ is the threshold velocity for the transition and $f(v, T)$ is the Maxwellian velocity distribution appropriate to a thermal plasma:

$$f(v, T) = 4\pi \left(\frac{m}{2\pi kT} \right)^{3/2} v^2 e^{-mv^2/2kT}. \quad (183)$$

The integration yields:

$$\begin{aligned} C_{mn}(T) &= \left(\frac{\pi a_0^2}{g_m} \right) \left(\frac{2kT}{\pi m_e} \right)^{1/2} \left(\frac{2Ry}{kT} \right) \Omega_{mn} e^{-E_{mn}/kT} \\ &\approx \frac{8.6 \cdot 10^{-6}}{g_m} T^{-1/2} \Omega_{mn} e^{-E_{mn}/kT} \text{ cm}^3/\text{s} \end{aligned} \quad (184)$$

where T is now in K.

The inverse of collisional excitation is collisional deexcitation. The principle of detailed balance asserts that in thermodynamic equilibrium, the rates for a process and its inverse must be equal. The rate for collisional excitation is $n_e n_i^m C_{mn}(T)$. The rate for collisional deexcitation is $n_e n_i^n C_{nm}(T)$. But in thermodynamic equilibrium, the level populations are related by the degeneracies and the Boltzmann factor:

$$\frac{n_i^n}{n_i^m} = \frac{g_n}{g_m} e^{-E_{mn}/kT}. \quad (185)$$

Thus:

$$\begin{aligned} C_{nm}(T) &= C_{mn}(T) \frac{g_m}{g_n} e^{E_{mn}/kT} \\ &= \frac{8.6 \cdot 10^{-6}}{g_n} T^{-1/2} \Omega_{nm} \text{ cm}^3/\text{s} \end{aligned} \quad (186)$$

where $\Omega_{nm} = \Omega_{mn}$. Note that for isoelectronic sequences, Ω_{nm} scales like $E_{nm}^{-1} \sim Z^{-2}$. In contrast, we saw earlier (Sect. 3.3) that radiative decay rates scale like Z^4 . Thus, for X-ray emitting plasmas, whose spectra are dominated by higher Z ions, we need very high electron densities before collisional deexcitation competes with spontaneous radiative decay.

4.4 Collisional Ionization

Collisional ionization is essentially the same process as collisional excitation except that the final state of the initially bound electron is now also a continuum state. The general quantum formalism outlined in Sect. 4.2 can clearly be applied to this case as well. With two continuum states in the final state, the square of the matrix element in (170) is proportional to $1/V^3$ instead of $1/V^2$ but there are now two density of states factors instead of one, so the final expression for the cross-section is still independent of the assumed volume.

As in the case of collisional excitation, there is a simple classical calculation that can be invoked to provide a rough estimate of the cross-section. This is originally due to Thomson and dates back to 1912 (before the discovery of the electron!). Thomson calculated the energy transfer between two same charges, assuming one is initially at rest:

$$\Delta E = \frac{E}{\left[1 + \frac{E^2 b^2}{e^2}\right]} \quad (187)$$

where E is the energy of the colliding electron and b is the impact parameter. Setting $\Delta E \geq \chi$, where χ is the ionization potential of the atom, one finds $b \leq b_c$, where:

$$b_c = \frac{e}{E} \left(\frac{E}{\chi} - 1\right)^{1/2}. \quad (188)$$

The cross-section is thus given by:

$$\sigma = \pi b_c^2 = \pi e^2 \frac{1}{E^2} \left(\frac{E}{\chi} - 1\right) = (4\pi a_0^2) \frac{1}{E^2} \left(\frac{E}{\chi} - 1\right) \quad (189)$$

where the last expression is in atomic units, with E given in Rydbergs. This is a classical ionization cross-section per electron. It must be summed over all the electrons in the atom, using the appropriate χ value for each atomic shell and only including shells for which $E \geq \chi$.

This Thomson exchange cross-section provides a surprisingly good estimate of the true cross-section for $E \gg \chi$, but it gives a significant overestimate near threshold. This is due essentially to two effects:

1. The calculation ignores the initial binding energy of the target electron;
2. It does not allow for the possibility that if too much energy is transferred, the colliding electron itself becomes bound.

Hutchinson [7] suggests a simple modification that partially corrects for these two effects:

$$\sigma = 4\pi a_0^2 \frac{1}{E(E + E_+)} \left(\frac{E}{\chi} - 1\right) \quad (190)$$

where E_+ is an adjustable parameter which is approximately a few times χ .

The cross-section given in (190) can be integrated analytically over a Maxwellian distribution (as in 182) to yield a rate coefficient. The result involves an exponential integral, but Hutchinson shows that to a good approximation one obtains:

$$\begin{aligned} C(T) &= \langle \sigma v \rangle = 4\pi a_0^2 \left(\frac{8kT}{\pi m}\right)^{1/2} \frac{Ry^2}{\chi(\chi + E_+)} e^{-\chi/kT} \left[1 - e^{-(\chi + E_+)/kT}\right] \\ &\approx (8.5 \cdot 10^{-8}) \left[\frac{Ry^2}{\chi(\chi + E_+)}\right] \left[\frac{kT}{Ry}\right]^{1/2} e^{-\chi/kT} \left[1 - e^{-(\chi + E_+)/kT}\right] \text{ cm}^3 \text{ s}^{-1}. \end{aligned} \quad (191)$$

Similar (but not identical) formulae have been derived empirically from fits to experimental data by Lotz [8] and others. These generally agree with one another to within a factor of two.

The inverse of collisional ionization is 3-body recombination. However, since this process involves the collision of two electrons with the atom in the same interaction, it is usually only important at very high densities ($n_e \geq 10^{19} \text{ cm}^{-3}$), which rarely apply to X-ray emitting astrophysical plasmas.

4.5 Radiative Recombination

Radiative recombination involves the capture of a free electron, accompanied by the emission of a photon with energy given by:

$$\hbar\omega_n = E + \chi_n \quad (192)$$

where E is the initial energy of the electron, and χ_n is the ionization potential of the level into which the electron is captured. Since this is a radiative process, it may be calculated using the techniques outlined in Chap. 2. In particular, we can get a quick semi-quantitative estimate of the cross-section from a classical treatment, where we view radiative recombination as a kind of discrete limit of classical bremsstrahlung, the radiation emitted by an electron as it is accelerated in the Coulomb field of an ion. The energy emitted per unit frequency per unit time per unit volume due to bremsstrahlung by electrons of velocity v is given by:

$$\frac{dW}{d\omega dV dt} = \frac{16\pi e^6}{3\sqrt{3}c^3 m^2 v} n_e n_i Z^2 g \quad (193)$$

where n_e is the electron density, n_i is the ion density, Z is the charge on the ion and g is a Gaunt factor of order unity (see [2]). For radiative recombination, the final state of the electron is discrete, so the energy radiated must all come out at a single frequency given by (192). We may thus write:

$$\frac{dW_n}{dV dt} = \frac{16\pi e^6}{3\sqrt{3}c^3 m^2 v} n_e n_i Z^2 g(\Delta\omega_n) \quad (194)$$

where $(\Delta\omega_n)$ is the frequency difference between two neighboring shells. Adopting an ‘‘hydrogenic approximation’’ for the energy levels:

$$\chi_n \approx \frac{Z^2 Ry}{n^2} \quad (195)$$

$$\Delta\omega_n = \frac{2Z^2 Ry}{\hbar n^3} \approx \frac{2\chi_n}{\hbar n} . \quad (196)$$

We define a cross-section $\sigma_n(v)$ by setting:

$$\frac{dW_n}{dV dt} = n_e n_i v \sigma_n(v) \hbar\omega_n . \quad (197)$$

Plugging in the relevant expressions from (192), (194) and (195) and solving for $\sigma_n v$ yields:

$$\sigma_n(v)v = \frac{16\pi e^6 Z^2 g}{3\sqrt{3}c^3 m^2} \frac{2\chi_n}{n} \frac{1}{(\frac{1}{2}mv^2 + \chi_n)} \frac{1}{v}. \quad (198)$$

Finally, averaging over a Maxwellian velocity distribution yields a rate coefficient as a function of temperature:

$$\alpha(T) \equiv \langle \sigma_n(v)v \rangle \approx (5.2 \cdot 10^{-14}) g Z^2 \left(\frac{\chi_n}{kT} \right)^{3/2} e^{\chi_n/kT} E_i \left(\frac{\chi_n}{kT} \right) \text{ cm}^3 \text{ s}^{-1} \quad (199)$$

where $E_i(x)$ is the exponential integral.

To get more accurate estimates from a quantum mechanical calculation, it is usually easier to first calculate the photoionization cross-section and then resort to a detailed balance argument to find the cross-section for radiative recombination. Let $\sigma_{PI}(\omega)$ be the photon cross-section for photoionization at frequency ω and let $\sigma_{RR}(v)$ be the electron cross-section for radiative recombination at electron velocity v . As we have seen, ω and v are related by energy conservation (192) with $E = 1/2 mv^2$. Let n_i be the density of the i th ionic species and n_{i+1} be the density of the one higher ionization state. Then the rate of recombinations per unit volume in the velocity range v to $v + dv$ is given by:

$$dR_{RR}(v) = n_e \sigma_{RR}(v) v f(v) dv n_{i+1} \quad (200)$$

where $f(v)$ is the Maxwellian electron distribution in velocity. The rate of photoionizations per unit volume in the frequency range ω to $\omega + d\omega$ is given by:

$$dR_{PI}(\omega) = \frac{F(\omega)d\omega}{\hbar\omega} \sigma_{PI}(\omega) n_i (1 - e^{-\hbar\omega/kT}) \quad (201)$$

where $F(\omega)$ is the energy flux per unit frequency in the radiation field. In thermodynamic equilibrium, this is given by the expression:

$$F(\omega) = \frac{\hbar\omega^3}{\pi^2 c^2} \frac{1}{(e^{\hbar\omega/kT} - 1)} \quad (202)$$

(see Sect. 5). The last factor which appears in (201) is a correction for stimulated emission – in thermodynamic equilibrium, there are always photon-induced radiative decays in addition to spontaneous radiative decays. Thus (201) gives a *net* photoabsorption rate. Using the expression we had earlier for the Maxwellian distribution (183), and equating the rates in (200) and (201) yields:

$$\frac{\sigma_{PI}(\omega)}{\sigma_{RR}(v)} = \frac{n_e n_{i+1}}{n_i} \left(\frac{m}{2\pi kT} \right)^{3/2} v^3 e^{-(mv^2/2 - \hbar\omega)/kT} \frac{dv}{d\omega}. \quad (203)$$

But $1/2 mv^2 - \hbar\omega = -\chi$ and $dv/d\omega = (d\omega/dv)^{-1} = \hbar/mv$. The ratio of the densities is given by the Saha equation which we will introduce in the next chapter:

$$\frac{n_e n_{i+1}}{n_i} = \frac{2g_{i+1}}{g_i} \left(\frac{mkT}{2\pi\hbar^2} \right)^{3/2} e^{-\chi/kT} \quad (204)$$

where g_{i+1} is the degeneracy of the final state of the more highly ionized ion, and g_i is the degeneracy of the less ionized ion (see Sect. 5). Collecting terms yields:

$$\frac{\sigma_{PI}(\omega)}{\sigma_{RR}(v)} = \frac{m^2 c^2 v^2}{\hbar^2 \omega^2} \frac{g_{i+1}}{g_i} \quad (205)$$

which is called the *Milne relation*.

The quantum mechanical calculation of photoionization cross-sections was discussed in Sect. 2.8. For hydrogen-like ions, we can obtain an analytical expression. Averaging over l , the cross-section for ionization out of the n th shell is given by:

$$\sigma_n(\omega) = \frac{64\alpha}{3^{3/2}} \frac{Z^4}{n^5} \left(\frac{Ry}{\hbar\omega} \right)^3 \pi a_0^2 g \quad (206)$$

[if $\hbar\omega > Z^2 Ry/n^2$ and is zero otherwise] where g is again a Gaunt factor of order unity. The ω^{-3} dependence is also typical of photoionization cross-sections of more complex atoms. The monochromatic emissivity (energy radiated per unit volume per unit frequency) associated with recombination radiation is given by:

$$\begin{aligned} \frac{dW}{dt d\omega dV} &= n_e n_{i+1} (\hbar\omega) v f(v) \sigma_{RR}(v) \frac{dv}{d\omega} = \left(\frac{2}{\pi} \right)^{1/2} n_e n_i \frac{g_i}{g_{i+1}} \\ &\times \left(\frac{\hbar\omega}{\chi} \right)^3 \left(\frac{\chi^2}{mc^2 kT} \right)^{3/2} \hbar c \sigma_{PI}(\omega) e^{-\hbar\omega/kT} e^{\chi/kT}. \end{aligned} \quad (207)$$

Notice that for $\sigma_{PI}(\omega) \sim \omega^{-3}$, the frequency dependence is essentially exponential above threshold.

4.6 Dielectronic Recombination and Autoionization

Dielectronic capture involves the capture of a free electron into a bound level with the accompanying excitation of a core electron. The resulting recombined atom is doubly excited. It can decay by autoionization, ejecting the captured electron back out into the continuum. In that case, there is no net change in the level of ionization of the atom. However, the doubly excited atom can also decay radiatively, thereby lowering its total energy below the ionization potential of the recombined atom. When this occurs, the recombination is complete and the atom is left in a stable configuration with one extra electron. The complete process – dielectronic capture followed by radiative decay is usually referred to as *dielectronic recombination*. This can be

a very important process in astrophysical plasmas, especially for ions, as we shall see shortly.

Let's first consider the inverse process, autoionization. Its rate (from time dependent perturbation theory) is given by:

$$A_a = \frac{2\pi}{\hbar} \left| \left\langle f \left| \frac{e}{|r_i - r_j|} \right| i \right\rangle \right|^2 \quad (208)$$

where f and i represent the appropriate product wave-functions for the two electrons involved in the interaction in the initial and final states. Note that in the final state, one of the electrons is in a continuum state. Since the continuum states have wave-functions which are normalized to a delta-function in energy, this wave-function has units of energy^{-1/2}. Therefore, the square of the matrix element has units of energy, not energy-squared, as one would otherwise expect. When divided by \hbar , it gives a finite rate.

The matrix element which appears in the autoionization decay rate (208) is the same matrix element one would use to calculate the configuration interaction between the doubly bound level and the continuum level with equal energy. In some sense, autoionization is a consequence of configuration interaction. The diagonalized eigenstate of the perturbation is then a superposition of the initial discrete state and a range of continuum states:

$$\psi = a\psi_{discrete} + \int dEb(E)\psi_{continuum}(E) \quad (209)$$

with the coefficient a and $b(E)$ determined by the configuration interaction matrix-element. It can be shown (see [1] pp. 526–535) that the width of the function $b(E)$ is given roughly by $A_a\hbar$, as one would expect based on the energy-time uncertainty principle. The autoionization process by assigning a finite lifetime to the doubly excited level, broadens this level into a narrow continuum whose width is inversely related to that lifetime.

The presence of the configuration interaction also gives rise to characteristic absorption line profiles for photoionization in the vicinity of autoionizing resonances. The continuum state can, of course, be reached by photoexcitation of a core electron. If there were no configuration interaction, these two processes would be distinct and the photoabsorption spectrum would consist of a discrete absorption line on a photoionization continuum, as shown in Fig. 4, left panel. However, with configuration interaction, the final state wave-function is as given in (209), and we get interference between the two channels. The photoabsorption spectrum in this case looks like Fig. 4, right panel, which is called a Beutler-Fano absorption profile. Such features are expected in the extreme ultraviolet spectra of nearby white dwarf stars due to photoabsorption by neutral helium in the intervening interstellar medium [9]. The features so far observed have been associated with autoionizing resonances of neutral helium.

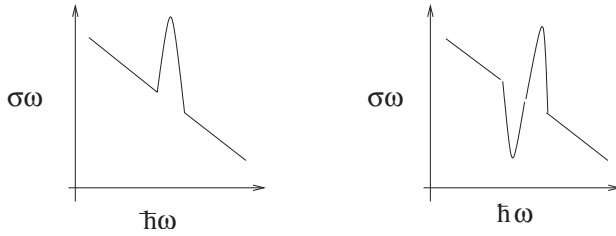


Fig. 4. Spectra without configuration interaction (*left*) and Beutler-Fano profile (*right*)

Note that using the simple Z -scaling arguments we invoked earlier, autoionization decay rates are roughly independent of Z for isoelectronic sequences. This is because the outgoing continuum wave-function is proportional to $E^{-1/2} \sim Z^{-1}$, while the perturbation Hamiltonian $\sim r^{-1} \sim Z^{+1}$. Thus, the matrix element is $\sim Z^0$. This means that autoionization is extremely important for low Z ions, but becomes less and less important in comparison to radiative decay for high Z ions. We will return to this shortly.

We can derive a rate coefficient for dielectronic capture by resorting to detailed balance arguments. The process is resonant, so the cross-section is actually infinite at the velocity which satisfies energy conservation:

$$\frac{1}{2}mv_c^2 = E_i^{**} - E_{i+1} \quad (210)$$

where E_i^{**} is the energy of the doubly excited recombined ion, and E_{i+1} is the energy of the ground-state of the initial ion. That is:

$$\sigma_{dc}(v) = \alpha_{dc}\delta(v - v_c) \quad (211)$$

where α_{dc} has units of cm^3s^{-1} . If n_{i+1} is the density of $i + 1$ ions in the ground state, then the rate of dielectronic captures per unit volume per unit time is given by:

$$R_{dc} = \int d^3\mathbf{v} n_e n_{i+1} v \sigma_{dc}(v) f(v) = 4\pi n_e n_{i+1} \alpha_{dc} v_c^3 e^{-mv_c^2/kT} \left(\frac{m}{2\pi kT}\right)^{3/2} \quad (212)$$

where $f(v)$ is the Maxwellian distribution given in (183). If n_i^{**} is the density of i ions in the doubly excited state, then the autoionization rate per unit volume is:

$$R_{auto} = n_i^{**} A_a \quad (213)$$

These rates must be equal in thermodynamic equilibrium. But, in thermodynamic equilibrium, the level populations are given by:

$$\frac{n_i^{**}}{n_i} = \frac{g_i^{**}}{g_i} e^{-(E_i^{**} - E_i)/kT} \quad (214)$$

where n_i , g_i and E_i are the density, degeneracy and energy of the i th ion in the ground state (see Sect. 5), and the ionization structure $n_e n_{i+1}/n_i$ is given by the Saha equation:

$$\frac{n_e n_{i+1}}{n_i} = \frac{2g_{i+1}}{g_i} \left(\frac{mkT}{2\pi\hbar^2} \right)^{3/2} e^{-\chi/kT} \quad (215)$$

where $\chi = E_{i+1} - E_i$ is the ionization potential for the i th ion. Collecting terms gives:

$$\alpha_{dc} = \frac{g_i^{**}}{2g_{i+1}} 2\pi^2 \left(\frac{\hbar}{mv_c} \right)^3 A_a . \quad (216)$$

Not surprisingly, the temperature drops out since dielectronic capture and autoionization must be related by fundamental constants.

The dielectronic capture rate is obtained by plugging (216) back into (212):

$$R_{dc} = n_e n_{i+1} \frac{g_i^{**}}{2g_{i+1}} A_a \left(\frac{h^2}{2\pi mkT} \right)^{3/2} e^{-mv_c^2/2kT} . \quad (217)$$

To get the *dielectronic recombination rate*, as opposed to dielectronic capture rate, we must multiply the expression in (217) by the probability that the doubly excited atom stabilizes radiatively. Quite generally, this probability is given by the ratio of the sum of all radiative decay rates from the excited state to the sum of all radiative plus autoionizing decay rates:

$$\text{Probability of stabilization} = \frac{\sum A_r}{\sum (A_r + A_a)} . \quad (218)$$

Usually, however, there is only one dominant decay channel in each case, which involves the decay of the core excitation. Thus, the dielectronic rate coefficient becomes:

$$R_{dr} \approx n_e n_{i+1} \frac{g_i^{**}}{2g_{i+1}} \left(\frac{h^2}{2\pi mkT} \right)^{3/2} e^{-mv_c^2/2kT} \left(\frac{A_a A_r}{A_a + A_r} \right) . \quad (219)$$

The factor in parenthesis has a maximum when $A_a = A_r$. Hence, dielectronic recombination is efficient when the rates for autoionization decay and radiative decay of the core excitation are approximately equal. Since $A_a \sim Z^0$ and $A_r \sim Z^4$, this is primarily the case for high- Z ions.

We can get a further quantitative feel for how these rates compare by again using a semi-classical treatment. Note that the dielectronic capture process is very similar to collisional excitation, except that the final state of the colliding electron is now a bound state rather than a continuum state. We should therefore be able to get a rough idea of the rate coefficient for this process by extending our earlier classical treatment of collisional excitation to energies below threshold. Recall that our earlier expression for the excitation cross-section was given by (180):

$$\sigma_{mn}(E) \equiv \frac{\pi a_0^2}{g_m E_c} \Omega_{mn}. \quad (220)$$

For capture into principal quantum number n , we can integrate this expression over the velocity range between neighboring Rydberg levels to yield an estimate for α_{dc} associated with this core excitation:

$$\alpha_{ij,n}^{dc} \approx \sigma_{ij}(\delta v) \approx \sigma_{ij} \frac{2Z^2 Ryd}{n^3 m v} = \frac{\pi e^4}{g_i} \Omega_{ij} \frac{Z^2 Ryd}{n^3 m^2 v_c^3}. \quad (221)$$

But $\Omega_{ij}/g_i = 2\pi/\sqrt{3} f_{ij} \bar{g}/E_{ij}$ (181) and

$$f_{ij} = \frac{3}{2} \frac{m c^3}{e^2} \frac{\hbar^2}{E_{ij}^2} A_{ij}^r \quad (222)$$

(Equation 113). Plugging these expressions in and equating $\alpha_{ij,n}^{dc}$ from (221) to α^{dc} from (216) we obtain:

$$\frac{A_{ij}^a}{A_{ij}^r} = \frac{12}{\sqrt{3}} \frac{g_{i+1}}{g_i^{**}} \bar{g} \frac{Z^2}{n^3} \left(\frac{Ryd}{E_{ij}} \right)^3 \frac{1}{\alpha^3}. \quad (223)$$

Note that since $E_{ij} \sim Z^2$, this ratio scales like Z^{-4} , as expected from our earlier discussion. Taking all other features to be of order unity, with $E_{ij} \sim Z^2 Ryd$, this ratio is found to be $\sim Z^{-4} \alpha^{-3}$. Setting it equal to unity (for maximum dielectronic recombination efficiency) then implies $Z \approx 40$. So we see that dielectronic recombination becomes important only for the higher- Z elements, most notably iron.

5 Types of Equilibria

In most astrophysical settings, some form of equilibrium applies, in which there is a balance between competing processes, e.g. heating and cooling, ionization and recombination, excitation and deexcitation, etc. The nature of the equilibrium has a very important effect on the emergent spectrum.

There are three “systems” which may or may not equilibrate with one another:

- the kinetic distributions of the electrons and ions;
- the atomic level populations;
- the radiation field.

We say that we have strict thermodynamic equilibrium when all three systems are characterized by statistical distributions at the same temperature T . In particular, for this case, the radiation field is characterized by the blackbody distribution, so the spectrum is especially simple. For absolute equilibrium, the temperature T , must also be independent of spatial position within the

gas. However, as long as the scale length for temperature variations: $T/|\nabla T|$ is long compared to all relevant mean free paths for particle and photon interactions, it is appropriate to talk about strict local thermodynamic equilibrium, where $T = T(\mathbf{r})$.

The more common term, *local thermodynamic equilibrium* (LTE) usually applies to the situation where the particle distributions and level populations are in equilibrium, but the radiation field is not, i.e. the scale lengths of the system are not sufficient to trap emitted photons and enforce thermalization.

5.1 Properties of LTE

In LTE, the population of a given energy level is proportional to the degeneracy in that level and a Maxwell-Boltzmann factor $e^{-E/kT}$. This gives rise to:

The Maxwellian velocity distribution for free particles

$$\frac{n(v)dv}{n} = 4\pi v^2 \left(\frac{m}{2\pi kT} \right)^{3/2} e^{-\frac{mv^2}{2kT}} dv, \quad (224)$$

The Maxwell-Boltzmann distribution for level populations

$$\frac{n_j^z}{n^z} = \frac{g_j^z}{U^z(T)} e^{-\frac{E_j^z - E_0^z}{kT}}, \quad (225)$$

where $U^z(T)$ is the partition function:

$$U^z(T) = \sum_j g_j^z e^{-\frac{E_j^z - E_0^z}{kT}} \quad (226)$$

and *The Saha equation for the ionization balance*

$$\frac{n_e n^{z+1}}{n^z} = \frac{2U^{z+1}(T)}{U^z(T)} \frac{(2\pi m kT)^{3/2}}{h^3} e^{-\frac{\chi^z}{kT}}. \quad (227)$$

The definition of $U^z(T)$ can be problematic. For example, for H-like atoms

$$g_n = 2n^2 \quad (228)$$

$$e^{-\frac{E_n - E_0}{kT}} = e^{-\frac{z^2 R y}{kT} (1 - \frac{1}{n^2})} \quad (229)$$

$$\Rightarrow U^z(T) \rightarrow \infty; \quad (230)$$

we must truncate the expansion at some high Rydberg level. This is usually a function of the particle density, due to the effects of neighboring charges.

In LTE, the prediction of the emergent spectrum requires the solution of the radiative transfer equations

$$\frac{dI_\nu}{d\tau_\nu} = -I_\nu + S_\nu \quad (231)$$

$$S_\nu = \frac{j_\nu}{k_\nu} \quad (232)$$

$$d\tau_\nu = k_\nu ds \quad (233)$$

Here, I_ν is the specific intensity of the radiation field, j_ν is the emissivity of the gas, and k_ν is the opacity, all of which are functions of the position along the path of propagation s . S_ν is called the source function.

For discrete lines:

$$j_{nm} = \frac{h\nu_{nm}}{4\pi} g_m n_n A^{nm} \varphi(\nu) \quad (234)$$

$$k_{nm} = g_m n_m \sigma_{mn}(\nu) - g_n n_n \sigma_{mn}(\nu) \quad (235)$$

But from radiation theory, we found:

$$A_{nm} = \frac{8\pi^2}{3} \frac{e^2}{mc^3} f_{nm} \nu^2 \quad (236)$$

$$\sigma_{mn}(\nu) = \sigma_{nm}(\nu) = \frac{1}{3} \frac{\pi e^2}{mc} f_{nm} \quad (237)$$

and, relating the level populations using the Maxwell-Boltzmann distribution (225), we get:

$$S_{nm} = \frac{j_{nm}}{k_{mn}} = \frac{2h\nu_{nm}^3}{c^2} \frac{1}{(e^{h\nu_{nm}/kT} - 1)} = B_{\nu_{nm}}(T) \quad (238)$$

which is the blackbody function evaluated at the frequency of the transition ν_{nm} !

Looking inward to an optically thick medium at constant temperature, (231) implies:

$$I_\nu(\tau_\nu) = B_\nu(T)(1 - e^{-\tau_\nu}) \quad (239)$$

The line intensities are “limited” to the blackbody intensity evaluated at the local temperature.

For the approximation of LTE to hold, we need the rates for collisional deexcitation of discrete levels to be comparable to the rates for spontaneous radiative decay:

$$n_e C_{nm}(T) \sim A_{nm} \quad (240)$$

$$\Rightarrow n_e \sim 9 \cdot 10^{19} T_K^{1/2} (\delta E)_{keV}^3 cm^{-3} \quad (241)$$

In astrophysical settings, such high densities are only reached in the atmospheres of compact objects like white dwarfs and neutron stars.

When the assumption of LTE is invalid, the calculation of the emergent spectrum can be much more complicated. In general, we have to explicitly

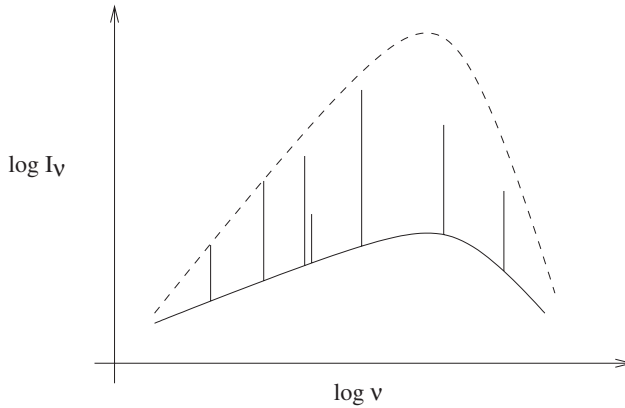


Fig. 5. An illustration of the limitation of line intensities to the blackbody intensity for cases where LTE holds

account for all microphysical processes that feed and deplete the individual quantum levels. The most general, time-dependent equations are of the form:

$$\frac{dn_i^z}{dt} = -n_i^z \sum_j R_{ij} + \sum_{z',k} n_k^{z'} R_{ki} \quad (242)$$

where the R 's represent the rates for collisional and photon interactions coupling levels within the same charge state and in neighboring charge states.

5.2 Coronal Equilibrium

Equation (242) is difficult to solve because of the requirement for inclusion of such a large array of diverse processes. Therefore, it is useful to adopt some approximations, applicable to particular cases. One of the most important sets of approximations applies to the case of *coronal equilibrium*, sometimes also referred to as *collisional ionization equilibrium*.

There are three basic assumptions underlying this limit:

- Excitation and ionization are dominated by electron-ion collisions. Deexcitation is dominated by spontaneous radiative decay.
- Densities are low enough so that atoms are always in their ground states.
- The radiation field has a negligible effect on the atomic populations, and the plasma is optically thin, so photoabsorption and scattering can be ignored.

Sources of applicability for these assumptions include: stellar coronae, the shocked gas of older supernova remnants, and the intracluster media of galaxy clusters.

The charge state distribution in coronal equilibrium is determined by a balance of collisional ionization and radiative and dielectronic recombination:

$$\frac{dn_z}{dt} = -n_e n_z (C_z + \alpha_z) + n_e n_{z+1} \alpha_{z+1} + n_e n_{z-1} C_{z-1} \quad (243)$$

Here C_z represents the rate coefficient for collisional ionization (see Sect. 5.4), and α_z represents the combined RR + DR rate coefficient for recombination (Sects. 4.5 and 4.6, respectively). Note that the characteristic timescales for equilibrium to be established are $\sim(n_e C)^{-1}$ or $\sim(n_e \alpha)^{-1}$. These can be larger than 10^3 yr for $n_e \leq 1 \text{ cm}^{-3}$, as found in young supernova remnants. Since this age exceeds the age of the remnant (for the most recent supernovae), the shocked gas that we observe for these cases may still be ionizing, and the charge balance may be far from equilibrium. A similar situation can be found during weak flares in stellar coronae. Here the electron density is closer to $n_e \sim 10^{10} \text{ cm}^{-3}$, so the equilibration time is of order a few seconds, comparable in some cases to the duration of the flare.

However, if equilibrium is established, so that the left-hand side of (243) vanishes, the electron density n_e , drops out of the equation, and the resulting steady-state ionization structure becomes a function only of temperature. This turns out to be also true of the discrete spectrum. Specifically, since we are assuming that the atoms are “always” in the ground state, the populations of upper levels are given by the ratio of collisional excitation rates from the ground level, to the spontaneous radiative decay rates back down:

$$n_2 = \frac{n_e n_1 \gamma_{12}(T)}{A_{21}}, \quad (244)$$

and the line emissivities become:

$$\epsilon_{21} = n_e n_1 \gamma_{21}(T) E_{12}, \quad (245)$$

where $\gamma_{12}(T)$ is the collisional excitation coefficient (Sect. 5.3), and E_{12} is the energy of the transition. The density of the ion in the ground state is given by $n_1 = A_{elem} f_Z(T) n_H$, where A_{elem} is the abundance of the element relative to hydrogen, and $f_Z(T)$ is the steady-state ion fraction, as discussed above. It is useful to define a *line power* for the transition: $P_{21} = \epsilon_{21}/n_e^2$. We thus get:

$$P_{21}(T) = \left(\frac{n_H}{n_e} \right) A_{elem} f_Z(T) \gamma_{12}(T) E_{12} \quad (246)$$

which is typically expressed in units of $\text{erg cm}^3 \text{s}^{-1}$.

Actually, the “two-state” model discussed above is too simple, since important contributions to upper level populations can also come from ground-state excitations to higher levels, which then radiatively decay to intermediate states. However, even these more complicated “channels” can still be incorporated via the definition of more general, effective excitation rate coefficients that include these terms. A number of coronal equilibrium “spectral synthesis” codes have been developed over the years to provide these line power calculations, and some are in widespread use in the community. The largest

residual uncertainties in these codes generally involve the treatment of the DR rates, and the completeness of the line lists.

For an intermediate charge state, the ion fraction, f_Z , peaks in temperature at some particular value. The excitation rate coefficient, γ , generally increases across the range of temperatures where the ion exists in appreciable abundance. Therefore, the line power, P , exhibits a peak at a temperature often called the *temperature of formation*, T_f . The presence of a particular line in the spectrum implies the existence of plasma at or near the temperature of formation for that line. The modulation of line powers by the temperature dependence of the ion fraction thus gives us a crude temperature diagnostic.

The measured line flux for a collisional plasma is given by:

$$F_{21} = \frac{e^{-N_H \sigma(E_{21})}}{4\pi d^2} \int dV dT n_e^2(T, V) P_{21}(T) \quad (247)$$

$$\sim \frac{e^{-N_H \sigma(E_{21})}}{4\pi d^2} P_{21}(T_f) \int dV n_e^2(T_f) \quad (248)$$

where $e^{-N_H \sigma E_{21}}$ is the attenuation factor through the interstellar and circumsource media, and d is the distance to the source. The integral that remains in (247) is called the *volume emission measure*, $VEM(T_f)$. As indicated, it is a function of temperature. For an assumed set of abundances, and a given column density, N_H , the shape of the emergent spectrum for a coronal plasma is given completely by the shape of the volume emission measure distribution.

5.3 X-Ray Photoionization Equilibrium

A quite different set of approximations applies to the case of *photoionization equilibrium*, where the presence of an intense continuum radiation field has a significant effect on the ionization and thermal structure of the surrounding gas. The electrons are generally too cool to excite prominent X-ray lines in this case, and excited levels are instead populated by direct recombination, by radiative cascades following recombination onto higher levels, and by direct photoexcitation from the continuum.

These conditions are typically found in the circumsource media of accretion-powered sources, such as X-ray binaries and active galactic nuclei. For example, in the accreting gas surrounding an X-ray binary, the energy density in the continuum radiation field is given by:

$$U_\gamma \sim \frac{L}{4\pi R^2 c} \sim 3.7 \cdot 10^4 \text{ erg cm}^{-3} \quad (249)$$

where we have taken $L \sim 10^{38} \text{ erg s}^{-1}$, and $R \sim 10^{11} \text{ cm}$. In contrast, the thermal energy density in the electron distribution is given by:

$$U_e \sim \frac{3}{2} n_e kT \sim 2.4 \text{ erg cm}^{-3} \quad (250)$$

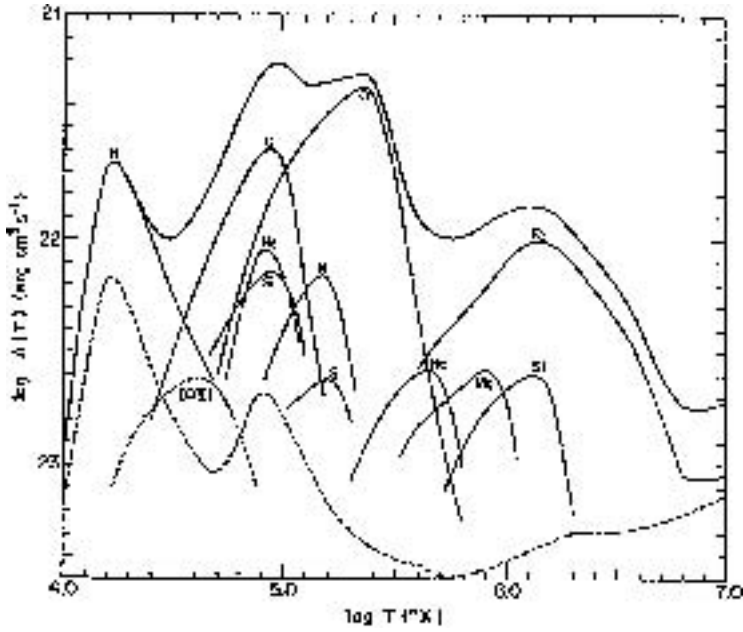


Fig. 6. The power radiated (ϵ/n_e^2) of a cosmic abundance plasma as a function of temperature in coronal equilibrium. The contributions of the individual elements are indicated. Line radiation dominates at temperatures below $10^7 K$

for typical values of the electron density and temperature, $n_e \sim 10^{12} \text{ cm}^{-3}$, $kT \sim 10 \text{ eV}$.

In photoionization equilibrium, the ionization structure is determined by the balance between photoionization and recombination.

$$n_z \int_0^\infty dE \frac{F_E}{E} \sigma_z(E) = n_e n_{z+1} \alpha_{z+1}(T) \quad (251)$$

where F_E is the differential continuum flux, in units of $\text{erg cm}^{-2} \text{ s}^{-1} \text{ keV}^{-1}$, $\sigma_z(E)$ is the photoelectric cross-section as a function of energy (Sect. 3.8), and $\alpha_{z+1}(T)$ is the recombination coefficient, again including both RR and DR contributions. The equilibrium temperature is determined by the solution of the equation of energy balance, where the rate of energy injection is due to photoelectric heating, and the rate of energy loss is due to radiation:

$$\begin{aligned} \sum_{elem,z} n_{z,elem} \int_0^\infty dE \frac{F_E}{E} \sigma_{z,elem}(E) (E - E_{thresh}^{z,elem}) \\ = \sum_{elem,z} n_e n_{z,elem} \Lambda_{z,elem}(T) \end{aligned} \quad (252)$$

In the optically thin limit: $F_E = \frac{L}{4\pi R^2} f(E)$, where $f(E)$ is a normalized function containing the details of the spectral shape of the irradiating continuum. In addition, we can write $n_{z,elem} = A_{elem} f_z n_H$, and $n_e = \mu_e n_H$, where μ_e , the mean number of electrons per hydrogen atom, is only a weak function of gas parameters. Therefore “environment specific” factors are all embodied in a single quantity

$$\xi = \frac{L}{nR^2} \quad (253)$$

which is usually referred to as the *ionization parameter*. Given the specification of this ionization parameter, the self-consistent solution of the ionization and energy balance equations yield the $f_z(\xi)$ values for all the elements, and $T(\xi)$. A variety of codes are in widespread use to calculate these quantities.

Plots of the ionization structure of iron as a function of temperature for conditions of coronal equilibrium and photoionization equilibrium are shown in Fig. 7. Two important features are immediately apparent from this figure:

- First, the “dominance of closed shells” is much less obvious in the case of photoionization equilibrium. Given the big jump in ionization potential following the removal of all the electrons in a closed shell, the closed shell charge states (e.g. Ne-like and He-like) dominate over a wide range of temperature for a plasma in coronal equilibrium. However, for a photoionized plasma, photoionization out of inner shells (L-shell and K-shell) plays a significant role for the hard irradiating spectra characteristic of accretion-powered sources. This process is essentially unaffected by the removal of outer valence electrons, eliminating any important distinction between open shell and closed shell charge states.
- Second, the gas is significantly “overionized” relative to the electron temperature in a photoionized plasmas. For example, Ne-like iron (FeXVII) peaks at $kT_e = 10$ eV in the photoionized case, while for the coronal plasma Ne-like iron peaks at $kT_e = 400$ eV.

The significantly different temperatures appropriate to a given charge state for coronal and photoionized plasmas lead to several important characteristic differences in the emergent X-ray spectra. For a coronal plasma, $kT \sim \chi$, the ionization potential of the ion, and δE , the characteristic energies of the line excitations. The lines are formed primarily via collisional excitation from the ground state. The brightest lines are E1 transitions, or those “fed” by E1 transitions. In a photoionized plasma, $kT \ll \chi$ and δE , so the electrons have insufficient energy to collisionally excite X-ray lines. Instead, lines are formed mostly by radiative cascades following recombination. Recombination flux tends to distribute evenly among all the available levels. Hence, the brightest lines tend to come from ions with the fewest states in the upper level configuration (e.g. K-shell ions). In addition, the cascades “rain” into the lowest lying excited levels. Therefore, lines from these levels are usually quite bright. Often, these are higher order multipole transitions, with low collisional coupling strengths to the ground.

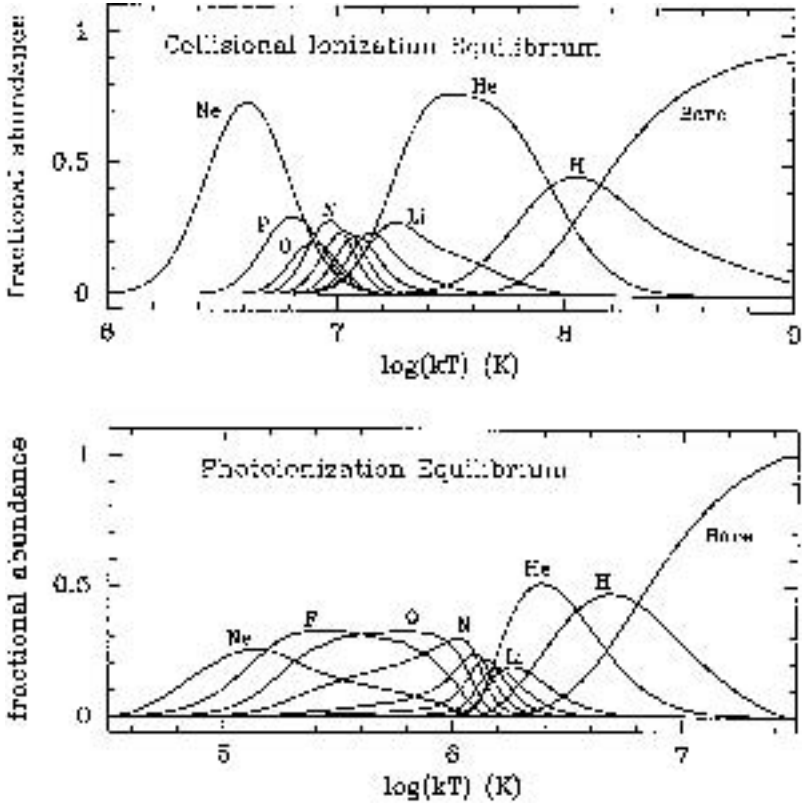


Fig. 7. Plots of the ionization structure of iron as a function of temperature for coronal equilibrium (*top*), and photoionization equilibrium (*bottom*). The element symbols refer to the isoelectronic charge state of iron, e.g. the curve labeled O refers to oxygen-like Fe (figure courtesy of Masao Sako)

However, the most useful spectroscopic diagnostics for distinguishing coronal equilibrium from photoionization equilibrium are the narrow radiative recombination continua (RRC's) expected for the latter case. In Sect. 4.5, we found that RRC's are described by

$$\frac{dW}{dt d\omega dV} \sim \left(\frac{\hbar\omega}{\chi}\right)^3 \sigma_{PI}(\omega) \left(\frac{\chi^2}{mc^2 kT}\right)^{3/2} e^{\chi/kT} e^{-\hbar\omega/kT} \quad (254)$$

For a coronal plasma, $kT \sim \chi \sim \hbar\omega$. The RRC's are broad and do not have high contrast relative to the accompanying bremsstrahlung continuum. On the other hand, in a photoionized plasma, $kT \ll \chi$ and $\hbar\omega$. For this case, the RRCs are strong and fall off steeply with increasing energy. They resemble "lines" at moderate resolution. The relative width of this feature is a good

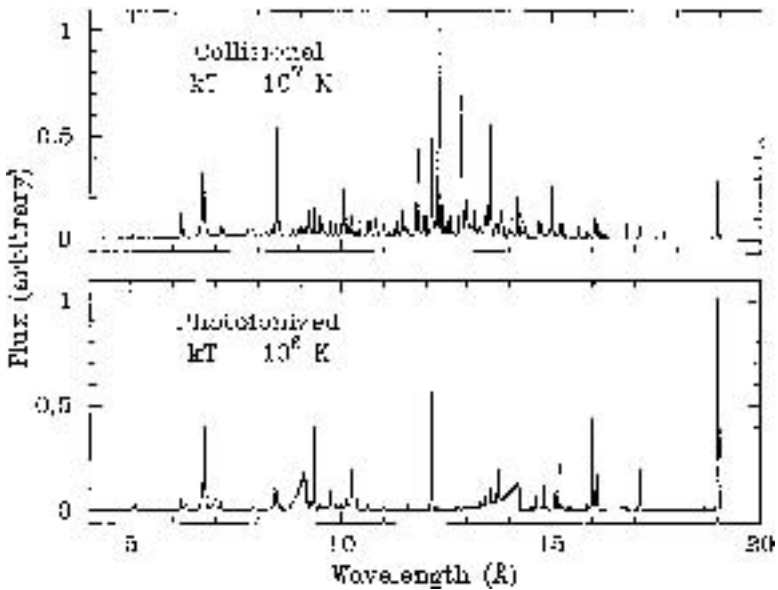


Fig. 8. Plots of characteristic emergent soft X-ray spectra for conditions appropriate to a coronal plasma *top* and an X-ray photoionized plasma *bottom*. Note that the coronal spectrum is more “rich”, due to the greater prominence of the Fe L complex in that case. The photoionized spectrum is dominated by lines from lower-Z K-shell elements, and by low temperature radiative recombination continua (figure courtesy of Masao Sako)

temperature diagnostic, and, if the width is larger than predicted, can signal the presence of extra sources of heating in the gas.

This is illustrated in Fig. 9, which shows the predicted spectrum of neon in a photoionized plasma for electron temperatures of both 10 eV and 50 eV. The former is the expected temperature for these charge states, if photoelectric heating provides the only form of energy injection in the gas. The latter might apply if there are other sources of heating which contribute. As can be seen, the discrete line spectra look very similar for the two cases. However, the RRC (near 9 Å) is much broader and less pronounced at the higher temperature.

With the launches of the grating spectrometers on the *Chandra* and *XMM-Newton* observatories, we now have clear detections of these features in many sources. A particular dramatic case is illustrated in Fig. 10, which shows the spectrum of the bright Seyfert 2 galaxy NGC 1068, as obtained with the reflection grating spectrometer on *XMM-Newton* [10] As can be seen, the spectrum is rich in emission lines, especially H-like and He-like lines of carbon, nitrogen, oxygen, and neon. The RRC’s from most of these species are labeled in the figure. They are narrow, indicating a low electron temperature of a few eV, characteristic of a photoionized plasma. In NGC 1068, the soft

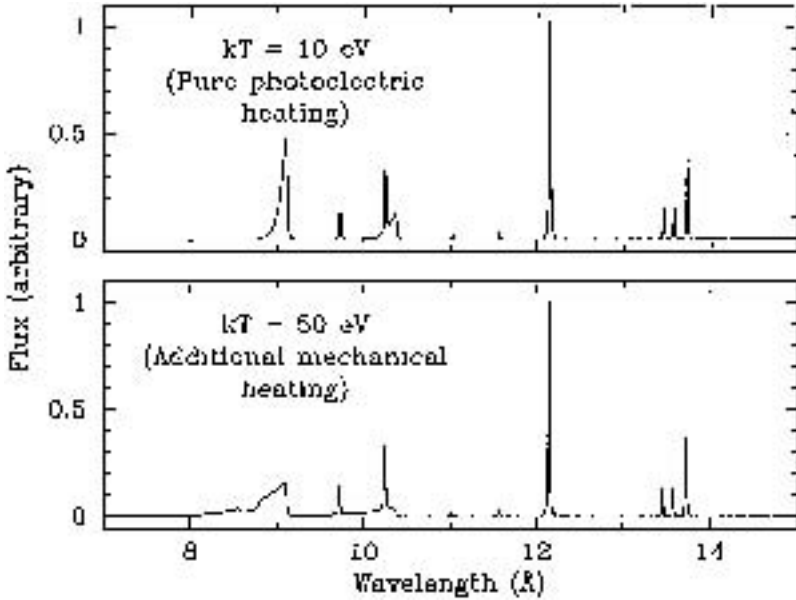


Fig. 9. Plots of the expected spectra of H-like and He-like neon in photoionized plasmas with electron temperatures of 10 eV *top*, and 50 eV *bottom*, but with similar ion fractions. Note the differences in the RRC's for the two cases (figure courtesy of Masao Sako)

X-ray spectrum is produced in an ionization cone, which is irradiated by an intense X-ray continuum emanating from a central obscured nucleus.

5.4 Thermal Instability in Photoionized Plasmas

It has been known for many years that X-ray photoionized plasmas can be thermally unstable in certain regions of ionization parameter space. Typically, this is represented by means of an “S-curve”, a plot of the temperature, derived by solving the equation of energy balance (252), versus an ionization parameter $\Xi = F/n_e T \sim \xi/T$. An example is shown in Fig. 11. On the curve itself, the heating rate is equal to the cooling rate, so the gas is in thermal balance. To the right, heating dominates over cooling, as indicated, while to the left, cooling dominates over heating. On branches of the curve which have positive slope in this figure, the gas is thermally stable. Small perturbations upward in temperature increase the cooling, while small perturbations downward in temperature increase the heating. However, on the branches which have negative slope, the gas is thermally unstable. A small perturbation upward in temperature increases the heating, causing further temperature rise, while a small perturbation downward increases the cooling. Many different calculations of these effects exist in the literature, and

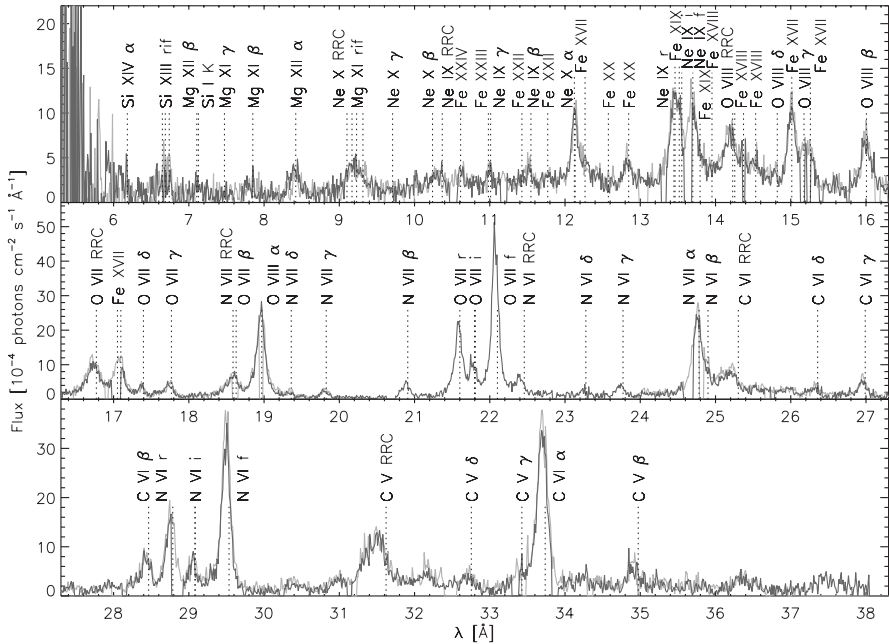


Fig. 10. *XMM-Newton* reflection grating spectrum of the prototypical Seyfert 2 galaxy NGC 1068 [10]. Features of H-like and He-like ions from carbon to silicon, as well as significant emission due to Fe L-shell transitions, dominate the spectrum of its active nucleus. Bright, narrow RRC’s point unambiguously to the predominance of recombination in a photoionized plasma. Strong higher order Rydberg transitions ($np \rightarrow 1s$) are also present, implying the presence of photoexcitation as well

the resulting S-curves show a lot of variations, even for similar assumptions. However, most show some degree of thermal instability in similar regions of (Ξ, T) -space.

The thermal instability has important spectroscopic implications. Growth rates are $\sim kc_s$ where k is the wave number, and c_s is the sound speed, up until a maximum value of k , the inverse of the so-called “Field length”, where they saturate due to the increasing importance of thermal conduction. The medium is expected to “break” into multiple stable phases, which can coexist in pressure and ionization equilibrium. Gas in an unstable phase should quickly disappear, unless it is replenished on a timescale comparable to the inverse of the growth rate. We do not expect to see emission lines characteristic of ionization parameters in the unstable regimes.

The instability arises because of ionization through various atomic shells, which acts as a type of phase transition. The criterion for instability is:

$$\left(\frac{\partial(C - H)}{\partial T} \right)_{\Xi} < 0 \quad (255)$$

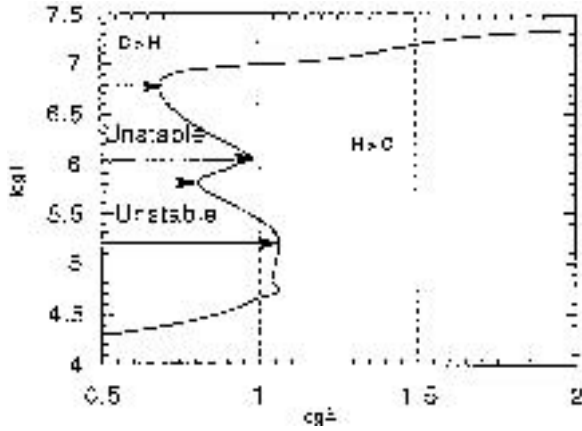


Fig. 11. The phase diagram for a photoionized gas with cosmic abundances irradiated by a 10 keV bremsstrahlung spectrum (figure from [11])

where C represents the complete set of cooling processes, and H represents the complete set of heating processes. Continuum and bound-state processes contribute to both C and H , but the latter dominate in the region of instability. To see the effect of ionization, it is useful to group charge-states for a given atomic shell, e.g. Fe L, Si K etc., but to also distinguish between two types: “X-ray ions”, such as Fe L, O K, Si K, Fe K, in which $\chi \sim \text{keV} \gg kT_e$, and “EUV ions”, such as Fe M, O L, He K, in which $\chi \leq 100 \text{ eV} \leq kT_e$.

For the X-ray ions, the primary heating contribution is due to the photoelectric effect:

$$H = n_i \zeta_{PE} \langle \varepsilon \rangle \quad (256)$$

where ζ_{PE} is the photoionization rate per ion, and $\langle \varepsilon \rangle$ is the mean energy released in the photoelectron. The primary cooling contribution is due to radiative recombination:

$$C = n_e n_{i+1} \alpha_R(T_e) kT_e . \quad (257)$$

Because the gas is in ionization balance, the photoionization rate must be equal to the recombination rate:

$$n_i \zeta_{PE} = n_e n_{i+1} \alpha_R \quad (258)$$

In addition, $\langle \varepsilon \rangle \sim \chi \gg (kT_e)$, so $H \gg C$. As the ionization parameter is increased, so that we ionize through an atomic shell, both H and C initially rise and then fall. One finds that this shell contributes a negative term to the partial derivative in (256), during the rise and a positive term during the fall. Thus, each atomic shell contributes both an unstable and a stable lobe.

For the EUV ions, the same analysis holds, but in this case: $kT_e \gg \langle \varepsilon \rangle$, so that $C \gg H$, and the contribution is positive during the rise and

negative during the fall. The net thermal stability is determined by the sum of the contributions from all of these atomic shells. The situation can be quite complex, because the stable and unstable lobes contributed by the different elements occur at different temperatures. One finds that there are “near cancellations”, which makes the total stability quite sensitive to details related to the elemental abundances and the shape of the ionizing spectrum. This can be beneficial, because we can exploit this sensitivity to derive strong constraints on physical conditions in the gas, if the signatures of thermal instability are visible in the spectra.

6 Discrete Line Diagnostics

The relative prominence of various emission line features in cosmic X-ray spectra is determined principally by the abundances of the different elements, and the locations of the K- and L-shell complexes associated with these elements within the X-ray band. Scaling from the H-like isoelectronic sequence, the energies of the K-shell features are given roughly by:

$$E_K \sim (10 \text{ eV})Z^2, \quad (259)$$

while the energies of the L-shell features are approximately:

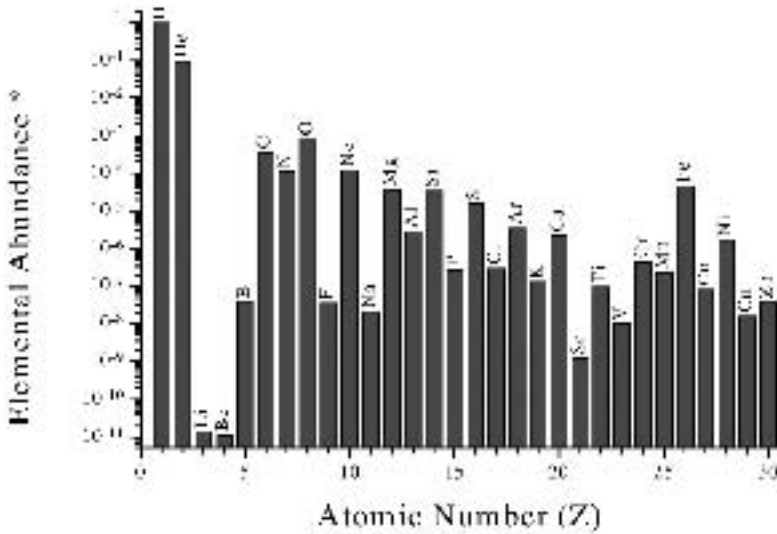
$$E_L \sim (1.5 \text{ eV})Z^2. \quad (260)$$

If we define the conventional soft X-ray band to cover the range $100 \text{ eV} \leq E \leq 10 \text{ keV}$, we see that it includes the K-shell features of beryllium ($Z = 4$) through gallium ($Z = 31$), and the L-shell features of oxygen ($Z = 8$) through thallium ($Z = 81$).

A plot of standard cosmic abundances as a function of atomic number appears in Fig. 12. Several features should be noted:

- The abundances drop precipitously with increasing Z above carbon ($Z = 6$). The abundances of lithium, beryllium, and boron ($Z = 3, 4,$ and 5 , respectively) are especially low.
- In general, elements with even values of Z have considerably higher abundances than elements with odd values of Z . This is a consequence of the importance of α -chain reactions, in the production of the heavier elements during the late stages of stellar evolution.
- There is a very prominent abundance peak at iron ($Z = 26$) in the higher Z -range. This is a consequence of nuclear stability. ^{56}Fe has the highest binding energy per nucleon of any nucleus. Fusion reactions that produce lower Z elements are exothermic, while above iron, fusion reactions become endothermic.

Given these considerations, the most significant K-shell complexes in cosmic X-ray spectra are due to C, N, O, Ne, Mg, Si, S, Ar, Ca, Fe, and Ni, while the



* Taken from Anders & Greife, *Gaschemistry of Cosmochemicals* *ApJ* **53**, 197 (1989).

Fig. 12. A plot of the standard cosmic abundance of the elements as a function of atomic number Z (figure courtesy of Masao Sako)

most significant L-shell complexes are associated with Si, S, Ar, Ca, Fe, and Ni. It is one of the major strengths of cosmic X-ray spectroscopy that such a wide range of elements and charge states is measured in a single wavelength band.

6.1 Lyman Series Transitions in H-like Ions

At the characteristic temperatures of X-ray emitting plasmas, the low-Z abundant elements are often found in their H-like charge states. The most prominent emission lines are the Lyman series transitions:

$$\begin{aligned}
 \text{Ly } \alpha_1: & 1s-2p \ ^2P_{3/2}; & \text{Ly } \alpha_2: & 1s-2p \ ^2P_{1/2}; \\
 \text{Ly } \beta_1: & 1s-3p \ ^2P_{3/2}; & \text{Ly } \beta_2: & 1s-3p \ ^2P_{1/2}; \\
 \text{Ly } \gamma_1: & 1s-4p \ ^2P_{3/2}; & \text{Ly } \gamma_2: & 1s-4p \ ^2P_{1/2} \\
 & \dots & &
 \end{aligned}$$

The ratio of the line intensities for the two transitions in each case is given roughly by the degeneracy factors, e.g.:

$$\text{Ly } \alpha_1 / \text{Ly } \alpha_2 \sim \frac{2(3/2 + 1)}{2(1/2) + 1} = 2 .$$

Recall that the splitting is:

$$\Delta E_{n,j} = E_n \frac{(Z\alpha)^2}{n^2} \left[\frac{n}{j+1/2} - 3/4 \right] \quad (261)$$

$$\frac{\Delta E_{1,2}}{E} \sim \frac{(Z\alpha)^2}{2n} \quad (262)$$

so these are barely resolvable, especially at low Z .

These lines are usually quite bright, and are therefore good for abundance and velocity determinations. Examples are shown in Fig. 13, which displays the *XMM-Newton* reflection grating spectrum of the supernova remnant SNR 1E0102-72.3 in the Small Magellanic Cloud [12]. This young core collapse remnant is an oxygen-rich Type 1b SNR akin to Cas A [13], so the spectrum is dominated by lines of elements produced by α -burning reactions. The Lyman series lines (α through γ) of H-like C, N, Ne, and Mg are clearly visible in the spectrum, as marked in the figure.

Despite their prominence in astrophysical X-ray spectra, Lyman series transitions have rather limited utility as density and temperature diagnostics. Lines in this series are all produced through electric dipole transitions, so the radiative decay rates are high, and the collisional couplings are negligible. In addition, because of the n^{-2} dependence of the H-like energy levels

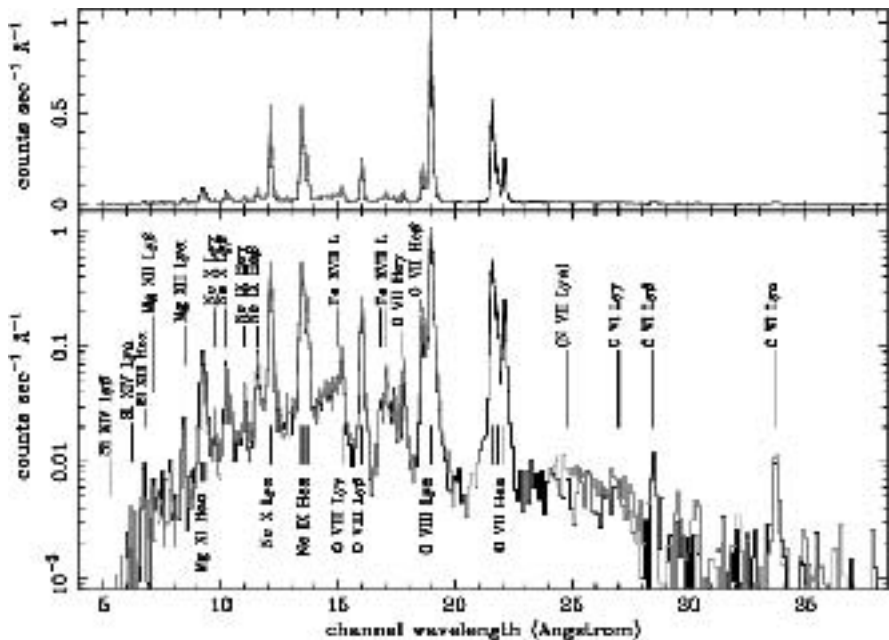


Fig. 13. The *XMM-Newton* reflection grating spectrum of SNR 1E0102-72.3 from [12]. For clarity, the spectrum is shown in both linear (*top*) and logarithmic (*bottom*) units. H-like and He-like emission lines from carbon to silicon are present with some significant emission from Fe L transitions as well

(261), the upper levels for the different transitions in the series are close in energy, so the Boltzmann factor in the excitation rates varies only slightly from transition to transition in the temperature range where the H-like ion is the dominant species (see Fig. 14). At the very low temperatures characteristic

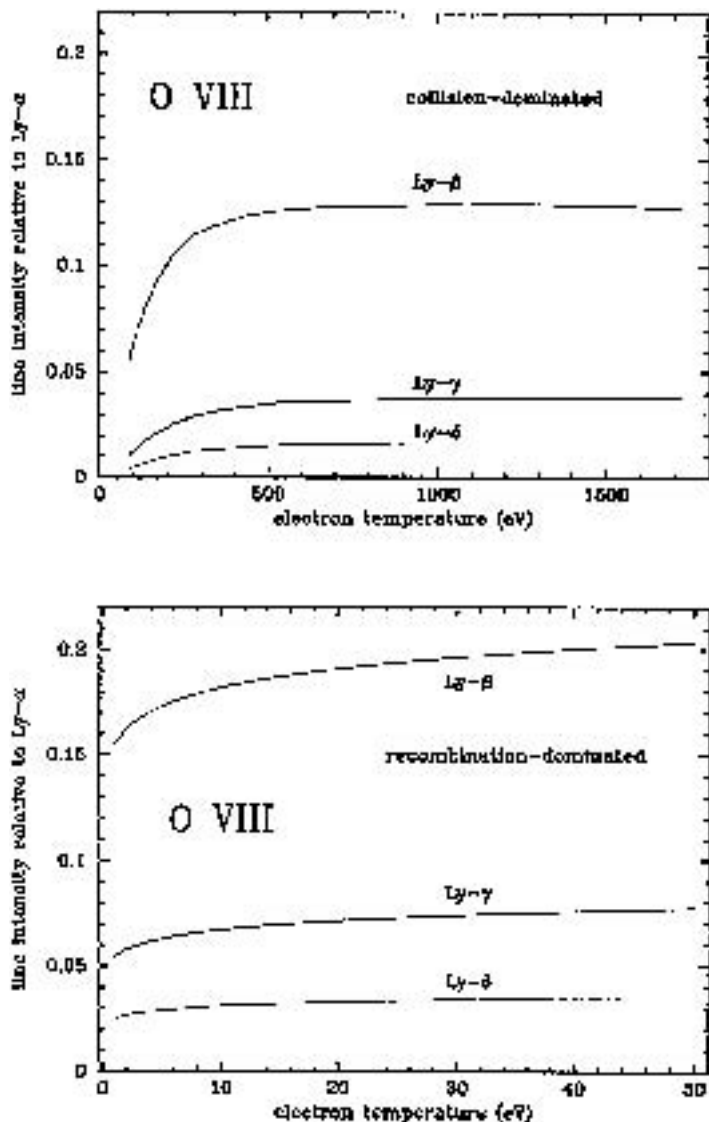


Fig. 14. Plots of the ratio of higher series Lyman line intensities to the Lyman α line intensity as a function of temperature in O VIII, for both coronal plasmas (*top*), and photoionized plasmas (*bottom*)

of photoionized plasmas, Lyman series lines are formed by radiative cascades associated with radiative recombination. The line ratios produced by these processes are somewhat different than those associated with collisional excitation in collisional plasmas. This is apparent from Fig. 14, where it can be seen that the Ly β to Ly α ratio for O VIII is ~ 0.11 for a coronal plasma, and ~ 0.14 for a photoionized plasma. Similar enhancements are found for the higher series line ratios as well.

6.2 He-like Transitions

He-like K-shell lines are among the most important of all in the soft X-ray band. Since the He-like charge state is a tight “closed shell”, this is the dominant ion species over a wide range in temperature, particularly in coronal plasmas. In addition, as explained below, these lines exhibit strong sensitivity to electron density, temperature, and ionization conditions in the emitting plasma.

The most important K-shell He-like transitions are as follows:

$$\begin{aligned} W: & 1s^2 \ ^1S_0 - 1s2p \ ^1P_1 \\ X: & 1s^2 \ ^1S_0 - 1s2p \ ^3P_2 \\ Y: & 1s^2 \ ^1S_0 - 1s2p \ ^3P_1 \\ Z: & 1s^2 \ ^1S_0 - 1s2p \ ^3S_1 \end{aligned}$$

W is an electric dipole transition, also called the *resonance* transition, and is sometimes designated with the symbol r . X and Y are the so-called *intercombination* lines. These are usually blended (especially for the lower- Z elements), and are collectively designated with the symbol i . Z is the *forbidden* line, often designated by the symbol f . It is a relativistic magnetic dipole transition, with a very low radiative decay rate.

The temperature sensitivity of these lines arises as follows [14–16]: Since W is an electric dipole transition, the collision strength for collisional excitation of this line includes important contributions from higher order terms in the partial wave expansion, and thus continues to increase with energy above threshold. By contrast, X and Z are electric dipole forbidden. The dominant term in the excitation collision strength for these transitions involves electron exchange. Therefore, their excitation collision strengths drop off strongly with energy above threshold, whereas Y remains relatively constant. As a result, the line ratio: $G = (X + Y + Z)/W$ is a decreasing function of electron temperature.

The density sensitivity comes from the fact that the 3S_1 level can be collisionally excited to the 3P levels. At high electron density, that process successfully competes with radiative decay of the forbidden line. Therefore, the ratio $R = Z/(X + Y)$ drops off above a critical density, n_c . The critical density depends strongly on Z . For C V, $n_c \sim 10^9 \text{ cm}^{-3}$, while for Si XIII, $n_c \sim 10^{13} \text{ cm}^{-3}$.

However, the R -ratio can also be affected by the presence of a significant ultraviolet radiation field [14]. In particular, the 3S_1 level can be photoexcited to the 3P levels, prior to radiative decay, if there is sufficient ultraviolet intensity at the energy of the relevant transitions. That leads to suppression of the forbidden line and enhancement of the intercombination lines, mimicking the effects of high electron density.

These dependences are illustrated in Figs. 16 and 15, which shows the He-like spectra of oxygen, nitrogen, and carbon for two stellar coronal sources, Procyon and Capella, as measured with the *Chandra* low energy transmission grating spectrometer [17]. The corona of Procyon is cooler than that of Capella. As can be seen, the resonance lines are consequently less intense for Procyon, in comparison to both the intercombination and forbidden lines. Note that the forbidden line of carbon is also comparatively suppressed for Procyon in relation to the intercombination line. While this looks like a density effect, it is actually due to the ultraviolet radiation field from this star. Procyon is an F star, with a relatively high UV flux.

In photoionized plasmas, the excited levels for He-like ions are fed directly by recombination and also by radiative cascades following recombination onto higher levels. The forbidden line is most intense, since most of the cascades from high- n , high- l (high- J) levels land on the lowest lying $1s2s(J=1)$ level, which produces the forbidden line. This is illustrated in Fig. 17, and can also be seen in the spectrum of NGC 1068 shown in Fig. 10 for both the He-like oxygen lines near 22 Å, and the He-like nitrogen lines near 29 Å.

6.3 Iron L-Shell Transitions

Since iron is the most abundant high- Z element, its L-shell spectrum plays a crucial role in astrophysical X-ray spectroscopy. As a result of their higher ionization potentials, the iron L-shell ions contribute significant line emission even when the lower- Z elements are full stripped. For collisionally ionized plasmas, this complex samples a wide range in temperature (0.2–2 keV). In addition, the L-shell spectrum is very “rich”, and there is significant diagnostic sensitivity.

The brightest iron L-shell lines are of the form:

$$\begin{aligned} 2s^22p^k - 2s^22p^{k-1}3d \\ 2s^22p^k - 2s^22p^{k-1}3s \\ 2s^22p^k - 2s2p^k3p \end{aligned}$$

The $2p - 3d$ lines generally have the highest oscillator strength. The line positions are a strong function of charge state. Thus, the ionization structure is easily discernible, which provides a simple, abundance-independent constraint on the temperature distribution.

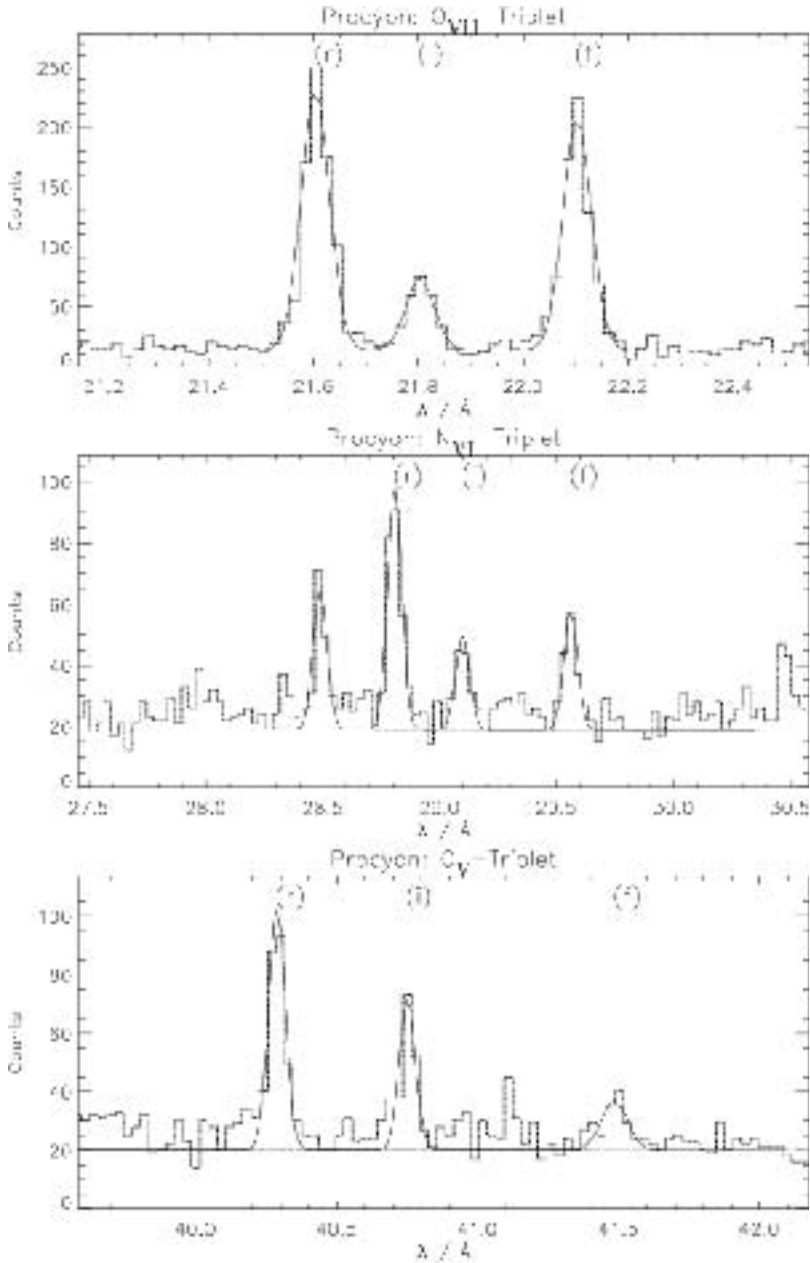


Fig. 15. He-like complexes for O, N, and C from the coronal star Procyon, as measured with the *Chandra* low energy transmission grating spectrometer (From [17])

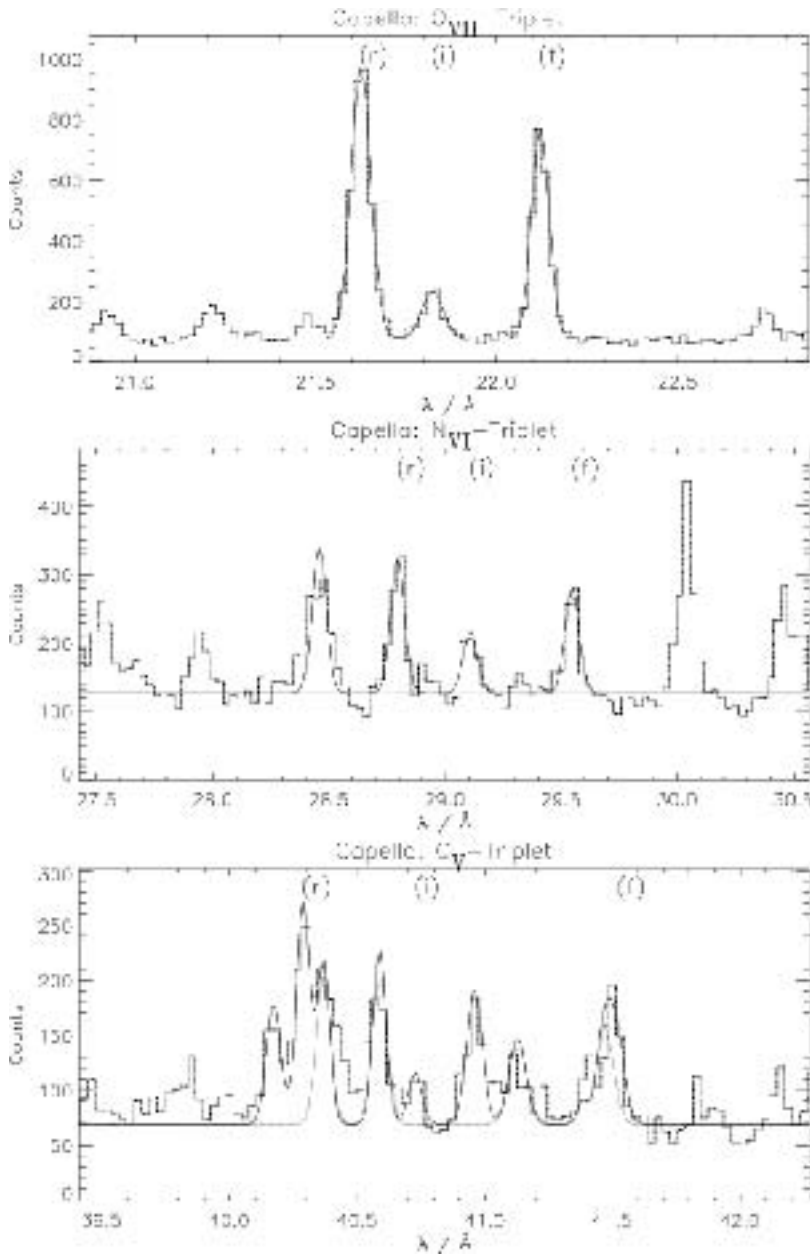


Fig. 16. He-like complexes for O, N, and C from the coronal star Capella, as measured with the *Chandra* low energy transmission grating spectrometer (From [17])

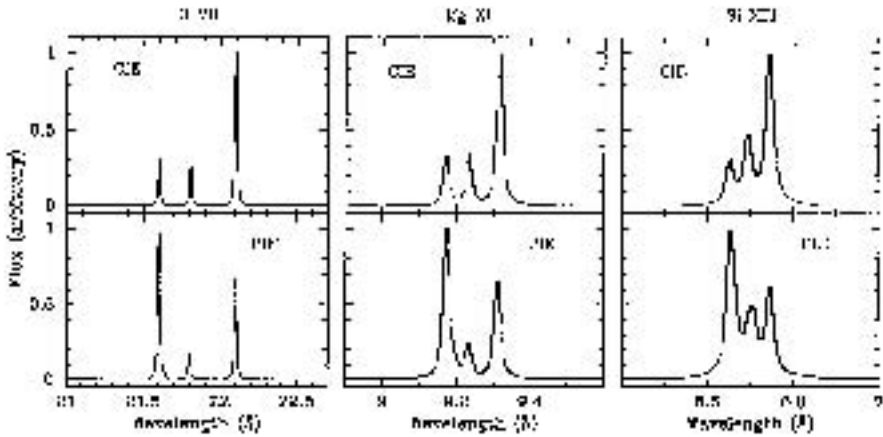


Fig. 17. Calculated He-like emission line spectra of oxygen, magnesium, and silicon for photoionization equilibrium *top* and coronal equilibrium *bottom* plasmas. Note the prominence of the forbidden lines in the case of the photoionized plasmas (figure courtesy of Masao Sako)

This is illustrated in Fig. 18, which shows the iron L spectrum of Capella, as observed with the *Chandra* high energy transmission grating spectrometer. Plotted below the measured data are the calculated contributions from each of the individual charge states, ranging from Na-like iron (Fe XVI) to Be-like iron (Fe XXII). Note the relatively clean separation between the L-shell complexes from each of these ions, allowing for relatively easy decomposition of the spectrum, even with only moderate resolution. The density sensitivity of the iron L complex arises from the fact that the intermediate iron L charge states (e.g. N-like and C-like) possess a number of low lying metastable levels associated with $n = 2 \rightarrow n' = 2$ excitations. These can be populated collisionally, leading to new “seed” states for $2 \rightarrow 3$ excitations, followed by $3 \rightarrow 2$ radiative decays. Such density diagnostics turn on at electron densities $\sim 10^{13} \text{ cm}^{-3}$.

6.4 The Iron K-Shell Complex

The iron K complex is relatively isolated in the spectrum at energies $\sim 6 - 7 \text{ keV}$, where even non-dispersive detectors have moderate spectral resolution. Thus, iron K lines were the first discrete atomic features unambiguously detected for cosmic X-ray sources.

An important contributor to iron K emission, especially for accretion-powered sources, is due to fluorescence from cold material in the vicinity of a bright X-ray continuum. Fluorescence involves a radiative decay following inner shell photoionization, i.e. a transition of the form $1s^2 2s^2 2p^{k-1} nl - 1s 2s^2 2p^k nl$. The excited level, in this case, can also decay via autoionization

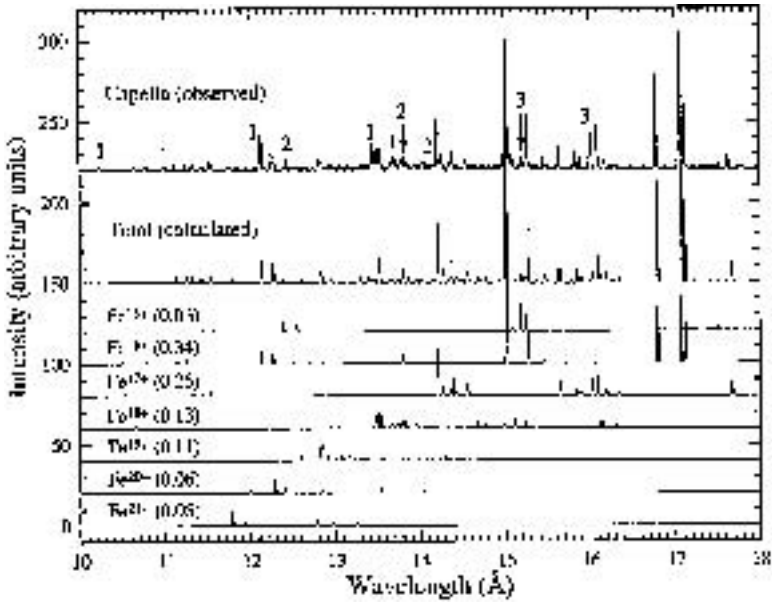


Fig. 18. The spectrum of Capella obtained with *Chandra* high energy transmission grating spectrum, compared with a calculated spectrum showing the separate contributions of each of the iron L charge states (From [19])

by ejecting one of the outer electrons in the valence shell. This latter process dominates for low- Z elements. However, since radiative decay rates scale like Z^4 , and autoionization decay rates scale like Z^0 , the fluorescence yield becomes appreciable for a high- Z element like iron. The near-neutral iron K fluorescence line falls at 6.4 keV, easily distinguishable from the He-like lines near 6.7 keV, and the Lyman α line at 7.1 keV.

The iron K complex also exhibits new features due to the relative importance of dielectronic recombination. DR leads to Li-like “satellites” to He-like K-lines: $1s2pnl - 1s^2nl$. These satellites are shifted down in energy. Higher n implies a smaller shift, and is associated with a higher energy of the recombining electron. Therefore, the satellite spectrum is temperature sensitive (cf. [20]).

At astrophysical densities, all atoms are in the ground state. Most of the satellite lines cannot be produced by collisional excitation of Li-like iron (e.g. $1s2p^2 - 1s^22p$). They come purely from DR on He-like atoms. However, other lines terminate in the ground configuration of the Li-like ion (e.g. $1s2s2p - 1s^22s$). These can be produced by both collisional excitation of Li-like atoms, and DR on He-like atoms. Hence, the line ratios for these various transitions provide an independent measure of the charge balance. Analysis of the Fe K He-like spectrum thus provides independent constraints on the

electron temperature and the level of ionization, and is ideal for investigating departures from ionization equilibrium.

7 Concluding Remarks

As a field, astrophysical X-ray spectroscopy is still in its infancy. While the grating spectrometers on *Chandra* and *XMM-Newton* have already showered us with fascinating results on a wide variety of diverse sources, most of the data have not been completely reduced, and many sources bright enough to provide reasonable spectra have still not yet been observed. A much larger population of interesting sources are too faint for these instruments, but should be amenable for study with the more sensitive experiments planned for future missions such as *Constellation-X* and *XEUS*.

The complete analysis of all of these observations will require a greater level of spectroscopic sophistication than most X-ray astronomers are accustomed to. In the past, we have had the luxury of fitting relatively simple “canned” spectral models to low resolution, low statistics data. As the quality of our spectra improves, these more familiar techniques no longer suffice. Some would prefer to ignore the complications, and continue to work only on the faintest sources where the paucity of photons precludes worrying about spectral details. I have even heard some argue that we should not attempt to build higher resolution spectroscopic instruments, because the data they will acquire will be too difficult to interpret. I find this view to be very unscientific. We will always benefit by better instruments and better data.

In these lectures, I have tried to provide a synopsis of the kinds of issues X-ray astronomers must consider in analyzing their spectroscopic data. But this is by no means a “user manual”. There are no simple codes that will take proper account of all relevant processes, and provide a neat set of “results” at the push of a button. We will all have to continue to learn as we go along. The first data sets we have obtained have already pointed to holes in our existing atomic databases, and in our understanding of particular excitation processes. To make progress, we must complement our data analysis activities with direct involvement in laboratory astrophysics experimentation, and atomic calculation. Astronomers must become spectroscopists, and spectroscopists must become astronomers. This is how real progress will emerge.

Acknowledgments

I am indebted to a number of key individuals for helping me to finally make these lecture notes available for publication. First, I would like to thank Pascal Favre of the Integral Science Data Centre, for his tremendous assistance with the preparation of the manuscript. Second, I would like to thank my students and colleagues at Columbia: Ehud Behar, Jean Cottam, Mingfeng Gu, Ali Kinkhabwala, Maurice Leutenegger, Frits Paerels, John Peterson, Masao

Sako, and Daniel Savin for help with the figures, editing the text, and for contributing many of the ideas that are contained within. I have also benefited from numerous conversations with current and previous collaborators, most notably Peter Beiersdorfer and Duane Liedahl at the Lawrence Livermore National Laboratory, and Bert Brinkman, Jelle Kaastra, and Rolf Mewe of SRON, Utrecht. Finally, I would like to thank my hosts for the Saas Fee program: Manuel Güdel and Roland Walter, for inviting me to Les Diablerets and allowing me to participate in this distinguished lecture series.

References

1. Cowan, R., 1981, *The Theory of Atomic Structure and Spectra*, Los Alamos series in Basic and Applied Science, University of California Press, Berkeley, CA
2. Rybicki, G. B., and Lightman, A. P., 1979, *Radiative Processes in Astrophysics*, Wiley, New York, 1979
3. Giacconi, R., Gursky, H., Paolini, F., et al., 1962, *Phys. Rev. Lett.*, **9**, 439
4. Blandford, R., Fabian, A., Pounds, K., 2003, *X-Ray Astronomy in the New Millennium*, Cambridge University Press
5. Schlegel, E. M., 2002, *The Restless Universe: Understanding X-Ray Astronomy in the Age of Chandra and Newton*. Oxford University Press
6. Tucker, W., Tucker, K., 2001, *Revealing the Universe: the Making of the Chandra X-ray Observatory*, Harvard University Press, Cambridge, MA
7. Hutchinson, I. H. 1987, *Principles of plasma diagnostics*, Cambridge University Press
8. Lotz, W. 1967, *ApJS*, **14**, 207
9. Rumph, T., Bowyer, S., and Vennes, S., 1994, *AJ*, **107**, 2108
10. Kinkhabwala, A., Sako, M., Behar, E., et al., 2002, *ApJ*, **575**, 732
11. Hess, C. J., Kahn, S. M., & Paerels, F. B. S., 1997, *ApJ*, **478**, 94
12. Rasmussen, A. P., Behar, E., Kahn, S. M., et al., 2001, *A&A*, **365**, 231
13. Blair, W.P., Morse, J. A., Raymond, J. C., et al., 2000, *ApJ*, **537**, 667
14. Gabriel, A. H., and Jordan, C., 1969, *MNRAS*, **145**, 241
15. Pradhan, A. K., 1982, *ApJ*, **263**, 477
16. Porquet, D., Mewe, R., Dubau, J., et al., 2001, *A&A*, **376**, 1113
17. Ness, J.-U., Mewe, R., Schmitt, J. H. M. M., et al., 2001, *A&A*, **367**, 282
18. Kahn, S. M., Leutenegger, M. A., Cottam, J., et al., 2001, *A&A*, **365**, 312
19. Behar, E., Cottam, J., and Kahn, S., 2001, *ApJ*, **548**, 966
20. Dubau, J., Volonte, S., 1980, *Reports on Progress in Physics*, vol. 43, 199



Peter von Ballmoos